The Pennsylvania State University

The Graduate School

The Eberly College of Science

LIGAND-CONTROLLED ELECTRONIC PROPERTIES IN INORGANIC MATERIALS

A Dissertation in

Chemistry

by

Juyeong Kim

Submitted in Partial Fulfillment
of the Requirements
for the Degree of

Doctor of Philosophy

August 2015

The dissertation of Juyeong Kim was reviewed and approved* by the following:

Benjamin J. Lear
Assistant Professor of Chemistry
Dissertation Advisor
Chair of Committee

Alexander Radosevich
Assistant Professor of Chemistry

Thomas E. Mallouk
Evan Pugh Professor of Chemistry, Physics, Biochemistry and Molecular Biology
Associate Head of the Chemistry Department

Thomas N. Jackson
Robert E. Kirby Chair Professor of Electrical Engineering

Barbara J. Garrison
Shapiro Professor of Chemistry
Head of the Chemistry Department

*Signatures are on file in the Graduate School

ABSTRACT

Electron transfer is a widespread and important phenomenon studied across multiple fields of science and engineering such as biology, chemistry, and physiology. Specifically, understanding electron transfer in inorganic systems has become of significant interest since energy and health emerged as the most important focus to humankind in the 21st century. Inorganic materials and complexes function as an essential part in alternative energy conversion systems, molecular electronics, cell bodies, and medicinal treatments, and in many cases they are used as redox centers — places where electron potential energy can be stored and then extracted. In order to best-control their performance for specific applications, it is crucial to know fundamentals of how to modulate the electronic properties of inorganic materials and further have control over the electron transfer in different conditions. In this dissertation, a ligand-assisted approach is introduced to tune the electronic properties of different inorganic materials, and various types of electron transfer are investigated in such materials spectroscopically and electrochemically.

I begin by demonstrating that the electronic properties of a series of ruthenium polypyridyl complexes with a hydroxypyridine ligand can be modulated by change in the electron density of the hydroxypyridine ligand. Protonation/deprotonation and ethylation of this ligand were implemented, and I found that electronic perturbation of the ligand influenced the electronic structure of the metal center as well as the bipyridine ligands via UV-visible spectroscopy, nuclear magnetic resonance spectroscopy and electrochemical measurements. The deprotonation enriched the electron density of the metal center and induced de-shielding of the protons in the bipyridine ligands, and the ethylation only increased the reduction potential for the hydroxypyridine ligand. Furthermore, the intramolecular electron transfer between the bipyridine ligands could be studied with the ethylated complex. There was no absorption band detected for

the intramolecular electron transfer, indicating that the complex possesses poor electronic coupling between the ligands through the metal center. This study provided an easy strategy for controlling the electronic properties of a transition metal complex by coordinating a hydroxypyridine ligand and applying a different substituent to the ligand.

Following this, I studied examining systems with redox active ligands. Coordination of organic radicals to metal centers and study of a related intermolecular electron transfer were performed by synthesizing a dinuclear zinc complex with tetracyanoquinodimethane (TCNQ) radicals, bridged with a TCNQ σ-dimer. The individual molecules were easily stacked in crystals, forming π-stacking of the TCNQ ligands. Unlike existing research, incorporation of the TCNQ σ-dimer introduced a novel stacking pattern with different spacing between the TCNQ ligands. The intermolecular electron transfer was measured via diffuse reflectance spectroscopy, and the magnetic coupling between the adjacent TCNQ ligands was studied by electron paramagnetic resonance spectroscopy. The crystals showed a high-energy intermolecular charge transfer band, resulting in poor electronic conductivity. Also, I found antiferromagnetic coupling through the π-stacks. Use of the TCNQ σ-dimer demonstrated an example of how one could differentiate the stacking pattern in such π-stacked systems and modify a degree of the intermolecular interaction electronically and magnetically.

The ligand-assisted approach for modification of the electronic structure could be expanded from the molecular systems to nano-sized inorganic materials. I studied the effect of ligands on the surface electronic structure of semiconductor nanocrystals by using colloidal zinc oxide nanocrystals. In this case, the electronically excited species was the zinc oxide nanocrystal, and two different types of carboxylic acid ligands (aliphatic and aromatic) were adsorbed on the surface of the nanocrystals. Changes to the electronic properties were probed by examining change to the bandgap energy using UV-visible spectroscopy. The absorption spectra showed that

the bandgap energy of the nanocrystal with the aromatic ligand became lower than that with the aliphatic ligand. It appears that π orbitals of the aromatic ligand could have better coupling with the valence band of the nanocrystals, leading to decrease in the bandgap. Further studies such as precise size measurements will follow to confirm this tentative conclusion.

Continuing the theme of using the effect of ligands to control electrons, ligand effect to the electronic properties of a solvatochromic molecule was demonstrated by investigating confined environment in which coumarin 153 was encapsulated in a metal-organic framework. Different solvent molecules were intercalated into the pore with coumarin 153, and the absorption and fluorescence emission spectra were acquired. After confined in the pore, coumarin 153 lost the original solvent-dependent photophysical properties in the absorption and emission process. However, the Stokes shift of coumarin 153 was observed to be solvent-dependent and increased in energy upon confinement in the pore. Based on these divergent results, I hypothesize that the framework dominantly affected the energetics of coumarin 153. Specifically, lattice flexibility of the framework, mainly from ligand rotation, might dissipate the excited state energy of the molecule. This confined system with a solvatochromic molecule can be a good platform to understand complex molecular interactions in restricted space and how to perturb the electronic properties of confined molecules through indirect contact.

These studies suggest that the electronic properties of inorganic materials can be controlled by modifying the electronic structure of coordinated ligands and inducing electronic interactions between the inorganic substrate and the ligand. I believe that the ligand-assisted approach is useful for tuning the electronic properties of inorganic materials in that ligands can be easily combined with inorganic materials in the solution phase and simultaneously influence the energetics to a large degree. In addition, the fact that there are a large number of ligands to be explored provides a potential toolbox for adjusting the properties of inorganic materials.

TABLE OF CONTENTS

LIST OF FIGURES

LIST OF TABLES

ACKNOWLEDGEMENTS

I would like to thank my family, specially my parents. All your support helped me fulfill my PhD study. Also, I would like to thank my fiancé, Christine, and her family. Your prayers have been great encouragement to me whenever I had hard time. To Christine, I appreciate your patience for five years.

The only best thing that makes me think studying abroad in USA was a good decision is that I met Ben and my labmates (Please forgive me for not writing your individual name). I cannot thank them enough for everything that I was given from them. I was lucky to know Ben and become his student. I can say that he is one of few advisors who are academically learned as well as personally good-natured. In addition, I feel that my labmates are another family in USA. Now, I regret that I did not spend much time with them.

I would like to thank all my committee members. Specially, to Prof. Alexander Radosevich and Prof. Thomas E. Mallouk, I learned not only science from your class but also qualities as a scholar.

I would like to thank my collaborators for data acquirement and analysis: Dr. Hemant P. Yennawar for solving crystal structures, Dr. Alexey Silakov for EPR measurements, Prof. Nitin Samarth and Robbie Fraleigh for SQUID measurements, and Prof. Michelle Dolgos at Oregon State for solving the intermediate MOF structure.

I would like to thank faculty members and their students at Penn State Chemistry for generosity in their instruments: Prof. Raymond E. Schaak and his students for use of a powder X-ray diffractometer, Prof. Mark Maroncelli, Dr. Jens Breffke, and Chris Rumble for use of a fluorometer, Prof. Mary Beth Williams and Sun Sha for use of a fluorometer, and Prof. Christine Dolan Keating and Dr. Dan Dewey for use of a confocal microscope.

Lastly, to the only one in heaven, I did not know why you brought me to Penn State, but I know why now. Again, I do not know why you bring me and Christine to Illinois, but I will believe in your providence to my life. I will not stop praying, and hope to honor you by my life. Please help me.

Chapter 1

Electron transfer in inorganic materials

Introduction

Electron transfer is a fundamental process that occurs in a wide range of chemical and biological systems. There have been longstanding efforts to elucidate mechanisms of electron transfer in such systems. Beyond examining naturally occurring phenomena themselves, one can also turn to develop an artificial system in order to find specific factors that affect electron transfer. One of the most-studied systems is Cruetz-Taube ion and its derivatives.[1] This dinuclear ruthenium complex is composed of amine ligands, a pyrazine bridging ligand, and two ruthenium metal centers in different oxidation states (Figure 1-4b). It first allowed direct measurement of the Frank-Condon barrier to electron transfer from Ru^{II} to Ru^{III}. Since then, various derivatives of the complex have been developed and provided fundamental information for the rate of electron transfer and charge localization between the redox metal centers in terms of types of ancillary ligands, bridging ligands, and metals.[2,3]

Based on the fundamental understanding of electron transfer, there are growing needs to develop a new material that can be best-suited for practical applications such as developing water oxidation catalysts,[4,5] molecular electronics,[6,7] and dye-sensitized solar cells.[8] In these systems, it is important to control behavior of electrons to improve their performance. For instance, there has been effort to apply findings of electron transfer in natural photosynthesis to develop artificial photosynthetic systems.[9-12] The sophisticated structure of the photosynthetic system has been emulated by synthesizing transition metal complexes, and their photophysical properties can be modified by coordinating different organic ligands and also having multi-nuclear metal centers.

However, the development of the efficient system has been much slower than expected.[13] Likewise, other systems such as molecular electronics have not shown any good progress despite of much effort performed so far.[14] Thus, one will still need not only to understand the phenomena themselves exhaustively, but also build a fundamental understanding on how to control physicochemical parameters for electron transfer that can be useful for practical applications.

Below, I will introduce a brief description of electron transfer theory and show different types of electron transfer that occur in inorganic materials.

Electron transfer theory

Marcus theory for outer sphere electron transfer

Electron transfer between two redox sites can be described by Marcus theory.[15-17] Figure 1-1 shows two potential energy curves of reactants and products as a function of nuclear reaction coordinate when electron transfer between two molecules occurs (outer sphere electron transfer), $A^- + B \rightarrow A + B^-$. There are two pathways for electron transfer in the given system: thermal and optical. To thermally induce the electron transfer, an input of energy of ΔG^* is required to overcome the energy barrier, which is the energy difference between the minimum energy of the reactants and the energy at which the two potential energy surfaces of the reactants and products cross.

On the other hand, the electron transfer can be induced by light irradiation in the range from UV to NIR. If the irradiation energy is equal to the reorganization energy (λ), it can allow electrons in the ground state to move into the excited state where the wavefunctions between the two potential energy surfaces have in-phase vibrational overlap. Note that the electron transfer process will occur at $X = 0$ as there is no change in the reaction coordinate because the rate of

light absorption occurs within femtoseconds (10^{-16}-10^{-14} s), but nuclear motions are comparatively sluggish (10^{-13}-10^{-12} s). Based on the principle in this potential energy surface diagram, one can interpret the electron transfer process between two or more species and correlate the electron transfer event with its observed spectrum.

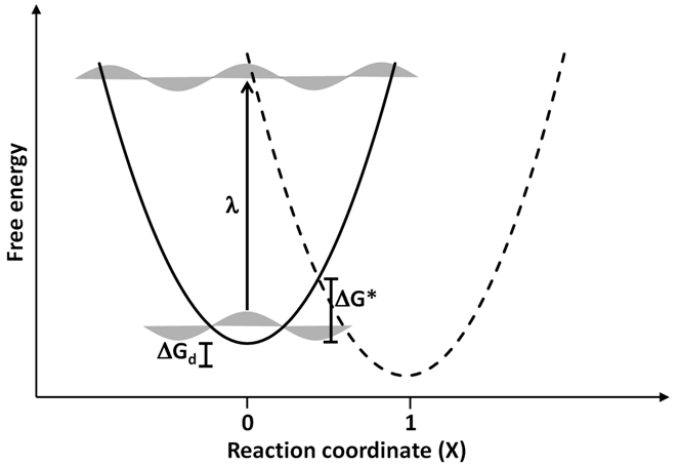

Figure 1-1: Potential energy surfaces of reactants (solid) and products (dotted) with respect to reaction coordinate.

Marcus-Hush theory for inner sphere electron transfer

Furthermore, a modified potential energy diagram (Figure 1-2) can be utilized to understand the electron transfer that occurs within a single molecule (inner sphere electron transfer), for instance, a dinuclear metal complex, M^{+}-L-M → M-L-M^{+} (M = metal and L = ligand).[15-17] When considering this intramolecular electron transfer, it is assumed that there is some degree of electronic coupling between two redox sites in the molecule, which can be typically dependent on their energy levels, orbital overlap, and distance between two redox sites. Thus, the potential energy curves of reactants and products are expressed as two merged curves. As the magnitude of electronic coupling (H_{AB}) increases, the potential energy minima of reactants

and products approach each other. Then, one can extract the degree of electron delocalization between the redox centers throughout the molecule.

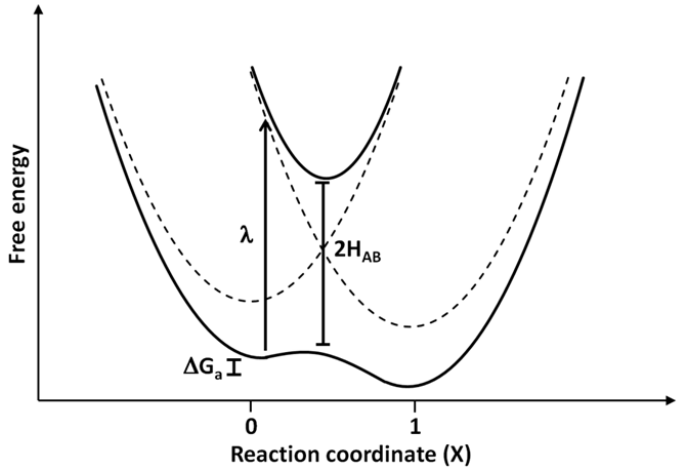

Figure 1-2: Potential energy surfaces of a molecule with electronically-coupled redox centers (solid) and those without any electronic coupling (dotted).

Applications of the theory

Intramolecular electron transfer

In this section, I will discuss electron transfer that occurs within a molecule. Due to the variety of transition metal complexes reported in this field, I will limit the topic to mono- and di-nuclear ruthenium complexes.

The intramolecular electron transfer has been studied by using transition metal complexes. Compared to organic molecules, transition metal complexes can absorb wider wavelengths of light and have better stable redox properties. The electron transfer occurs largely between a metal and a ligand under light irradiation (Figure 1-3): metal to ligand charge transfer (MLCT) and ligand to metal charge transfer (LMCT) in which the energy levels of the metal and the ligand are responsible for the direction of the electron transfer. Furthermore, between metals or ligands in

different oxidation states one might expect to observe metal to metal charge transfer (MMCT) or ligand to ligand charge transfer (LLCT).

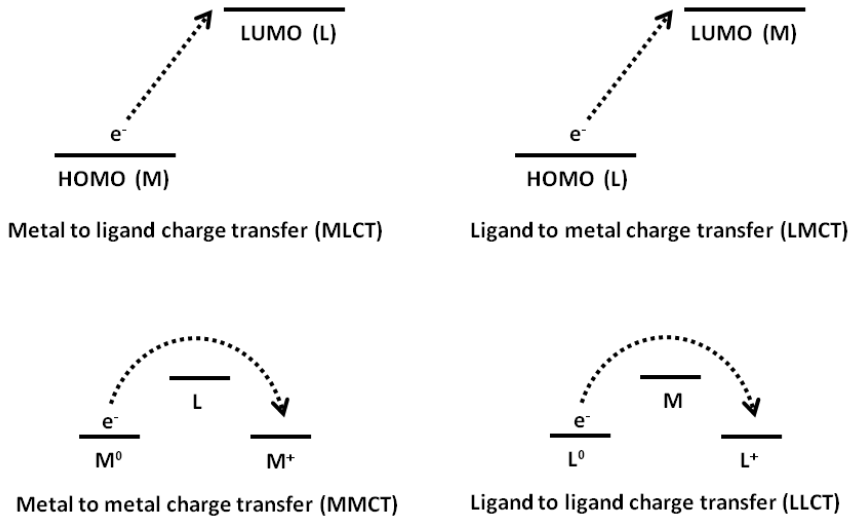

Figure 1-3: Intramolecular electron transfer in transition metal complexes (M = metal and L = ligand).

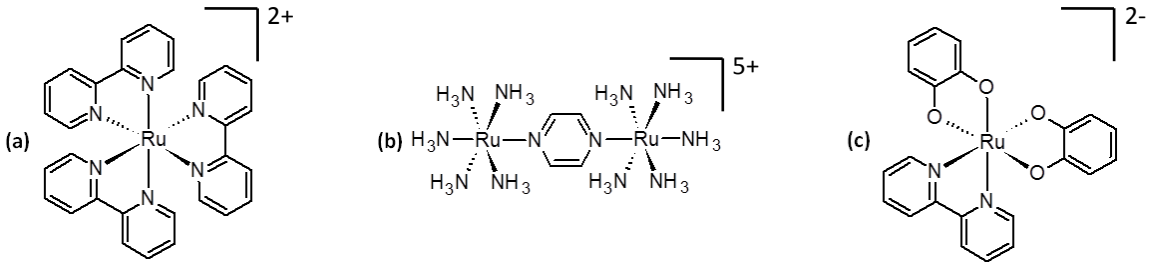

Figure 1-4: Ruthenium complexes that contain a characteristic absorption band for (a) MLCT, (b) MMCT, and (c) LLCT.

The study of MLCT in a series of ruthenium polypyridyl complexes has been a popular topic because they showed high extinction coefficient for visible light and a relatively long lifetime for the excited state (890 ns in acetonitrile) (Figure 1-4a).[18,19] The electron transfer occurs from highest occupied molecular orbital (HOMO) of Ru^{II} to lowest unoccupied molecular orbital (LUMO) of the pyridyl ligand, and then electrons in the singlet excited state undergoes intersystem crossing to the triplet excited state, followed by further relaxation to the ground

state.[8] The energetics between the ruthenium metal center and the pyridyl ligand and the slow kinetics for the relaxation process of the excited state made the ruthenium complexes an excellent absorber for sunlight, which opened their applicability for dye sensitized solar cells.[20] Until now, functionalizing the pyridyl ligand and coordinating different types of ancillary ligand in the ruthenium complexes have been implemented to modify MLCT and the lifetime of the excited electron in order for achieving higher efficiency for solar energy harvesting.

Understanding MMCT in dinuclear ruthenium complexes has also received much attention since the Creutz-Taube ion was synthesized in 1968 (Figure 1-4b).[1] Many successive studies demonstrated that modification of the bridging ligand could perturb delocalization of the electron density between two ruthenium centers,[21,22] and the electronic structure of the ruthenium metal centers could also be modulated by coordinating electron-donating or -withdrawing ancillary ligands.[2] The studies on MMCT have helped to learn the basics regarding the parameters that govern the intramolecular electron transfer between homogeneous redox centers and further will contribute to designing molecular electronic devices.

In contrast to the abundant studies in MLCT and MMCT, there are many fewer reports regarding LLCT in ruthenium complexes.[23-25] The only difference to MMCT is that ligands become the redox centers between which electron transfer occurs. For LLCT, the ligands should be redox-active and the metal center is capable of mediating the electron between the ligands. In one of the early reports,[23] LLCT in a ruthenium polypyridyl complex was observed in the NIR region, but due to the poor electronic coupling, the extinction coefficient was found to be very low (ε_{max} = 210 L/mol·cm). More intense LLCT could be observed in the ruthenium complexes coordinated with non-innocent ligands.[26-28] This type of ligand is, in other words, a redox-active ligand that is electronically coupled well with the metal center, and the redox events in the ligand involve the metal center. Catecholate ligand-coordinated ruthenium complexes showed strong LLCT absorption bands upon oxidation of the ligands (Figure 1-4c).

In the recent five years, the importance of LLCT has emerged in that metal-organic frameworks, organic-inorganic hybrid porous materials, could conduct electrons via a sequence of the redox-active ligand centers in the framework.[29-31] Metal-organic frameworks have, heretofore, been known as insulating porous materials, whose applications were only limited to gas storage and separation. By observing electronic conductivity over the framework, their porous properties can now be considered as useful for many other electronic applications, but it still remains to investigate the conducting mechanisms between organic and inorganic components and to develop synthetic strategies for better conductive metal-organic frameworks.

Intermolecular electron transfer

The intermolecular electron transfer could be observed largely by two pathways: (*i*) direct contact of two species in the solution phase and (*ii*) non-covalent interaction in the solid state. As mentioned earlier with the potential energy diagram, the direct contact between two molecules in different oxidation states can be regarded as the most simple route for the intermolecular electron transfer. From this simple implementation, one can study the electron transfer process with respect to reactant concentrations, solvent, and pH.

This direct-contact intermolecular electron transfer frequently takes place along with hydrogen atoms in biological and chemical energy conversion processes, which is termed as proton-coupled electron transfer (PCET).[32] PCET involves simultaneous intermolecular proton and electron transfer: M + HX → HM + X (Figure 1-5a). This concerted mechanism has been verified in that it progresses through the lowest energy pathway (or high thermodynamic favorability) compared to the other plausible mechanisms with separate electron and proton transfer. Due to its importance in biology and chemistry, many attempts to elucidate the intermolecular electron transfer mechanisms in PCET with different transition metal complexes

have contributed to an understanding of various biological and chemical phenomena such as respiration and DNA repair. Now, the study of PCET has focused on energy conversion processes in solar fuel generation and fuel cells and helped in developing better catalysts in those applications.

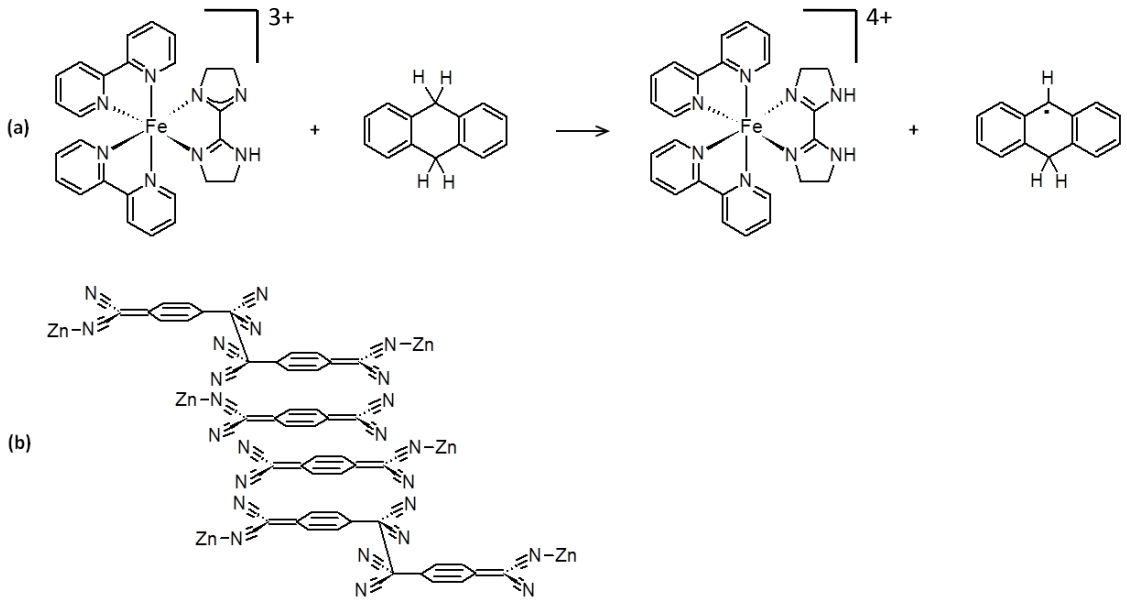

Figure 1-5: Transition metal complexes with intermolecular electron transfer (a) PCET between iron bis-imidazoline complex and dihydroanthracene from reference 33 and (b) zinc complex with π-stacked TCNQ ligands.

The intermolecular electron transfer can be found in solid-state inorganic materials with π-stacking. Although there is neither direct contact nor covalent bonding between two redox sites, the periodic alignment of the species facilitates the orbital overlap between the stacked species and electron hopping or diffusion induced by NIR energy, which indicates the intermolecular electron transfer between the stacks. As the NIR absorption energy decreases, the material is more likely to show enhanced electronic conductivity throughout the array.

One of the well-studied systems is a planar redox-active polynitrile ligand such as tetracyanoquinodimethane (TCNQ) and tetracyanoethylene (TCNE). This type of molecule is an electron acceptor with well-defined redox properties and has strong tendency toward π-stacking

when crystallized (Figure 1-5b). Consequently, transition metal complexes coordinated with those ligands are easily assembled in such stacks. Since TCNQ-TTF (TTF = tetrathiofulvalene), known as organic metal, showed unusually high conductivity (0.2 $\Omega^{-1}m^{-1}$ at 300 K) as a non-metal in 1970s, there have been a number of studies on development of conducting compounds coordinated with such ligands until now.[34] This motif, the intermolecular electron transfer through π-stacking, is now utilized as another strategy for constructing conducting metal-organic frameworks, and also applied for organic photovoltaic devices.

Electron transfer at interfaces

Analogous to the electron transfer in transition metal complexes mentioned in the previous sections, electron transfer at interfaces has become of interest for the development of devices with semiconducting nanocrystals (NCs) (Figure 1-6).

Semiconductor NCs are defined as nano-sized semiconductors that exhibit the quantum confinement effect.[35] The bandgap energy can be easily tuned by the size of the NCs as well as the composition (Table 1-1).[36,37] Along with the facile tunability of the bandgap energy, the high quantum efficiency allows the NCs to be used as bio-imaging agents.[38] They have shown superior sensitivity and resolution than conventional dye molecules in biomedical applications.

For optoelectronic devices such as solution-processed photovoltaics, the interfacial electron transfer from the NCs to the metal electrode or adsorbates has been focused more than the internal electronic transition.[39,40] When the corresponding bandgap energy is absorbed, electron-hole pairs are generated and it allows for long-range charge transfer throughout the semiconductor-assembled electronic device (the hole is considered to be a positive charge). For instance, to improve solar power-conversion efficiency in photovoltaics, it will be required to reduce energy loss during the interfacial electron transfer and transport charge carriers efficiently

via the interfaces in the device assembly. Thus, increasing investigation of such interfacial electron transfer has been implemented recently.

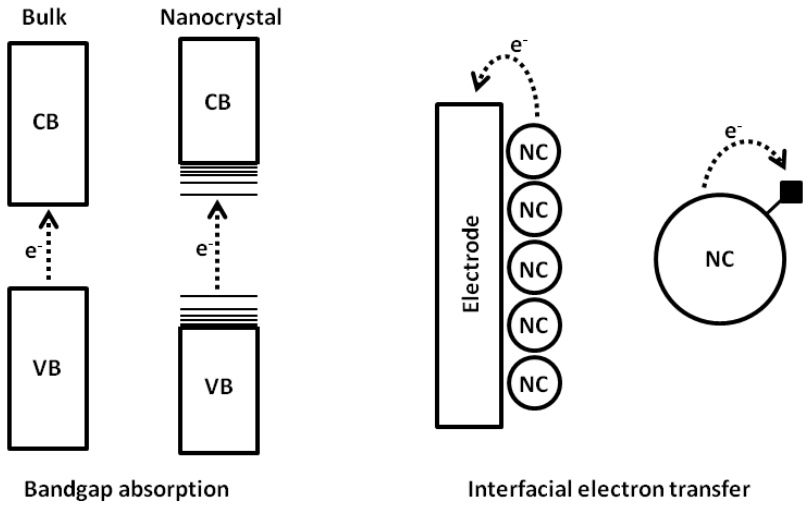

Figure 1-6: Electron transfer in semiconductor nanocrystals (CB = conduction band, VB = valence band, and NC = nanocrystal).

Table 1-1: Bandgap energy of semiconductors.

Composition	Bandgap energy	
	eV	nm
GaAs	1.4	886
CdSe	1.7	730
Fe_2O_3	2.1	590
CdS	2.4	517
ZnO	3.2	387

Motivation

One can realize that inorganic materials play an important role in transporting electrons in various practical applications such as solar energy conversion systems because they function as the redox centers at which electron transfer occurs. An attempt to improve performance of such

systems has been implemented by modifying elemental compositions or crystal structures of inorganic materials (mostly metal elements), which is expected to obtain a proper electronic structure of the material for a specific application. However, it normally requires much empirical effort if one seeks to find a new synthetic method for making different metal-based materials.

It is frequently overlooked that inorganic materials (ranging from transition metal complexes to semiconductor nanocrystals) are combined with ligands. Study of the effect of ligands to the electronic properties of inorganic materials have not been performed significantly for modifying the electronic properties of inorganic materials. Incorporation of ligands to metals can be rather easy based on the conventional fact that metal ions are acidic and ligands are electron-donating, while formation and segregation of metal-metal bonding may need more energy thermodynamically. In addition, there are a large number of ligands that can be incorporated in inorganic materials. Thus, I would suggest that it is necessary to develop a ligand-assisted methodology for modifying the electronic properties of inorganic materials.

Overview

I briefly introduced various types of electron transfer in inorganic materials and importance of such studies. Marcus theory is the foundation of understanding electron transfer, and the modified potential energy surfaces can be used for interpreting the intramolecular electron transfer between two electronically coupled redox sites. Energy level difference, orbital overlap, and distance are taken into account when predicting the degree of electronic coupling.

The intramolecular electron transfer has been studied with transition metal complexes. Many of them absorb UV-vis light that corresponds to MLCT or LMCT, and those with two metal or redox-active ligand centers may exhibit MMCT or LLCT in NIR. The intermolecular electron transfer can occur when two different species with different redox states are present in

solution, and also in the solid-state inorganic materials can show the intermolecular charge transfer band when they are crystallized via π-stacking. Likewise, understanding the interfacial electron transfer with semiconductor NC-based devices become important in order to reduce energy loss at interfaces and obtain high device efficiency.

From the following chapters, I will discuss specified electron transfer events that were observed in inorganic materials that I synthesized: hydroxypyridine-coordinated ruthenium polypyridyl complexes (Chapter 2), TCNQ-coordinated dinuclear zinc complex (Chapter 3), zinc oxide NCs with carboxylic acids (Chapter 4), and coumarin 153 encapsulated in a metal-organic framework (Chapter 5). I studied a fundamental understanding of electron transfer with molecule-scale objects in Chapter 2 and 3, and explored the photophysical properties of an extended system with the nano-sized semiconductor in Chapter 4. Lastly, I investigated the photophysical properties of small molecules in confined environment in Chapter 5. My observations with these inorganic materials will demonstrate how ligands can influence electronic structures and localization of electrons in such materials and complexes.

References

1. Creutz, C.; Taube, H. *J. Am. Chem. Soc.* **1969**, *91*, 3988-3989.
2. Kaim, W.; Klein, A.; Glockle, M. *Acc. Chem. Res.* **2000**, *33*, 755-763.
3. Launary, J. *Chem. Soc. Rev.* **2001**, *30*, 386-397.
4. Liu, F.; Concepcion, J. J.; Jurss, J. W.; Cardolaccia, T.; Templeton, J. L.; Meyer, T. J. *Inorg.Chem.* **2008**, *47*, 1727-1752.
5. Concepcion, J. J.; Jurss, J. W.; Brennaman, M. K.; Hoertz, P. G.; Patrocinio, A. O. T.; Iha, N. Y. M.; Templeton, J. L.; Meyer, T. J. *Acc. Chem. Res.* **2009**, *42*, 1954-1965.
6. Low, P. J. *Dalton Trans.* **2005**, 2821-2824.
7. Otsuki, J.; Akasaks, T.; Araki, K. *Coord. Chem. Rev.* **2008**, *252*, 32-56.
8. Vlček Jr., A. *Coord. Chem. Rev.* **2000**, *200-202*, 933-977.

9. Meyer, T. J. *Acc. Chem. Res.* **1989**, *22*, 163-170.
10. Rüttinger, W.; Dismukes, G. C. *Chem. Rev.***1997**, *97*, 1-24.
11. McEvoy, J. P.; Brudvig, G. W. *Chem. Rev.* **2006**, *106*, 4455-4483.
12. Yagi, M.; Syouji, A.; Yamada, S.; Komi, M.; Yamazaki, H.; Tajima, S. *Photochem. Photobiol. Sci.* **2009**, *8*, 139-147.
13. Lewis, N. S.; Nocera, D. G. *Proc. Natl. Acad. Sci. U.S.A.* **2006**, *103*, 15729-15735.
14. Ratner, M. *Nat. Nanotechnol.* **2013**, *8*, 378– 381.
15. Marcus, R. A. *J. Chem. Phys.* **1956**, *24*, 966-978.
16. Sutin, N. *Prog. Inorg. Chem.* **1983**, *30*, 441-498.
17. D'Alessandro, D. M.; Keene, F. R. *Chem. Soc. Rev.* **2006**, *35*, 424-440.
18. Meyer, T. J. *Acc. Chem. Res.* **1978**, *11*, 94-100.
19. Durham, B.; Caspar, J. V.; Nagle, J. K.; Meyer, T. J. *J. Am. Chem. Soc.* **1982**, *104*, 4803-4810.
20. O'Regan, B.; Grätzel, M. *Nature* **1991**, *353*, 737-740.
21. Lavalle, D. K.; Fleischer, E. B. *J. Am. Chem. Soc.* **1972**, *94*, 2583-2599.
22. Tom, G. M.; Creutz, C.; Taube, H. *J. Am. Chem. Soc.* **1974**, *96*, 7827-7829.
23. Heath, G. A.; Yellowlees, L. J.; Braterman, P. S. *Chem. Phys. Lett.* **1982**, *92*, 646-648.
24. Wang, Y.; Hauser, B. T.; Rooney, M. M.; Burton, R. D.; Schanze, K. S. *J. Am. Chem. Soc.* **1993**, *115*, 5675-5683.
25. Verma, S.; Kar, P.; Das, A.; Ghosh, H. N. *Dalton Trans.* **2011**, *40*, 9765-9773.
26. Haga, M.; Dodsworth, E. S.; Lever, A. B. P. *Inorg. Chem.* **1986**, *25*, 447-453.
27. Lever, A. B. P.; Auburn, P. R.; Dodsworth, E. S.; Haga, M.; Liu, W.; Melnik, M.; Nevin, W. A. *J. Am. Chem. Soc.* **1998**, *110*, 8076-8084.
28. Boyer, J. L.; Rochford, J.; Tsai, M.; Muckerman, J. T.; Fujita, E. *Coord. Chem. Rev.* **2010**, *254*, 309-330.
29. Kobayashi, Y.; Jacobs, B.; Allendorf, M. D.; Long, J. R. *Chem. Mater.* **2010**, *22*, 4120-4122.
30. D'Alessandro, D. M.; Kanga, J. R. R.; Caddy, J. S. *Aust. J. Chem.* **2011**, *64*, 718-722.
31. Allendorf, M. D.; Schwartzberg, A.; Stavila, V.; Talin, A. A. *Chem. Eur. J.* **2011**, *17*, 11372-11388.
32. Mayer, J. M. *Annu. Rev. Phys. Chem.* **2004**, *55*, 363-390.
33. Roth, J. P.; Lovell, S.; Mayer, J. M. *J. Am. Chem. Soc.* **2000**, *122*, 5486-5498.
34. Torrance, J. B. *Acc. Chem. Res.* **1979**, 12, 79-86.
35. Alivisatos, A. P. *Science* **1996**, *271*, 933-937.

36. Li, L.; Hu, J.; Yang, W.; Alivisatos, A. P. *Nano Lett.* **2001**, *1*, 349-351.
37. Baskoutas, S.; Terzis, A. F. *J. Appl. Phys.* **2006**, *99*, 013708.
38. Medintz, I. L.; Uyeda, H. T.; Goldman, E. R.; Mattoussi, H. *Nat. Mater.* **2005**, *4*, 435-446.
39. Tang, J.; Kemp, K. W.; Hoogland, S.; Jeong, K. S.; Liu, H.; Levina, L.; Furukawa, M.; Wang, X.; Debnath, R.; Cha, D.; Chou, K. W.; Fischer, A.; Amassian, A.; Asbury, J. B.; Sargent, E. H. *Nat. Mater.* **2011**, *10*, 765-771.
40. Sargent, E. H. *Nat. Photonics* **2012**, *6*, 133-135.

Chapter 2

Ruthenium complexes: Intramolecular electron transfer

Introduction

Numerous studies with ruthenium polypyridyl complexes have been performed to examine their electronic structure and excited state in order to tune the electronic properties that can be best-suited for light-harvesting applications.[1-3] The photo-physicochemical properties in such complexes are governed mainly by the redox processes of the ruthenium metal center. The most facile way to modulate the redox properties is to either functionalize the bipyridine ligands or coordinate different types of ancillary ligands.

It has been reported that coordinating redox-active ligands to ruthenium polypyridyl complexes can enrich their redox properties, in which the redox-active ligands allow the complexes to retain multiple redox events that originate from well-mixed orbitals between the metal center and the redox-active ligand.[4] Moreover, the good electronic coupling between the metal center and the redox-active ligand can potentially facilitate interligand electron transfer through the metal center. There are few research related to the interligand electron transfer (LLCT) in redox-active ligand-coordinated ruthenium complexes.[5-7] Fundamental questions are still not answered, about how LLCT can be affected by the oxidation state of the metal center, the type of the ancillary ligand, the structural geometry, and pH.

In this chapter, I will introduce a series of ruthenium polypyridyl complexes with a hydroxypyridine ligand (Figure 2-1), and discuss their structural, pH-dependence, electrochemical, and spectroscopic properties. The hydroxypyridine ligand is a derivative of 1,2-dihydroxybenzene, known as a redox-active ligand in the ruthenium polypyridyl complexes.

Compared to common redox-active ligands reported in literature,[4,8,9] the coordinated hydroxypyridine ligand (pid) could be modified easily by changing the substituent on the nitrogen atom to either a proton or an ethyl group. I observed that the different substituents tuned the electron density of the pid ligand as well as the ruthenium metal center. I will present changes in the electronic properties of the synthesized complexes as a function of these chemical changes and their relationship to LLCT in the ethylated complex.

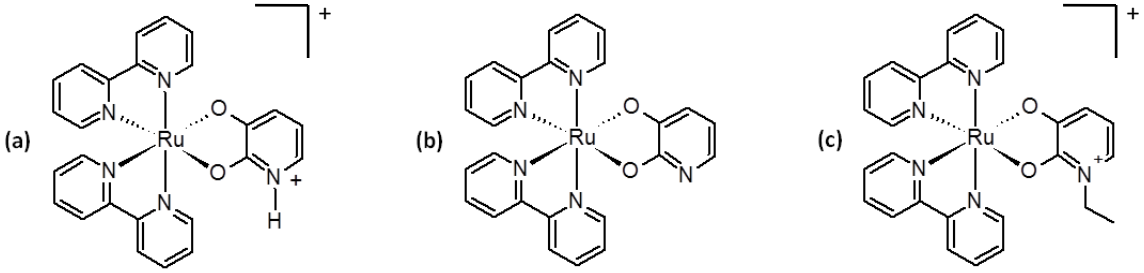

Figure 2-1: Molecular structures of (a) $[Ru(bpy)_2(pid\text{-}H)](PF_6)$ (1), (b) $Ru(bpy)_2(pid)$ (2), and (c) $[Ru(bpy)_2(pid\text{-}CH_2CH_3)](PF_6)$ (3).

Experimental

Materials and methods

2,2′-bipyridine (bpy) and sodium hydroxide were purchased from Aldrich. 2,3′-dihydroxypyridine (dhp) and sodium hexafluorophosphate were purchased from Alfa Aesar. Ruthenium (III) chloride hydrate was purchased from Oakwood Products, Inc., and anhydrous sodium sulfate was purchased from EMD. All solvents were ACS grade, and were used without further purification.

UV-visible (UV-vis) spectra were measured using an Agilent 8453 spectrometer with a 1 cm path length quartz cell. During the spectroscopic acid titration, the solution was prepared under nitrogen. For the spectroelectrochemical measurement, 1 mm path length quartz cell was

used and the experiment was performed under nitrogen. A gold honeycomb electrode card (Pine Instrument Company) was used as a working and counter electrode, and a silver chloride-coated silver wire was used as a pseudoreference electrode. 0.1 M tetra-butyl ammonium hexafluorophosphate was used as an electrolyte in dimethyl sulfoxide (DMSO). Electrochemical measurements such as cyclic voltammetry and differential pulse voltammetry were performed under nitrogen in a three-electrode cell with a silver chloride-coated silver wire as a pseudoreference electrode and two platinum wires as working and counter electrodes. Ferrocene was added at the end of the experiment as an internal standard. The potentials were converted to the saturated calomel electrode (SCE) by subtracting 0.4 V from the original values. Elemental analyses were carried out by Atlantic Microlab, Inc., Norcross, GA.

^{1}H NMR spectra were recorded by Bruker DPX-300 and DRX-400 instruments. They were calibrated using residual solvent peaks as internal reference. The NMR titration measurement was performed by dissolving 0.0080 g (0.012 mmol) of the complex in 1 mL of C_2D_6OS. The solution was titrated by adding 6 μL of 0.5 M NaOH (0.25 eq), followed by sonication for 1 min. Upon deprotonation of **1**, the color of the solution changed from purple to dark green. All of the NMR spectra were taken within 30 min of the addition of NaOH.

Synthesis of Na_2(pid)

Na_2(pid) was synthesized by combining 0.1884 g (1.70 mmol) of dhp and 0.1336 g (3.34 mmol) of NaOH with 20 mL of ethanol in a 25 mL flask. The mixture was sonicated for 5 min at room temperature. A white precipitate was produced during sonication. The solution was filtered and rinsed with 40 mL of ethanol and 30 mL of diethyl ether. The white precipitate was collected and dried under vacuum overnight to yield **1**. Yield: 0.1456 g (56%). ^{1}H NMR (300 MHz, C_2D_6OS): δ 6.52 (d, *J* = 6.8 Hz, 1H), δ 6.29 (d, *J* = 7.2 Hz, 1H), δ 5.95 (t, *J* = 7.0, 6.2 Hz, 1H).

Synthesis of [Ru(bpy)$_2$(pid-H)](PF$_6$) (1)

$Ru(bpy)_2Cl_2$ was prepared by a reported literature method.[10] The solution was prepared with 13.7 mL of ethanol and 13.7 mL of distilled water in a 50 mL flask, and was purged with nitrogen for 10 min. The protonated complex, **1**, was synthesized by combining 0.1918 g (0.396 mmol) of $Ru(bpy)_2Cl_2$ and 0.0790 g (0.543 mmol) of $Na_2(pid)$ in the prepared solution. The mixture was refluxed for 4 h under nitrogen without exposure to light. The solution was cooled to room temperature, and the solvent was evaporated to dryness. The purple solid was dissolved in 40 mL of 0.01 M HCl, and it was precipitated by $NaPF_6$. The purple precipitate was filtered and rinsed with cold 5 mL of distilled water and 30 mL of diethyl ether. Then, the purple solid was redissolved in 200 mL of dichloromethane in the presence of 0.1722 g (1.19 mmol) of Na_2SO_4. The purple solution was stirred for 1 h, and it was filtered to remove hydrated Na_2SO_4. The solvent was evaporated to dryness, and the purple product was dried under vacuum overnight. Yield: 0.1275 g (47%). Anal. Calcd (Found) for $C_{25}H_{20}N_5O_2F_6PRu\cdot H_2O$: C, 43.74 (43.73); H, 3.23 (3.13); N, 10.20 (10.17). ^{1}H NMR (400 MHz, C_2D_6OS): δ 12.56 (d, *J* = 4.6 Hz, 1H), δ 8.90 (d, *J* = 5.5 Hz, 1H), δ 8.82 (d, *J* = 5.5 Hz, 1H), δ 8.76 (d, *J* = 8.1 Hz, 2H), δ 8.63 (d, *J* = 3.8 Hz, 1H), δ 8.61 (d, *J* = 2.8 Hz, 1H), δ 8.14 (dd, *J* = 7.7 Hz, 1H), δ 8.12 (dd, *J* = 7.2, 7.6 Hz, 1H), δ 7.83 (dd, *J* = 8.5, 9.0 Hz, 1H), δ 7.81 (dd, *J* = 9.0, 9.8 Hz, 1H), δ 7.76 (dd, *J* = 6.3, 7.6 Hz, 1H), δ 7.75 (dd, *J* = 6.3, 7.0 Hz, 1H), δ 7.71 (d, *J* = 5.6 Hz, 1H), δ 7.65 (d, *J* = 5.6 Hz, 1H), δ 7.22 (dd, *J* = 6.1, 7.0 Hz, 1H), δ 7.19 (dd, *J* = 6.1, 6.9 Hz, 1H), δ 6.63 (dd, *J* = 5.7, 6.0 Hz, 1H), δ 6.52 (d, *J* = 7.5 Hz, 1H), δ 6.27 (t, *J* = 6.4, 7.3 Hz, 1H). MS [ESI (CH_2Cl_2), *m/z*]: 524.2 $[C_{25}H_{20}N_5O_2Ru]^+$.

Synthesis of Ru(bpy)$_2$(pid) (2)

It was not possible to obtain the deprotonated complex as solid with high purity. All provided results were collected in solution with NaOH. ^{1}H NMR (400 MHz, C_2D_6OS): δ 8.98 (d, *J* = 5.4 Hz, 1H), δ 8.94 (d, *J* = 5.3 Hz, 1H), δ 8.63 (d, *J* = 5.8, 6.8 Hz, 2H), δ 8.52 (d, *J* = 7.5 Hz, 1H), δ 8.50 (d, *J* = 7.6 Hz, 1H), δ 7.93 (dd, *J* = 7.5 Hz, 2H), δ 7.70 (dd, *J* = 6.9, 8.3 Hz, 1H), δ 7.68 (dd, *J* = 6.9, 7.1 Hz, 1H), δ 7.60 (dd, *J* = 5.9 Hz, 2H), δ 7.54 (d, *J* = 5.0 Hz, 2H), δ 7.12 (dd, *J* = 6.8, 7.5 Hz, 1H), δ 7.10 (dd, *J* = 6.8, 7.3 Hz, 1H), δ 6.71 (d, *J* = 3.9 Hz, 1H), δ 6.17 (d, *J* = 7.1 Hz, 1H), δ 5.88 (t, *J* = 5.7, 6.4 Hz, 1H).

Synthesis of [Ru(bpy)$_2$(pid-CH$_2$CH$_3$)](PF$_6$) (3)

A basic solution was prepared by dissolving 0.0087 g (0.218 mmol) of NaOH in 10 mL of methanol in a 25 mL flask. Deprotonation of the pid ligand was performed by adding 0.050 g (0.0728 mmol) of **1** to the NaOH solution, and it was sonicated for 2 min. The resulted purple solution was stirred in the presence of 3.3 mL of bromoethane for 2 day without exposure to light. The solvent was evaporated, and the purple solid was dissolved in 20 mL of 0.5 M NaOH. Saturated $NaPF_6$ was added to the solution to precipitate the product. It was filtered and rinsed with cold 3 mL of distilled water and 30 mL of diethyl ether. The product was dried under vacuum overnight. Yield: 0.0090 g (17%). Anal. Calcd (Found) for $C_{27}H_{24}N_5O_2F_6PRu$: C, 46.56 (46.14); H, 3.47 (3.39); N, 10.05 (10.03). ^{1}H NMR (400 MHz, C_2D_6OS): δ 8.83 (d, *J* = 5.4 Hz, 1H), δ 8.81 (d, *J* = 5.5 Hz, 1H), δ 8.76 (d, *J* = 8.2 Hz, 2H), δ 8.64 (d, *J* = 9.2 Hz, 1H), δ 8.62 (d, *J* = 9.1 Hz, 1H), δ 8.12 (dd, *J* = 7.7, 7.9 Hz, 2H), δ 7.83 (dd, *J* = 7.9, 9.6 Hz, 1H), δ 7.81 (dd, *J* = 8.1, 9.6 Hz, 1H), δ 7.73 (dd, *J* = 6.6, 6.8 Hz, 1H), δ 7.72 (dd, *J* = 6.8 Hz, 1H), δ 7.68 (d, *J* = 5.7 Hz, 1H), δ 7.65 (d, *J* = 5.7 Hz, 1H), δ 7.22 (dd, *J* = 6.3 Hz, 1H), δ 7.18 (dd, *J* = 6.5, 6.9 Hz,

1H), δ 6.85 (d, *J* = 5.8 Hz, 1H), δ 6.49 (d, *J* = 6.8 Hz, 1H), δ 6.30 (t, *J* = 6.8, 7.3 Hz, 1H), δ 3.95 (m, 1H), δ 3.81 (m, 1H), δ 0.96 (t, *J* = 7.0 Hz, 3H).

Results and Discussion

As I focus on how deprotonation and ethylation affect the properties of this complex, I begin by characterizing the parent compound (**1**). I then report the observed effects of these chemical changes.

Characterization of [Ru(bpy)$_2$(pid-H)](PF$_6$) (1)

Slow diffusion of hexane into dichloromethane resulted in formation of opaque crystals of **1** suitable for single crystal X-ray diffraction. The structure obtained from these crystals is shown in Figure 2-2. Crystals of the deprotonated or ethylated complexes could not be obtained after several attempts. For **1**, the octahedral structure is distorted, not retaining the 90° bond angles between the metal center and the coordinated atom in each ligand (Table 2A-1). There is difference in the average bond length (Ru-N) between the metal center and the nitrogen atom in the bpy ligands. The average length *trans* to the pid is shorter by 0.029 Å than that of the other two Ru-N bonds (2.054 Å). Therefore, I infer that the Ru-N bonds *trans* to each other (simultaneously *cis* to both oxygens of the pid ligand) experience a greater *cis* influence than do the Ru-N bonds which are *trans* to the oxygens. This results in longer bonds for the *cis* Ru-N bonds. In addition, both Ru-N bond lengths *trans* to the oxygens are not symmetric, for which I presume that the *ortho* oxygen of the pid ligand exerts a stronger *cis* influence than does the *meta* oxygen.

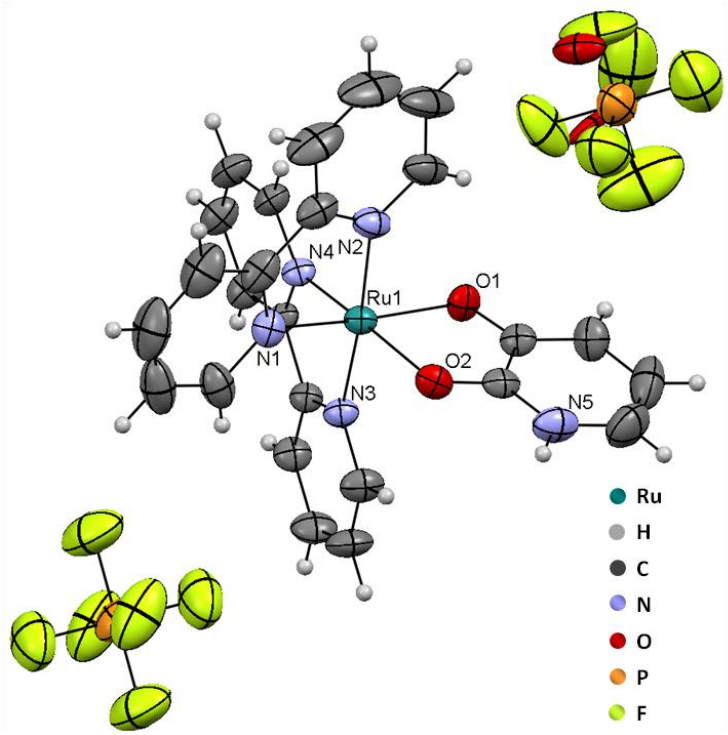

Figure 2-2: Crystal structure of **1**.

The aromatic region of the NMR spectrum of **1** is shown in Figure 2-3. The pid ligand shows its protons in the upfield range (6.0-7.0 ppm), which are assigned to H_α, H_β, and H_γ, using the literature of pyridinium ions.[11] The signal of the proton on the nitrogen of the pid ligand is observed at 12.5 ppm (Figure 2A-1). According to literature,[12] the protons in the bpy ligands of ruthenium complexes are commonly shown in 7.0-9.0 ppm. Due to the symmetry of the complex, the protons on the bpy rings are split into three groups: protons on the pyridyl rings *trans* to each other (*cis* to both oxygens of the pid ligand) belong to a single set, while the two pyridine rings *cis* to each other (*trans* to the pid) are split into two distinct groups. The reason for this is that the pyridyl rings *cis* to the pid experience near identical environments, and thus give nearly degenerate signals. At the same time, due to the electronic asymmetry of the pid ligand, the pyridine ring *trans* to the *ortho* oxygen of the pid experiences different electronic effects than the pyridine ring *trans* to the *meta* oxygen of the pid ligand. This reasoning is fully consistent with

the observed bond lengths in the crystal structure, where the lengths of Ru-N bonds *cis* to the pid are nearly identical, while the length of those *trans* to the pid ligand are distinct from each other.

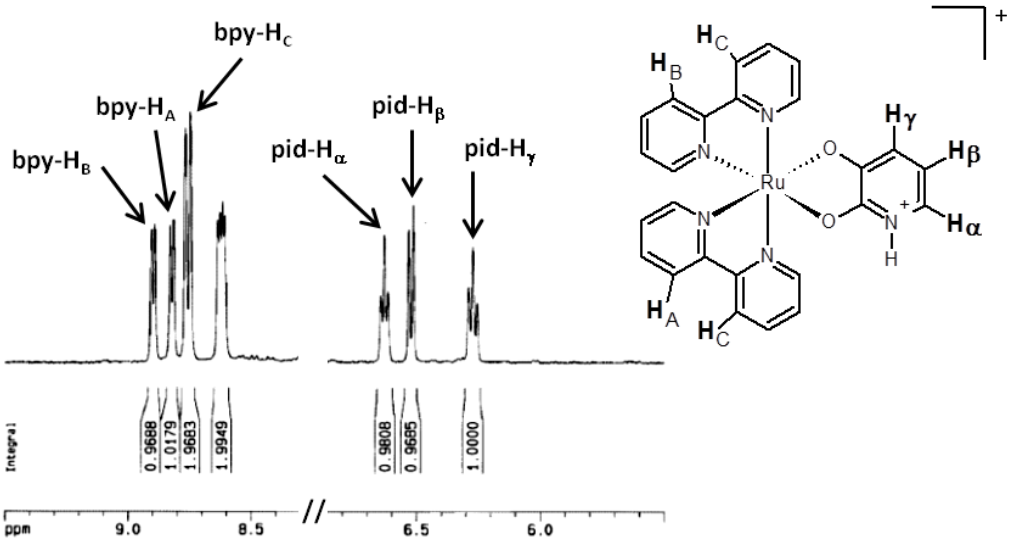

Figure 2-3: Selected NMR spectrum of **1**.

When considering the bpy ligands, it is worth focusing on the β protons (H_A, H_B and H_C in Figure 2-3), which stand well-separated from the rest of the ^1H signals and function as an assignable marker for the bpy ligands. For these protons, I can correlate the length of the Ru-N bonds with the ^1H chemical shift. The two nearly degenerate ^1H signals (H_C) are furthest upfield. These are also the moieties with the longest Ru-N bonds. From this, it seems reasonable to conclude that the further downfield signal (H_B) is attached to the ring with the shortest Ru-N bond.

The electronic absorption property of **1** was examined by UV-vis spectroscopy, which is similar to the reported properties of $Ru(bpy)_2$ derivatives.[13,14] This spectrum is the starting point before chemical modification by deprotonation and ethylation. The complex **1** exhibits four distinct absorption bands (Figure 2-4). The first two absorption bands at 245 and 293 nm correspond to two electronic transitions (π-π^{*1} and π-π^{*2}) in the bpy ligands. In the visible region, metal to ligand charge transfer (MLCT) absorption bands are shown at 360 and 513 nm, where

electrons from the ruthenium metal center are excited to the lowest unoccupied molecular orbitals (LUMO) in the ligands.

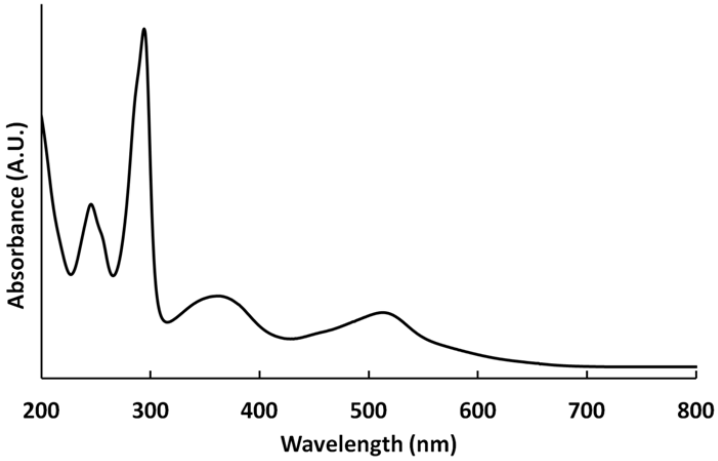

Figure 2-4: UV-vis spectrum of **1** in distilled water at 298 K.

Cyclic voltammetry and differential pulse voltammetry were performed to understand the redox properties of **1** (Figure 2-5a). In the cyclic voltammogram (CV), the reversible oxidation of Ru^{2+} (Ox_1) is recorded at 0.44 V, around which the redox event ($Ru^{2+/3+}$) typically takes place in ruthenium polypyridyl complexes.[15] In the more positive region, a second irreversible oxidation (Ox_2) was found. Figure 2-5b shows an irreversible oxidation peak (1.09 V) of the pid ligand prior to being coordinated. Based on this, it seems reasonable to ascribe the second oxidation to the pid ligand. Withdrawal of electrons from the pid ligand (upon coordination to the ruthenium metal center) gives rise to a +0.34 V shift.

The complex **1** also displays three reduction peaks (Red_1, Red_2, and Red_3). The redox event at -1.56 V (Red_1) looks reversible, but the following peaks at -1.70 V (Red_2) and -1.83 V (Red_3) appear irreversible. Based on literature,[16] I assigned Red_1 and Red_3 for the reduction of each bpy ligand. Identification for the redox event at Red_2 can be specified by Figure 2-5b, where the CV and DPV of free pid show an irreversible signal in the negative potential region (< -1.2 V). Thus, I ascribe the irreversible reduction (Red_2) of **1** to the pid ligand. Consistent with the

irreversibility of the electrochemistry of the pid ligand, instability of the reduced species of **1** did not allow for a spectroelectochemical investigation.

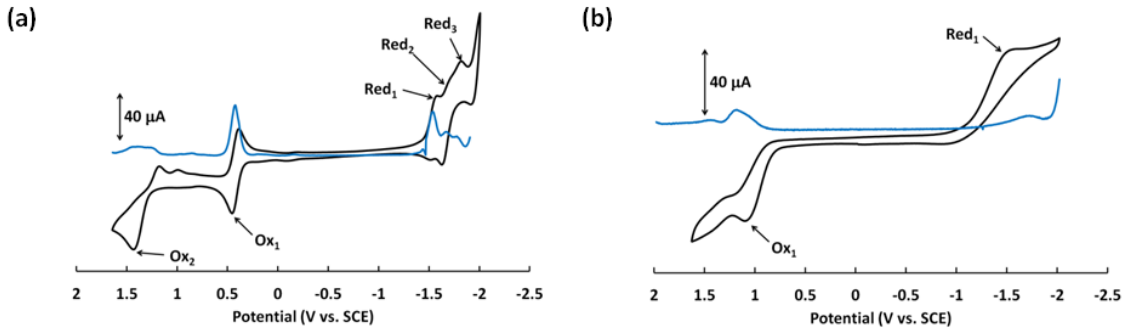

Figure 2-5: CV (black) and DPV (blue) of (a) **1** and (b) dhp in acetonitrile/0.1 M NBu_4PF_6 at 298 K. Scan rate: 100 mVs^{-1}. The current values of the blue lines are arbitrary.

Acidic properties of [Ru(bpy)$_2$(pid-H)](PF$_6$) (1)

Though the stability of the reduced species of **1** did not allow for complete characterization of the complex, I reasoned this might be due to the proton on the pid. To this end, I decided to examine the properties of the deprotonated complex **2**, in the hope that the electrochemistry would allow for complete characterization of the reduced state.

The pK_a of **1** was determined by UV-vis spectroscopic titration.[17] The complex was dissolved in distilled water, and the solution was sparged with nitrogen. The pH of the solution was increased by the addition of NaOH solution. The absorbance and pH of the solution were measured regularly until there was no change in the wavelengths of maximum absorbance. The initial pH of the solution was 6.6. As the pH of the solution increases, the wavelengths and shapes of the MLCT bands change (Figure 2-6a) and the presence of isobestic points indicates clean conversion from the protonated (**1**) to the deprotonated species (**2**). The shift of the lowest energy MLCT band at 513 nm at pH 6.6 to 540 nm at pH 12.3 is a good indicator for deprotonation of the pid ligand in **1**. These two peak positions are used to derive the pK_a value of the complex. The

percent absorbance curves in Figure 2-6b determine that the pK_a of **1** is 10.5 (pK_a = 9 for the nitrogen of the uncoordinated ligand).[18]

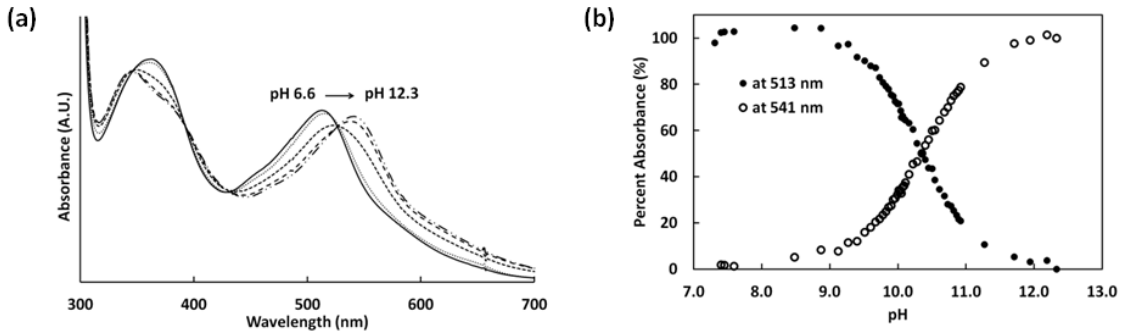

Figure 2-6: (a) Absorption spectral changes of **1** as a function of pH and (b) percent absorbance at 513 nm and 541 nm as a function of pH.

As noted above, the UV-vis spectrum of **1** closely resembles that of other bis-bpy ruthenium complexes. Thus, it seems reasonable to assume that the changes to the band at 513 nm result from changes in the energies of the Ru-d or the bpy π* orbitals. In the NMR (Figure 2-7), I observe that deprotonation of the pid ligand results in changes in chemical shifts of the bpy ligand. Thus, it is reasonable to assume that the energy of the orbitals on the bpy ligand are affected. By electrochemistry (Figure 2-8) I do not observe the reduction of the bpy ligands for the deprotonated complex, but I do observe that the Ru-based redox event is shifted more negative by 0.4 V. Thus, it seems clear that the energy of the Ru-d orbitals is also affected by deprotonation. In particular, the shift towards more negative potential is fully consistent with a red-shift in the MLCT band.[19]

Another characteristic change is shown in the MLCT absorption band at 360 nm during deprotonation. As the complex is deprotonated, the absorption band is separated into two peaks at 342 nm and 380 nm. Since this absorption occurs at higher energy than the other MLCT absorption (513 nm), it can be assigned as the electronic transition from the ruthenium metal center (dπ) to the higher energy LUMO (π^{*1}) in the bpy ligands. In the structural perspective, the

deprotonated complex (**2**) becomes relatively asymmetric than the original complex (**1**) simply due to loss of the proton at the pid ligand.[13] Thus, I ascribe this slight structural change to the perturbation of the energy level (π^{*1}) in the bpy ligands, leading to the split energy levels in π^{*1} and the occurrence of two absorption bands (342 nm and 380 nm). It is concluded that pH can control the electronic structure of the bpy ligands in complex **1**.

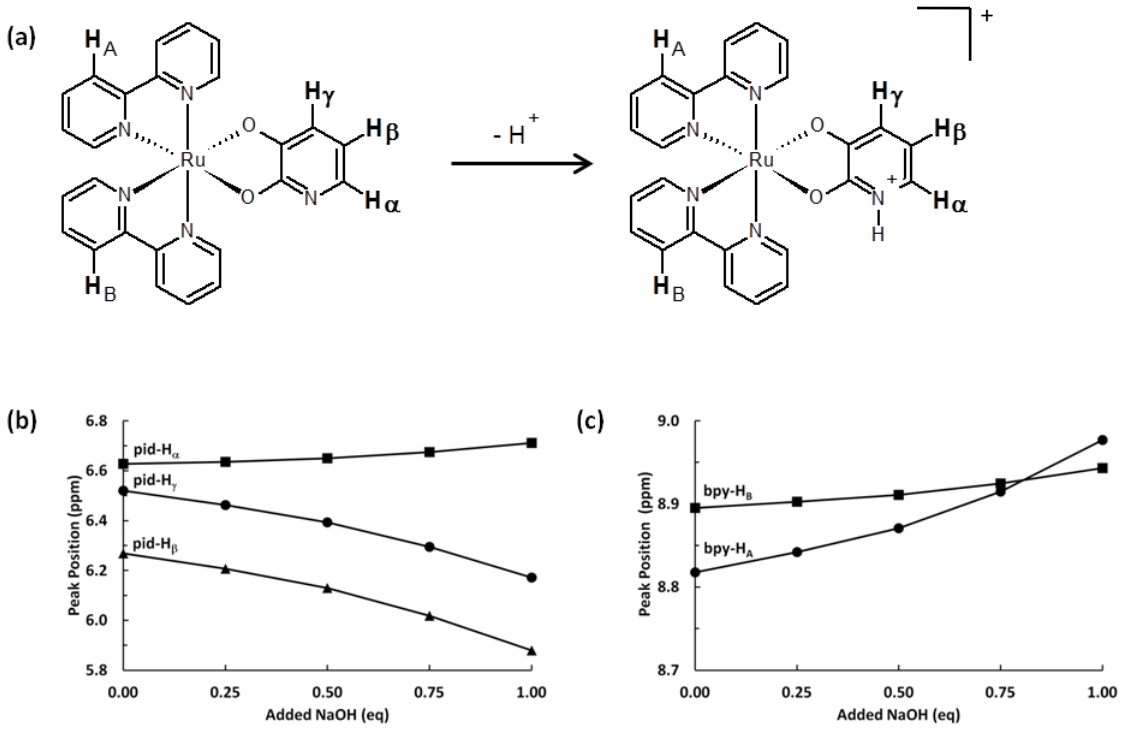

Figure 2-7: (a) Deprotonation scheme of **1**, (b) chemical shifts of the H_α, H_β, and H_γ in the pid ligand, and (c) chemical shifts of H_A and H_B in each bpy ligand.

Deprotonation of **1** resulted in large chemical shifts of the β and γ protons in the pid ligand (Figure 2-7b). The peak positions for H_β and H_γ are shifted to upfield to a larger extent (~0.4 ppm), while that for H_α is slightly shifted to downfield. This indicates that the electron density on the carbon atoms at H_β and H_γ are enriched upon deprotonation, which could also be observed in pyridinium ions. As the pyridinium ions were deprotonated, there was more shielding effect observed on H_β and H_γ than H_α.[11] From this titration study via NMR, I observed that

deprotonation exerts an analogous effect on the electron density of the pid ligand even after coordinated in the complex **1**. In addition, deprotonation of complex **1** not only affects the pid ligand, but also influences the electron density of the bpy ligands. Two proton signals (H_A and H_B) from each bpy ligand show different degrees of the pH-dependent chemical shift (Figure 2-7c). H_A becomes more de-shielded than H_B after deprotonation. It appears that the larger chemical shift in H_A might result from the *cis* influence that could be stronger to the side with the oxygen connected to the α carbon near the nitrogen.

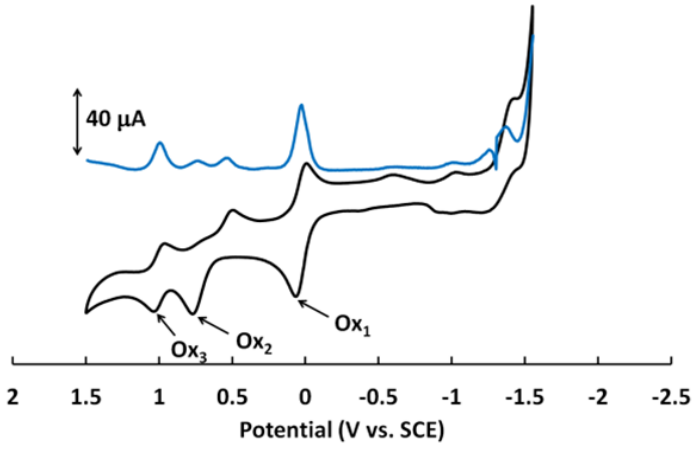

Figure 2-8: CV (black) and DPV (blue) of **2** in acetonitrile/0.1 M NBu_4PF_6 at 298 K. Scan rate: 100 mVs^{-1}. The current values of the blue lines are arbitrary.

Upon deprotonation of the pid ligand in **1**, the potentials and reversibility of the oxidation events are changed significantly (Figure 2-8). There are three oxidation events in **2**, two irreversible peaks (1.04 V and 0.75 V) and one reversible peak (0.07 V). The redox event of $Ru^{2+/3+}$ at 0.07 V is shifted 0.37 V more negative compared to that in **1**. I reason that the deprotonated pid ligand in **2** makes the ruthenium metal center more electron-rich. The second oxidation (Ox_2) seems irreversible, but the third oxidation (Ox_3) could be regarded as a reversible event. The height of the DPV of Ox_3, however, does not account for one electron oxidation event

when the signal of Ox_1 is assigned as one electron redox event of $Ru^{2+/3+}$. It is difficult to assign these events because of ambiguous peak heights and shapes.

Behaviors upon ethylation (3)

Due to the fact that neither the protonated nor the deprotonated complex displayed reversible electrochemistry, I next sought a way to generate an electrochemically well-behaved complex. For this, I turned to ethylation, reasoning that the stronger N-C bond might yield a more stable reduced species.

Changes to the molecule upon ethylation can also be tracked via NMR (Table 2-1). In this case, many of the ^1H shifts for the pid and bpy ligands are within 0.03 ppm of their positions in the protonated complex. This is not unexpected, as the same resonance structure is expected for pid-H as for pid-ethyl. The notable exceptions being the α proton on the pid ligand (0.22 ppm farther downfield than for the protonated complex) and H_B on the bpy ligand (0.07 ppm farther upfield than for the protonated complex). Thus, I would expect that, from an electronic standpoint, the protonated and ethylated complexes appear quite similar.

Table 2-1: Chemical shifts of bpy and pid in **1**, **2**, and **3**.

Complex	Chemical shift (ppm)				
	bpy-H_B	bpy-H_A	pid-H_α	pid-H_β	pid-H_γ
1	8.90	8.82	6.63	6.52	6.27
2	8.94	8.98	6.71	6.17	5.88
3	8.83	8.81	6.85	6.49	6.30

Figure 2-9 shows the CV and DPV of **3**. Two oxidation peaks are shown at 0.42 V (Ox_1) and 1.42 V (Ox_2). There is no difference in the peak positions compared to the corresponding peaks measured in complex **1** (Table 2-2). Ox_1 is reversible, and its potential is almost identical to the redox potential for $Ru^{2+/3+}$ in complex **1**. Also, Ox_2 still retains the irreversibility at the same

potential as Ox_2 in complex **1**. Thus, it can be concluded that ethylation does not affect the energy level, especially the HOMO, of the ruthenium metal center as well as the HOMO of the pid ligand.

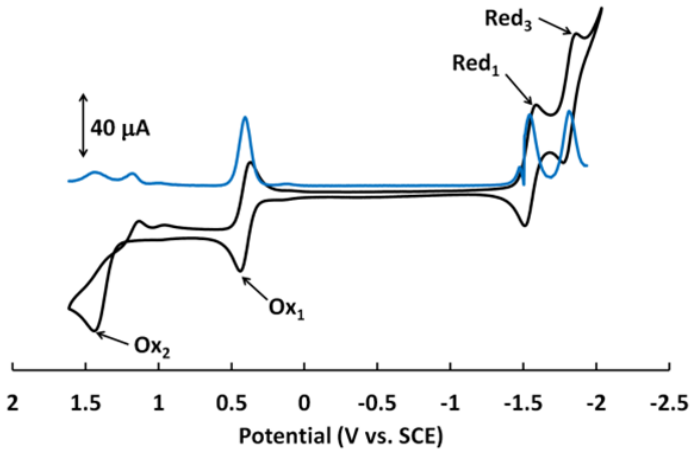

Figure 2-9: CV (black) and DPV (blue) of **3** in acetonitrile/0.1 M NBu_4PF_6 at 298 K. Scan rate: 100 mVs^{-1}. The current values of the blue lines are arbitrary.

Table 2-2: Electrochemical data from CV of **1**, **2**, and **3**.

Complex	E (V vs. SCE)				
	Ox_2	Ox_1	Red_1	Red_2	Red_3
1	1.43	0.44	-1.56	-1.70	-1.83
2	0.75	0.07	-	-	-
3	1.42	0.42	-1.57	-	-1.84
dhp	1.09	-	-	-1.51	-

On the other hand, the reduction events of **3** exhibit large differences in the shape of the curves. Only two clearly reversible reduction peaks (-1.57 V and -1.84 V) are shown, which I ascribe to the loss of Red_2. It is supposed that the electron donating property of the ethyl group can increase the LUMO energy level of the pid ligand in **3** as compared to **1**. This stronger donor strength causes more negative shift of the Red_2 (pid- $CH_2CH_3^{0/1-}$). As a result, the Red_2 could not be recorded due to the limit of the solvent window. Ethylation does not influence the reduction

behaviors of the bpy ligands, however the ethyl group imparts a stability to the singly reduced species, and this reversibility of the first and second reduction of the bpy ligands in **3** allows me to examine LLCT between the bpy^0 and bpy^{1-} ligand.

The UV-vis spectroelectrochemical behavior of **3** is shown in Figure 2-10. This measurement can allow me to understand LLCT between the bpy ligands by applying one electron on one of the bpy ligands. The ethylated complex is chosen due to its reversible redox behavior of the bpy ligands upon reduction. For the other compounds, the reduced species was not stable enough to obtain reliable spectra. Before reduction of complex **3**, the spectrum of **3** looks similar to that of the protonated form (Figure 2A-2), which is consistent with the electrochemical properties measured in both complex **1** and **3** (Table 2-2). The redox couples for $Ru^{2+/3+}$ and $bpy^{0/1-}$ do not show any changes in the potential after ethylation.

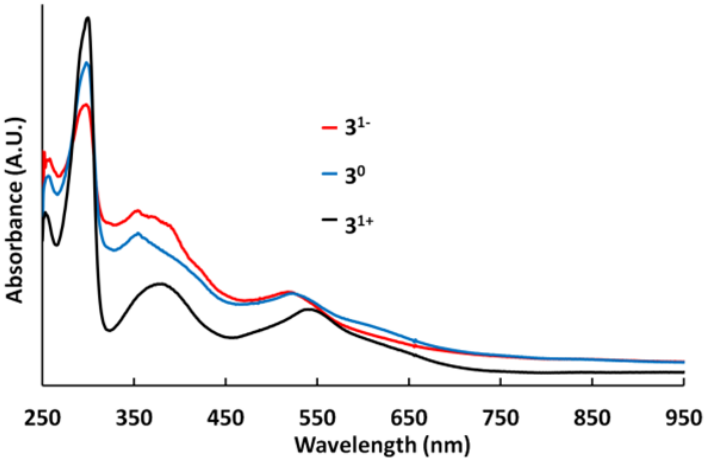

Figure 2-10: UV-vis spectroelectrochemistry of $\mathbf{3}^{1+}$ (black), $\mathbf{3}^{0}$ (blue), and $\mathbf{3}^{1-}$ (red) in DMSO/0.1 M NBu_4PF_6 at 298 K.

To generate one-electron reduced species ($\mathbf{3}^{0}$), a negative potential between Red_1 and Red_3 is applied to the electrolyte with complex **3**. Applying a more negative potential than Red_3, two-electron reduced species ($\mathbf{3}^{1-}$) can be obtained. Figure 2-10 shows three absorption spectra for each species (black for $\mathbf{3}^{1+}$, blue for $\mathbf{3}^{0}$, and red for $\mathbf{3}^{1-}$). Reduction of the bpy ligands is shown by

decrease in the intensity at 293 nm, which was also demonstrated with $[Ru(bpy)_3]^{2+}$ in literature.[20] As complex **3** is reduced, the absorption in the visible region is increased. It is known that the reduced bpy ligand starts to absorbs light around 354 nm due to π-π^{*1} transition, which can be assigned to the increasing absorption in the range of 300 nm to 450 nm in $\mathbf{3^0}$ and $\mathbf{3^{1-}}$. The MLCT absorption band is blue-shifted from 540 nm to 522 nm upon reduction, whereas $[Ru(bpy)_3]^{2+}$ was reported to have the red-shifted MLCT absorption band when reduced.

Since one of the bpy ligands is reduced in $\mathbf{3^0}$, it would be expected to observe LLCT for the electron transfer from bpy^{1-} to bpy^0. However, there is no absorption detected within the scanned wavelengths (190-1000 nm). To further investigate the LLCT absorption band in $\mathbf{3^0}$, I performed NIR spectroscopy with $\mathbf{3^0}$ which was reduced by benzophenone radical and investigated from 10000 cm^{-1} to 3000 cm^{-1} using a liquid IR cell with CaF_2 windows. However, $\mathbf{3^0}$ did not show any absorption in the wavelengths. It seems reasonable to conclude that this is a result of the LLCT being extremely weak and I conclude that my octahedral model complex with bpy and pid ligands possesses poor electronic coupling between adjacent bpy ligands.

Conclusions

A series of hydroxypyridine-coordinated ruthenium polypyridyl complexes are studied in this chapter. The starting complex **1** shows a slightly distorted octahedral geometry due to the pid ligand. Deprotonation of the pid ligand in **1** influences the electron density of all coordinated ligands, which is demonstrated by chemical shifts in the protons of the pid and bpy ligands shown in the NMR spectra. The pK_a of **1** is derived by the UV-vis titration, revealing stronger basicity than the uncoordinated pid ligand. With the deprotonated complex, increase in the electron density of the ruthenium metal center and the pid ligand is observed in the CVs, in which both of the redox peaks for $Ru^{2+/3+}$ and the pid ligand are shifted to more negative potentials. The redox

potentials of the bpy ligands, however, are not affected by deprotonation. The ethylated complex retains the redox potential for $Ru^{2+/3+}$ at the same position, but the reduction potential for the pid ligand is shifted more negatively. Thus, a stable mixed valence state of **3** can be generated and studied. The complex **1** and its ethylated one **3** do not show any significant difference in the absorption spectra, but there are shifts in the MLCT absorption bands with the deprotonated complex. Reduction of **3** is performed via the spectroelectrochemistry, and changes in the absorption can be detected due to the generation of the reduced bpy ligands, but there is no LLCT absorption observed for electron transfer between bpy^{1-} and bpy^{0} in my model complex.

References

1. Kalyanasundaram, K. *Coord. Chem. Rev.* **1982**, *46*, 159-244.
2. Allen, G. H.; White, R. P.; Rillema, D. P.; Meyer, T. J. *J. Am. Chem. Soc.* **1984**, *106*, 2613-2620.
3. Meyer, T. J. *Acc. Chem. Res.* **1989**, *22*, 163-170.
4. Boyer, J. L.; Rochford, J.; Tsai, M.; Muckerman, J. T.; Fujita, E. *Coord. Chem. Rev.* **2010**, *254*, 309-330.
5. Heath, G. A.; Yellowlees, L. J.; Braterman, P. S. *Chem. Phys. Lett.* **1982**, *92*, 646-648.
6. Wang, Y.; Hauser, B. T.; Rooney, M. M.; Burton, R. D.; Schanze, K. S. *J. Am. Chem. Soc.* **1993**, *115*, 5675-5683.
7. Verma, S.; Kar, P.; Das, A.; Ghosh, H. N. *Dalton Trans.* **2011**, *40*, 9765-9773.
8. Haga, M.; Dodsworth, E. S.; Lever, A. B. P. *Inorg. Chem.* **1986**, *25*, 447-453.
9. Lever, A. B. P.; Auburn, P. R.; Dodsworth, E. S.; Haga, M.; Liu, W.; Melnik, M.; Nevin, W. A. *J. Am. Chem. Soc.* **1998**, *110*, 8076-8084.
10. McCusker, C. E.; McCusker, J. K. *Inorg. Chem.* **2011**, *50*, 1656-1669.
11. Smith, I. C.; Schneider, W. G. *Can. J. Chem.* **1961**, *39*, 1158-1161.
12. Ji, Z.; Huang, S. D.; Guadalupe, A. R. *Inorg. Chim. Acta* **2000**, *305*, 127-134.
13. Bryant, G. M.; Fergusson, J. E.; Powell, H. K. J. *Aust. J. Chem.* **1971**, *24*, 257-273.
14. Root, M. J.; Sullivan, B. P.; Meyer, T. J.; Deutsch, E. *Inorg. Chem.* **1985**, *24*, 2731-2739.

15. Juris, A.; Balzani, V. *Coord. Chem. Rev*. **1988**, *84*, 85-277.
16. Rillema, D. P.; Allen, G.; Meyer, T. J.; Conrad, D. *Inorg. Chem.* **1983**, *22*, 1617-1622.
17. Nazeeruddin, Md. K.; Zakeeruddin, S. M.; Humphry-Baker, R.; Jirousek, M.; Liska, P.; Vlachopoulos, N.; Shklover, V.; Fischer, C.-H.; Gratzel, M. *Inorg. Chem.* **1999**, *38*, 6298-6305.
18. Grachev, V. T.; Zaitsev, B. E.; Dyumaev, K. M.; Smirnov, L. D.; Avezov, M. R. *Chem. Heterocycl. Compd.* **1973**, *9*, 47-50.
19. Das, S.; Saha, D.; Karmakar, S.; Baitalik, S. *J. Phys. Chem. A* **2012**, *116*, 5216-5226.
20. Heath, G. A.; Yellowlees, L. J. *J. Chem. Soc., Chem. Commun.* **1981**, 287-289.

Appendix for Chapter 2

Table 2A-1: Selected bond lengths (Å) and angles (°) for **1**.

Bond length (Å)		Bond angle (°)	
C5-C6	1.471(12)	N1-Ru1-N2	79.0(2)
C5-N1	1.360(9)	N1-Ru1-N3	99.2(2)
C6-N2	1.345(10)	N1-Ru1-O2	94.95(19)
C15-C16	1.477(8)	N2-Ru1-O1	93.1(2)
C15-N3	1.342(8)	N2-Ru1-O2	92.2(2)
C16-N4	1.370(8)	N3-Ru1-O1	89.2(2)
C21-C26	1.437(9)	N3-Ru1-O2	93.09(19)
C21-O2	1.279(8)	N4-Ru1-N1	92.1(2)
C26-O1	1.291(8)	N4-Ru1-N2	95.5(2)
O1-Ru1	2.090(5)	N4-Ru1-N3	79.4(2)
O2-Ru1	2.120(4)	N4-Ru1-O1	94.09(18)
N1-Ru1	2.040(6)	O1-Ru1-O2	79.80(17)
N2-Ru1	2.053(6)		
N3-Ru1	2.054(5)		
N4-Ru1	2.010(5)		

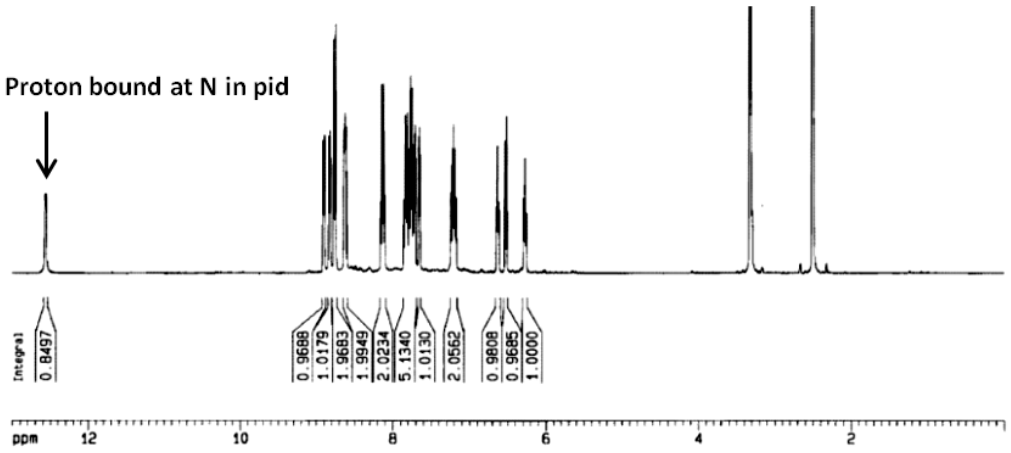

Figure 2A-1: Full NMR spectrum of **1**.

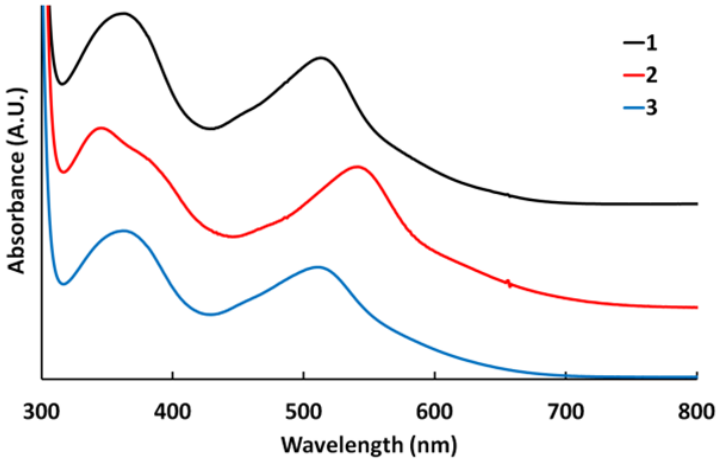

Figure 2A-2: UV-vis spectra of **1** (black), **2** (red), and **3** (blue) in distilled water at 298 K.

Chapter 3

Zinc dimer complex: Intermolecular electron transfer

Introduction

Materials based upon ordered assemblies of TCNQ (TCNQ = tetracyanoquinomethane) have long been of interest for their electronic and magnetic properties.[1-5] One of the first examples is a TTF-TCNQ charge-transfer salt (TTF = tetrathiafulvalene),[6] and its strikingly high conductivity initiated a field of study into the properties of TCNQ-based charge-transfer compounds. Typically, the relatively large π area and high acidity of TCNQ facilitate π-stacking with itself or electron-rich molecules. Assemblages of such stacks can lead to intermolecular electron transfer with NIR energy, and allow unexpected electrical conductivity and magnetic susceptibility.[7]

Furthermore, incorporation of TCNQ in transition metal complexes has widened the choice of parameters that affect π-stacking patterns and electronic structure of TCNQ and consequently control the intermolecular electron transfer between the TCNQ ligands.[8,9] In such complexes, a radical form of TCNQ is coordinated to a metal center. Crystals grown of these complexes often form in a manner allowing for π-stacked TCNQ arrays. A number of studies focused on the development of conducting metal complexes with TCNQ have been performed on this motif and have demonstrated that electronic conductivity can be created through π-stacked layers of TCNQ ligands.[10-15]

To extend the type of π-stacking pattern and obtain potential controllability in such stacked materials, one can utilize the σ-dimerized form of TCNQ, $[TCNQ\text{-}TCNQ]^{2-}$.[16-21] This

dimer is composed of two TCNQ molecules in which a carbon atom in one of the methylene units is bonded to the one in the other TCNQ. Due to pairing of electrons, the dimer becomes diamagnetic even though it is composed of two TCNQ radicals. Unlike a simple planar geometry of $TCNQ^-$, $[TCNQ\text{-}TCNQ]^{2-}$ forms a staircase geometry, which can help formation of various structures in crystals, but which impedes electrical conductivity.

Despite the unique structure and potential versatility of $[TCNQ\text{-}TCNQ]^{2-}$, I found only three molecular transition metal compounds with $[TCNQ\text{-}TCNQ]^{2-}$ that have been reported in literature in contrast with relative abundance of those incorporating $TCNQ^-$.[16,19,21] Even in those compounds, $[TCNQ\text{-}TCNQ]^{2-}$ is combined as an anion to the metal complex cation. The presence of $[TCNQ\text{-}TCNQ]^{2-}$, however, could result in different magnetic properties that have not been obtained with TCNQ radicals. Hoffmann et al. reported that $[Cu(DMP)_2]_2[TCNQ\text{-}TCNQ]$, where DMP = bis(2,9-dimethyl-1,10-phenanthroline), showed a strong triplet-state EPR signal induced from $[TCNQ\text{-}TCNQ]^{2-}$.[19] Thus, if $[TCNQ\text{-}TCNQ]^{2-}$ can be coordinated to a metal site, one might gain even more control over the properties of $[TCNQ\text{-}TCNQ]^{2-}$ and tune electronic and magnetic properties via π-stacking with $[TCNQ\text{-}TCNQ]^{2-}$ in the solid state.

Herein I will discuss the synthesis and properties of a novel [TCNQ-TCNQ]-bridged dinuclear zinc complex with 2,2′-bipyrimidine (**Zn dimer**). To the best of my knowledge, there has not been any single transition metal complex coordinated with $[TCNQ\text{-}TCNQ]^{2-}$ reported so far. Below, I will provide the details of intermolecular electron transfer with this molecule optically and magnetically in the solid state and solution phase.

Experimental

Materials and methods

Zinc nitrate hexahydrate was purchased from Strem Chemicals. TCNQ and lithium iodide were purchased from Alfa Aesar. 2,2'-bipyrimidine (bpym) was purchased from Aldrich. All solvents were ACS grade, and were used without further purification. Dimethylformamide (DMF) was dried over activated 4Å molecular sieves prior to use in the chemical reduction and electrochemistry studies.

X-ray intensity data were collected at 298(2) K, on a Bruker SMART APEX CCD area detector system equipped with a graphite monochromator and a MoK_α fine-focus sealed tube (λ = 0.71073Å) operated at 1600 watts power (50 kV, 32 mA). The detector was placed at a distance of 5.8 cm from the crystal. A total of 1650 frames were collected with a scan width of 0.3º in ω and an exposure time of 20 seconds/frame. The total data collection time was about 15 hours. The frames were integrated with the Bruker SAINT software package using a narrow-frame integration algorithm. The structure was solved and refined using the Bruker SHELXTL (Version 6.1) Software Package.

Infrared (IR) spectra were acquired using a Perkin-Elmer Spectrum 400 FT-IR/FT-NIR spectrometer with an attenuated total reflectance (ATR) crystal. UV-visible (UV-vis) spectra were measured using an Agilent 8453 spectrometer with a 1 cm path length quartz cell. All preparation for chemical reduction was performed in a glove box, and a liquid IR cell with CaF_2 windows was used for these IR and UV-vis spectra. Chemical reduction was performed in dry DMF using cobaltocene ($CoCp_2$) solution. Upon addition of 4 eq. of $CoCp_2$, the solution turned from dark green to light greenish yellow. UV-vis-near infrared (NIR) diffuse reflectance spectra were measured using a Perkin-Elmer Lambda 950 UV-Vis-NIR spectrophotometer. Scanning

electron microscopic (SEM) images were acquired by a FEI Quanta 200 environmental scanning electron microscope. Elemental analyses were carried out by Atlantic Microlab, Inc., Norcross, GA.

Electrochemical measurements, including cyclic voltammetry and differential pulse voltammetry, were performed under a nitrogen atmosphere in a three-electrode cell with a silver chloride-coated silver wire as a pseudoreference electrode and two platinum wires as a working and a counter electrode, respectively. 0.1 M tetra-butyl ammonium hexafluorophosphate in dry DMF was used as an electrolyte. Ferrocene (Fc) was added at the end of the experiment as an internal standard. The reported potentials were calculated by setting the half-wave potential of $Fc^{0/1+}$ as 0 V.

Continuous wave electron paramagnetic resonance (EPR) spectra were measured on a Bruker ESP300 X-band EPR spectrometer equipped with Bruker SHQE resonator. Measurements were performed at room temperature using following experimental settings: MW frequency, 9.495 GHz for **Zn dimer** and 9.478 GHz for TEMPO ((2,2,6,6-tetramethylpiperidin-1-yl)oxl); MW power, 20 mW; Modulation amplitude, 1 G; Scan time, 60 s; Number of Points, 4096; Time Constant, 40.96 ms. Rabi oscillation experiments were performed on a Bruker E580 X-band pulsed EPR spectrometer equipped with a Bruker ER 4118X-MS5 resonator (which was fully overcoupled for the experiments) and an Applied Systems Engineering 1 kW traveling wave tube (TWT) amplifier (model 117x). Temperature was maintained using an Oxford CF935 helium flow cryostat. Measurements were performed using a three pulse sequence: [Pinv]-Tdelay-[Pdet]-tau-[Pdet], in which two detection pulses [Pdet] were fixed at 16 ns and the inversion pulse [Pinv] was varied from 4 ns to 800 ns. Delay Tdelay = 2000 ns, and tau = 200 ns. Other experimental settings: Repetition time, 200 μs; Temperature, 100 K; MW frequency, 9.553 GHz; Shoots per point, 100. Obtained results were compared to *Standard Coal Sample* provided by Bruker. All samples were measured in 2.8 mm O.D./1.8 mm I.D. Clear Fused Quartz sample tubes.

Synthesis of Li(TCNQ)

Li(TCNQ) was prepared by a reported literature method.[22] TCNQ (1.02 g, 5.00 mmol) was refluxed in dry acetonitrile (100 mL) under argon. LiI (2.00 g, 14.9 mmol) was refluxed in 5 mL dry acetonitrile under argon. The LiI solution was transferred to the TCNQ solution. The mixture was stirred for 5 min and cooled down to room temperature. Precipitated purple solid was washed and filtered with acetonitrile and diethyl ether. Then, it was dried under vacuum overnight. Yield: 1.03 g (97%). Anal. Calcd (Found) for $C_{12}H_4N_4Li$: C, 68.27 (67.98); H, 1.91 (2.03); N, 26.54 (26.48).

Synthesis of Zn dimer

Zn dimer was prepared by a modified method from literature.[23] Li(TCNQ) (0.0105 g, 0.050 mmol) was dissolved in methanol (4 mL) in a 20 mL vial. Bpym (0.0158 g, 0.100 mmol) was dissolved in methanol (1 mL) in a 20 mL vial. Both solutions were mixed together and sonicated. $Zn(NO_3)_2{\cdot}6H_2O$ (0.0180 g, 0.061 mmol) was dissolved in methanol (3 mL) in a 20 mL vial. The zinc solution was transferred to a borosilicate glass tube (15 x 85 mm). The green solution with Li(TCNQ) and bpym was slowly transferred to the top of the zinc solution in order to obtain two separate layers. Slow diffusion was allowed for 1 day, and purple plates were formed at the middle of two layers in the glass tube. The purple plates were washed and filtered by a funnel with methanol. It was dried under vacuum. Its ^{1}H NMR spectrum in deuterated dimethyl sulfoxide showed signals that could not be quantified correctly with respect to the number of protons in TCNQ and bpym ligands, due to paramagnetism caused by TCNQ radicals. Yield: 0.0709 g (32%). Anal. Calcd (Found) for $C_{80}H_{40}N_{32}Zn_2{\cdot}2CH_3OH$: C, 58.56 (58.16); H, 2.94 (2.93); N, 27.26 (27.09).

Results and Discussion

Solid state properties

Slow diffusion of the reactants yielded leaf-like purple crystalline plates of **Zn dimer**. SEM images show that large crystals are made of long and narrow plates with sharp ends (Figure 3-1). The width of the plates ranges from 240 μm to 360 μm. Their estimated thickness is 60 μm.

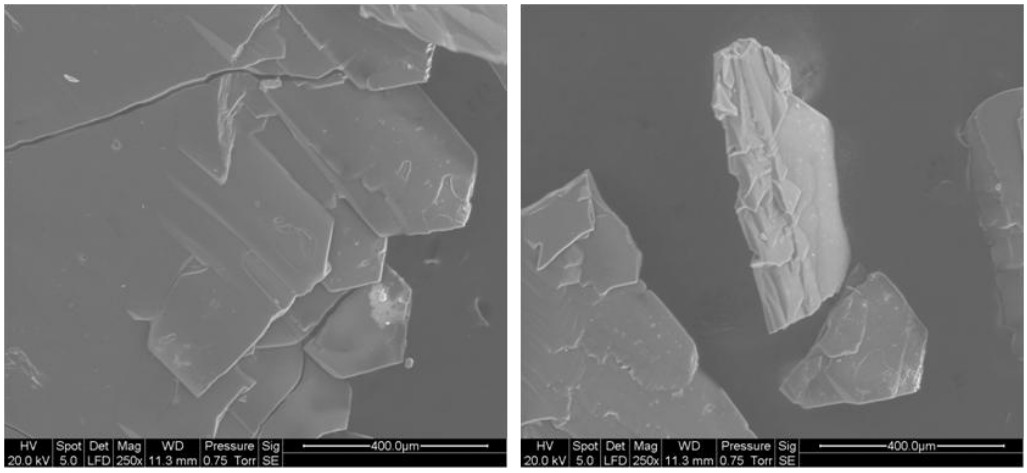

Figure 3-1: SEM images of **Zn dimer**.

Single crystal X-ray diffraction revealed that two zinc metal centers are bridged by a dimerized TCNQ ligand and the other coordination sites at each zinc center are bonded with one single $TCNQ^-$ ligand and two bpym ligands, completing the octahedral geometry in each moiety (Figure 3-2). Each bpym ligand is *trans* disposed to either a $TCNQ^-$ ligand or a $[TCNQ\text{-}TCNQ]^{2-}$ ligand. The C-C bond length (1.629 Å) in the $[TCNQ\text{-}TCNQ]^{2-}$ ligand is relatively shorter than the regular C-C bond length. My synthesis produced only one isomer of **Zn dimer** in which both metal sites have a Λ twist about the metal center.

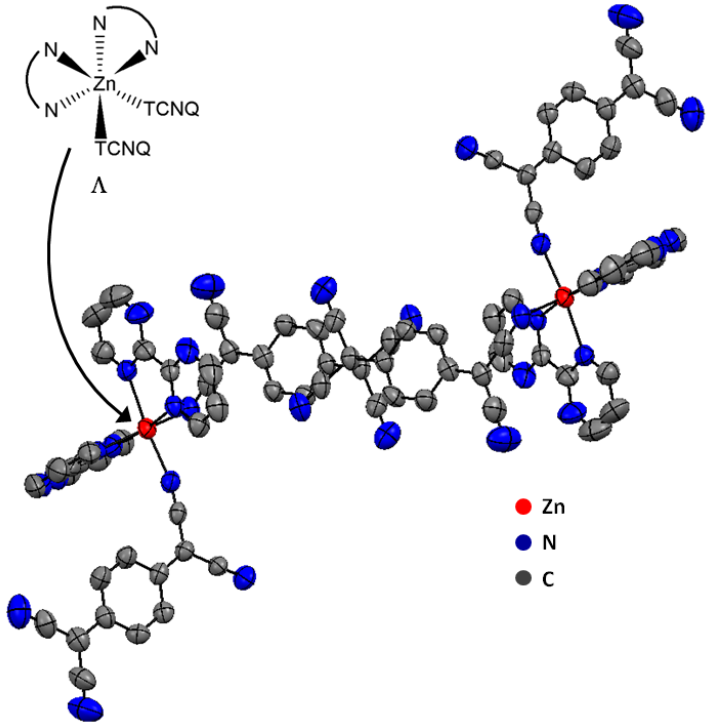

Figure 3-2: Crystal structure of **Zn dimer** in the *bc* plane.

I can gain further insight into the nature of the TCNQ ligands by considering the bond lengths (Figure 3-3), which are a useful tool for determining the charge on TCNQ derivatives by the Kistenmacher relationship (Equation 3-1).[24] For **Zn dimer** this approach is complicated by the fact that only one of the nitrogen atoms in a TCNQ molecule is coordinated to a zinc metal center, and b, c, and d values vary by their positions with respect to the metal center. To estimate the charge on each ligand, averaged bond lengths are used for each variable (b, c, and d) and the calculation reveals -1.27 for the charge of $TCNQ^{-}$ and -2.14 for that of $[TCNQ\text{-}TCNQ]^{2-}$. These estimated values are similar to their theoretical charge.

$$\rho = A[c / (b + d)] + B \quad (A = -41.667, B = 19.833) \qquad \text{(Equation 3-1)}$$

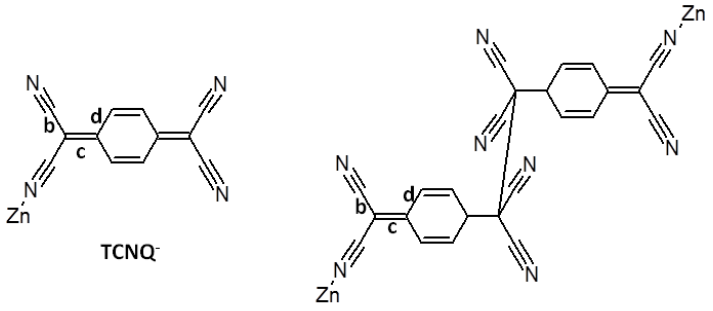

Ligand	Charge	b (Å)	c (Å)	d (Å)	ρ (charge)
$TCNQ^-$	-1	1.400	1.425	1.414	-1.27
$[TCNQ\text{-}TCNQ]^{2-}$	-2	1.428	1.487	1.392	-2.14

Figure 3-3: Molecular structures and averaged bond lengths (b, c, and d) in $TCNQ^-$ and $[TCNQ\text{-}TCNQ]^{2-}$ of **Zn dimer**.

Beyond X-ray analysis, the IR spectra of TCNQ-coordinated compounds also contain information concerning nature of $TCNQ^-$ and $[TCNQ\text{-}TCNQ]^{2-}$. According to literature,[25] the δ(C-H) bend mode in the ring of the TCNQ is helpful for distinguishing $TCNQ^-$ (shown at 827 cm^{-1}) from $[TCNQ\text{-}TCNQ]^{2-}$ (shown at 804 cm^{-1}). As expected, two characteristic peaks are detected at 804 cm^{-1} and 824 cm^{-1} with **Zn dimer** (Figure 3-4), re-confirming the presence of both types of the TCNQ ligands obtained from single X-ray diffraction. In addition, the ν(C≡N) stretch modes of the TCNQ ligands in **Zn dimer** are red-shifted compared to those in the uncoordinated TCNQ and $TCNQ^-$ molecules. The decreased vibration frequency of the TCNQ ligands in **Zn dimer** might be attributed to accumulation of the electron density donated from the metal center into the ligands. This supports the X-ray structure with assigned charges greater than -1 and -2 for $TCNQ^-$ and $[TCNQ\text{-}TCNQ]^{2-}$, respectively.

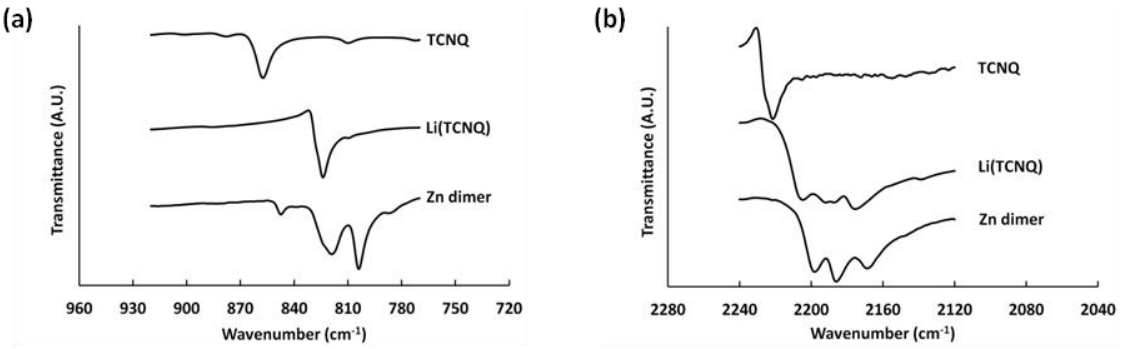

Figure 3-4: (a) δ(C-H) and (b) ν(C≡N) modes of TCNQ, Li(TCNQ), and **Zn dimer**.

The assignment of the charges to the $TCNQ^-$ and $[TCNQ\text{-}TCNQ]^{2-}$ is important because **Zn dimer** is the first example of a single molecule incorporating both a $TCNQ^-$ and a $[TCNQ\text{-}TCNQ]^{2-}$ at the same metal center. The other reports of metal centers coordinating σ-dimerized TCNQ ligands have been metal-organic frameworks.[25-28] Of particular relevance to **Zn dimer** is a recent report of one-dimensional chains of zinc and 4,4'-bipyridine (4,4'-bpy) with continuous π-stacking of coordinated and uncoordinated TCNQ molecules.[23] At each zinc metal center, all four equatorial coordination sites are monodentated with two $TCNQ^-$ and two methanol molecules respectively. Another uncoordinated TCNQ molecule is located between two coordinated $TCNQ^-$ ligands from neighboring chains so as to form a stable π-stacking structure, which is expanded along with zinc and 4,4'-bpy chains.

I obtained **Zn dimer** by a slight modification of the synthesis of the above metal-organic framework, in which I substituted a bpym ligand instead of 4,4'-bpy. I presume that the bidentating characteristic of the bpym, as well as lowered basicity of uncoordinated nitrogen atoms in the bpym, hindered continuous binding between zinc atoms and those ligands. It is not surprising that such a small change should result in a drastic difference in structure; slight changes in synthetic conditions such as concentration, solvent, and atmosphere have produced completely different structures even though the components were identical.[23,27,28]

Moving beyond the structure of the individual molecules, it is important to consider the stacking of these molecules in three dimensions (Figure 3-5). The stacking of TCNQ ligands revealed in the solid state means that I might expect electronic interactions in **Zn dimer**. In addition, the stacking can cause magnetic coupling between adjacent TCNQ ligands, which controls magnetic susceptibility of the compound. The packing diagram of **Zn dimer** in the *ab* plane shows that $TCNQ^-$ and $[TCNQ\text{-}TCNQ]^{2-}$ are stacked against each other. Stacks are formed as a series of zigzags, in which two $TCNQ^-$ ligands face each other at a distance of 3.15 Å, and two $[TCNQ\text{-}TCNQ]^{2-}$ ligands are located 3.72 Å away from each $TCNQ^-$ ligand. I tentatively assign these four TCNQ ligands as one unit, and they are all coordinated to different metal centers.

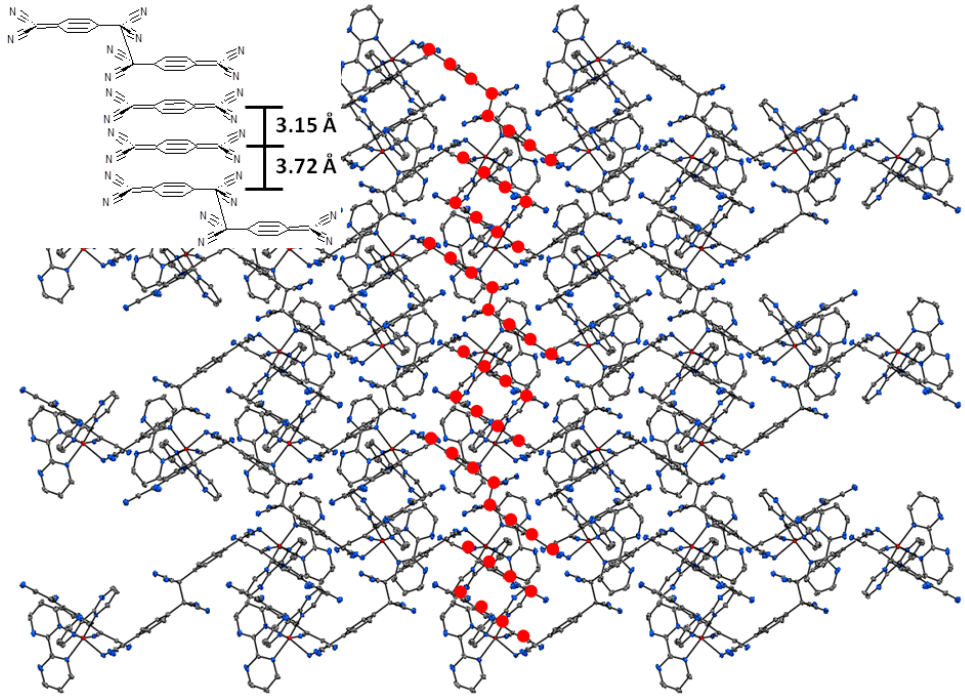

Figure 3-5: Packing diagram of **Zn dimer** in the *ab* plane.

The UV-vis-NIR diffuse reflectance spectrum of **Zn dimer** (Figure 3-6) provides insights into electronic effects resulting from this stacking. The spectra of **Zn dimer** and Li(TCNQ) were measured in the solid state. Three distinct bands are observed for **Zn dimer**, which resemble

those of Li(TCNQ). The spectrum of solid Li(TCNQ) is different from the TCNQ radical in solution. However, when the TCNQ radicals become concentrated in aqueous solution, new absorption bands arise at 27100, 16181, and 8197 cm^{-1} as shown in the spectrum of solid Li(TCNQ),[29] which is a result of the π-stacking of TCNQ radicals.[30] Li(TCNQ) exhibits a low-energy absorption band at 8197 cm^{-1}, which is normally assigned to the charge transfer (CT) between TCNQ radicals through π-stacking. Likewise, **Zn dimer** shows a CT band at 9141 cm^{-1}, which is higher by 1000 cm^{-1} than Li(TCNQ). The CT band in **Zn dimer** is anticipated from the packing diagram that demonstrates the presence of π-stacking between $TCNQ^-$ and $[TCNQ\text{-}TCNQ]^-$.

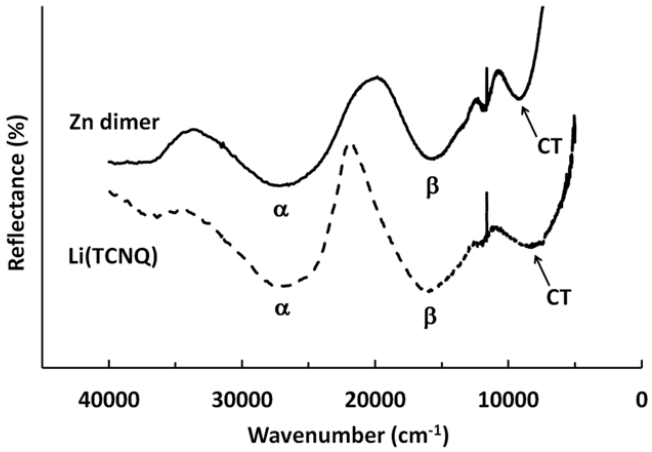

Figure 3-6: UV-vis-NIR diffuse reflectance spectra of **Zn dimer** (solid) and Li(TCNQ) (dotted) in the solid state.

Two possible factors might be taken into consideration to understand the blue shift of the CT band in **Zn dimer**. For **Zn dimer** the discontinuous staircase-shaped stacking of the TCNQ ligands could hinder the coupling of adjacent TCNQ radicals, whereas TCNQ salts such as Li(TCNQ) and K(TCNQ) retain a continuous chain of TCNQ radicals. Disruption of the π-stacking perturbs the band structure that would result from this stacking. This, necessarily, results in the blue shift for the CT transition. Also, the intermolecular spacing of the TCNQ radicals that

are π-stacked could also disrupt emergence of the bands. In general, the intermolecular spacing of TCNQ salts is reported as 3.4-3.5 Å.[30] Even though the spacing between two $TCNQ^-$ ligands in **Zn dimer** is smaller (3.15 Å) than this, the relatively large spacing (3.72 Å) between $TCNQ^-$ and $[TCNQ\text{-}TCNQ]^{2-}$ would result in the disruption in any long-range interactions in the solid. It is most likely a combination of the staircase motif and the alternating distances in the stacks that yield the higher energy intermolecular CT band of the TCNQ ligands.

The zigzag-shaped π-stacking and this high energy CT transition led me to anticipate poor electronic coupling in crystals of **Zn dimer**, which would result in high resistivity. The measured conductivity of **Zn dimer** is 7 orders of magnitude lower than that of Li(TCNQ).[22,31] I conclude that **Zn dimer** is an insulating material with a specific resistivity of 10^{12} ohm·cm.

The magnetic properties of **Zn dimer** were measured using EPR spectroscopy. **Zn dimer** exhibits a single isotropic signal with a g-value of 2.0059 (Figure 3-7a). The signal originates from either the single $TCNQ^-$ ligands coordinated to the metal center or any unbound $TCNQ^-$ species in crystals. To identify the paramagnetic signal, Rabi oscillation was performed to identify the spin state in **Zn dimer**. Figure 3-7b shows that the spin state observed in **Zn dimer** is a doublet (S = ½).

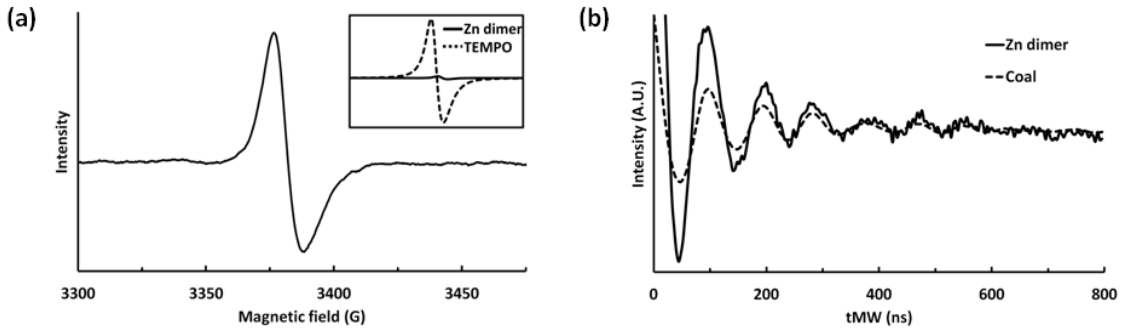

Figure 3-7: (a) EPR spectrum of **Zn dimer** at room temperature (the inset shows the overlaid spectra of **Zn dimer** and TEMPO) and (b) **Zn dimer** and coal (S = ½) via Rabi oscillation at 100 K.

Since I did not predict any paramagnetic signal in **Zn dimer** based on the fact that two $TCNQ^-$ ligands are closely stacked together and there are no other components with unpaired spins, I measured the EPR of TEMPO and compared the integrated area of its signal with that of **Zn dimer** in order to verify the number of unpaired spins present in **Zn dimer**. Both of the solid materials show isotropic spectra (Figure 3-7a inset). The double integral values identify that the number of unpaired spins in **Zn dimer** is counted as 0.096, which is expected to be 2 if the two single $TCNQ^-$ ligands did not have any spin coupling in **Zn dimer**. This ratio might imply that 5% of the total $TCNQ^-$ ligands are not π-stacked, or are defected in the crystals. Thus, I conclude that the paramagnetic signal arose from low level impurities in **Zn dimer** such as lattice defects, and there is strong antiferromagnetic coupling between the two π-stacked $TCNQ^-$ units found within the crystal-packing diagram with no further coupling between the stack of $TCNQ^-$ and $[TCNQ\text{-}TCNQ]^{2-}$.

In total, I find that the TCNQ ligands have much influence on the properties of **Zn dimer** in the solid state. Specifically, the π-stacking of the TCNQ ligands dominates the electronic and magnetic properties of **Zn dimer**. The UV-vis-NIR spectrum of **Zn dimer** mainly reflects the absorption of the TCNQ ligands and the extent of the stacking. Finally, the magnetic properties of the complex could be explained by antiferromagnetic coupling induced between the $TCNQ^-$ ligands.

Solution-phase behavior

Zn dimer provides the opportunity – for the first time – to investigate the properties of a metal-coordinated $[TCNQ\text{-}TCNQ]^{2-}$ in solution. However, as will be shown, I believe that **Zn dimer** undergoes disproportionation, releasing $TCNQ^-$ in solution, making it difficult to provide

definitive discussion of the properties of this complex in solution. Nonetheless, there are some statements that can be made, and I take this opportunity to extract what insight I can.

The first evidence that the molecule disproportionates is provided by the electrochemistry of **Zn dimer** in DMF, which shows its redox properties identical to Li(TCNQ).[32] Both cyclic voltammogram (CV) and differential pulse voltammogram (DPV) of **Zn dimer** display two redox events at -0.18 V and -0.77 V in $E_{1/2}$ with good reversibility (Figure 3-8). The number of electrons involved in each redox event was counted as four based on titration of the solution with ferrocene. This might also provide evidence for disproportionation, as the electrostatic repulsion associated with simultaneous reduction of both $TCNQ^-$ molecules in the $[TCNQ\text{-}TCNQ]^{2-}$ moiety would be expected to result in a splitting of the electrochemical processes. Furthermore, there is no difference in the peak-to-peak separation for **Zn dimer** and Li(TCNQ) respectively, indicating that the two waves are associated with a one-electron process. Thus, in total, the electrochemistry is highly suggestive of **Zn dimer** releasing four TCNQ molecules from its structure in solution.

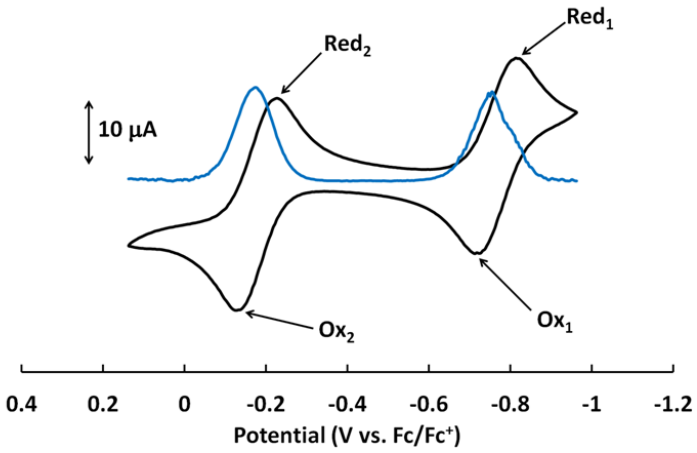

Figure 3-8: CV (black) and DPV (blue) of **Zn dimer** in DMF/0.1 M NBu_4PF_6 at 298 K. Scan rate: 100 mVs^{-1}. The current value of the blue curve is arbitrary.

Insight into this behavior can be gained from the IR spectrum of **Zn dimer** in solution (Figure 3-9). The neutral species displays two ν(C≡N) modes at 2181 cm^{-1} and 2155 cm^{-1}, which

are identical to those found for $TCNQ^-$ in DMF.[33,34] It seems unlikely that a coordinated $TCNQ^-$ would have identical spectra to that for free $TCNQ^-$, and this suggests that the molecule has disproportionated already (Equation 3-2). However, I do observe behavior that differs from just Li(TCNQ) upon addition of reducing equivalents.

$$\textbf{Zn dimer} \leftrightarrow 4\ TCNQ^- + 2\ [Zn(bpym)_2]^{2+} \qquad \text{(Equation 3-2)}$$

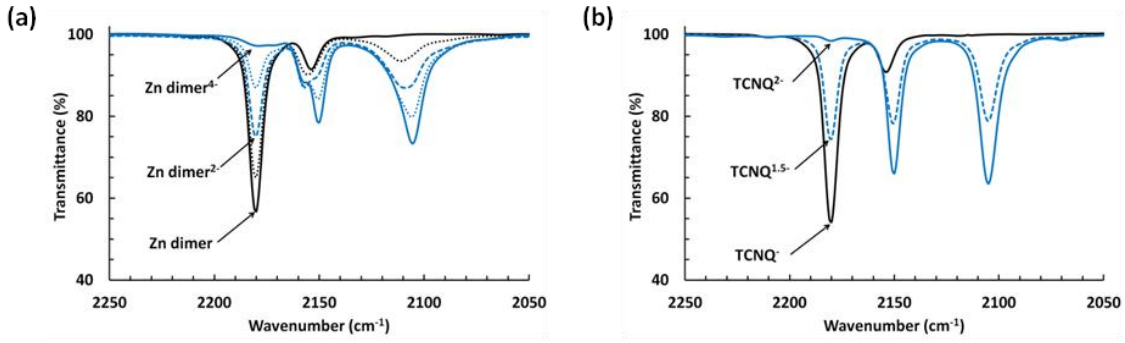

Figure 3-9: (a) ν(C≡N) modes of 2.42 mM **Zn dimer** and its reduced species with oxidation state (-1, -2, -3, and -4) in DMF and (b) ν(C≡N) modes of 2.42 mM Li(TCNQ) and its reduced species with oxidation state (-1.5 and -2) in DMF.

Upon addition of one equivalent of $CoCp_2$ (to give **Zn dimer**$^-$), the band at 2181 cm^{-1} decreases in intensity, the band at 2153 cm^{-1} increases in intensity and undergoes a shift in energy to 2157 cm^{-1}, and a new band appears at 2112 cm^{-1}. The new band is near that found for free $TCNQ^{2-}$ in solution. Addition of another equivalent of $CoCp_2$ (to give **Zn dimer**$^{2-}$) continues this observed trend, though the band at 2153 cm^{-1} becomes split into two distinct bands at 2158 cm^{-1} and 2151 cm^{-1}. Addition of another two equivalents of $CoCp_2$ (passing through **Zn dimer**$^{3-}$ to **Zn dimer**$^{4-}$), results in the loss of the band at 2181 cm^{-1}, an increase in the relative intensity of 2151 cm^{-1} vs. 2158 cm^{-1} and a shift in the low energy band to 2106 cm^{-1}. This shift in energy is also accompanied by a narrowing of this low energy band. The final spectrum of **Zn dimer**$^{4-}$ closely resembles that of $TCNQ^{2-}$, except for the feature at 2158 cm^{-1} and the extra breadth at 2106 cm^{-1}.

Thus, it appears that the feature at 2158 cm^{-1} is diagnostic of **Zn dimer** – or at least not an isolated $TCNQ^{2-}$.

Given this data, I hypothesize as follows. Upon dissolution **Zn dimer** in DMF, the complex disproportionates, yielding four equivalents of isolated $TCNQ^{-}$. Addition of reducing equivalents results in the reduction of $TCNQ^{-}$ to $TCNQ^{2-}$ (Equation 3-3). The dianion is then a stronger ligand for Zn, resulting in re-coordination of the dianion (Equation 3-4). It is this re-association that gives rise to the "extra" feature seen in the spectra in Figure 3-9a, and which I call the **Zn dimer^{2-}**.

$$2\ TCNQ^{-} + 2\ e^{-} \leftrightarrow 2\ TCNQ^{2-} \qquad \text{(Equation 3-3)}$$

$$[Zn(bpym)_2]^{2+} + 2\ TCNQ^{2-} + 2\ TCNQ^{-} \leftrightarrow \textbf{Zn dimer}^{2-} \qquad \text{(Equation 3-4)}$$

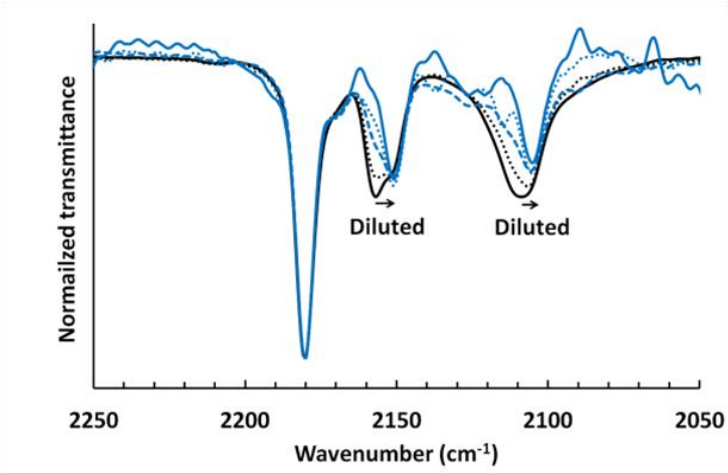

Figure 3-10: ν(C≡N) modes of **Zn dimer^{2-}** with different concentrations in DMF (black solid: 2.42 mM, black dotted: 1.21 mM, blue bold dotted: 0.61 mM, blue dotted: 0.31 mM, and blue solid: 0.16 mM).

It is important to acknowledge that the structure of this new complex could not be characterized, as crystals from the reduced solution did not form. Thus, while it is reasonable to assume re-coordination of the $TCNQ^{2-}$ to the zinc metal center, I do not know if I am reforming **Zn dimer** (unlikely) or some mononuclear zinc complex, $[Zn(bpym)_2(TCNQ^{2-})_x]^{(2-2x)}$. However, the hypothesis of disproportionation is supported by studies into the effect of dilution upon the

spectrum of **Zn dimer**$^{2-}$, which results in a change in the spectrum that is consistent with the increased presence of $TCNQ^-$ and $TCNQ^{2-}$ (Figure 3-10). The favoring of the left side of Equation 3 at high dilution is an expected behavior of the proposed disproportionation.

I can also reconcile the observation that (*i*) there is a feature in the IR unique to **Zn dimer** with (*ii*) the fact that the electrochemistry resembled only Li(TCNQ). I found that chemical reduction of **Zn dimer** in the presence of salt (NaCl or NBu_4PF_6) yielded a spectrum that was identical to that for free $TCNQ^{2-}$. In addition, titration of **Zn dimer**$^{2-}$ solution with salt results in the loss of this extra feature. Thus, I tentatively assign this extra feature at 2158 cm^{-1} to the intact (or partially intact) **Zn dimer**$^{2-}$, which disproportionates to $TCNQ^-$ and $TCNQ^{2-}$ upon the addition of salt (Equation 3-4). I suspect that solutions with high ionic strength are able to stabilize the charge that results from this disproportionation, thus favoring the left side of this reaction.

While I cannot definitively assign the spectral features that are associated with **Zn dimer**, I attempted to find other spectroscopic signals associated with the complex. Normalized UV-vis spectra of diluted **Zn dimer**$^{2-}$ solution as a function of the concentration of **Zn dimer**$^{2-}$ were obtained (Figure 3-11). The absorption band at 330 nm indicates the presence of $TCNQ^{2-}$, and two other strong absorption bands at 420 and 850 nm are attributed to $TCNQ^{\cdot-}$.[35,36] Here I note that the absorption band at 330 nm decreases as the concentration decreases, which corresponds to the IR spectra (Figure 3-10). The decrease in the intensity at 330 nm could support that the unassigned species from **Zn dimer**$^{2-}$ undergoes further disproportionation to $TCNQ^-$ and $TCNQ^{2-}$. In the 300-1000 nm region, I observed no absorption that could not be assigned to $TCNQ^-$ or $[TCNQ\text{-}TCNQ]^{2-}$. Thus, if **Zn dimer** is partially intact, as suggested by the IR data, the electronic absorptions associated with it are too weak to be observed.

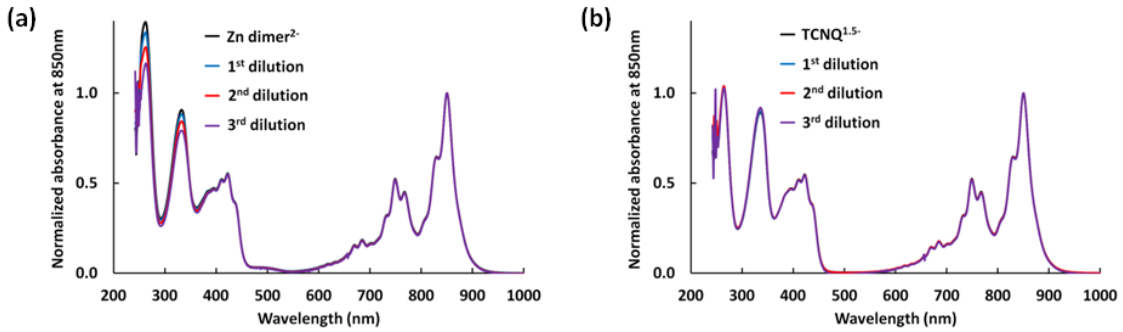

Figure 3-11: UV-vis spectra of (a) **Zn dimer**$^{2-}$ and (b) $TCNQ^{1.5-}$ with different concentrations in DMF (black: 2.42 mM, blue: 1.21 mM, red: 0.61 mM, and purple: 0.31 mM). Normalization was performed by identifying the absorbance at 850 nm for each concentration.

In conclusion, the solution phase behavior of **Zn dimer** strongly suggests that **Zn dimer** is unstable and disproportionates, yielding four equivalents of $TCNQ^-$ in solution. While I do find some small evidence for a species that differs from $TCNQ^-$ in the ν(C≡N) region of the IR, I observe no corresponding unique signals in the UV-vis. Thus, I am unable to discuss the solution-phase behavior of metal coordinated $[TCNQ\text{-}TCNQ]^{2-}$ using this complex.

Conclusions

Mixing of bpym, $TCNQ^-$, and Zn^{2+} yields the first known complex with a metal coordinated $[TCNQ\text{-}TCNQ]^{2-}$. The properties of **Zn dimer** were explored in both the solid and solution phase. However, due to stability problems in solution, I was only able to investigate the properties of **Zn dimer** in the solid state. As a solid I found that the charges of $TCNQ^-$ and $[TCNQ\text{-}TCNQ]^{2-}$ are retained as -1 and -2 respectively. The packing diagram shows that $TCNQ^-$ and $[TCNQ\text{-}TCNQ]^{2-}$ are stacked in a zigzag pattern with each other, resulting in a higher-energy charge transfer in the NIR region. The unpaired electrons from the $TCNQ^-$ ligands gives rise to antiferromagnetic coupling features on **Zn dimer**. Following this first example of a metal-

coordinated $[TCNQ\text{-}TCNQ]^{2-}$, future work can focus on creating a complex that will be more stable in solution.

References

1. Miller, J. S.; Epstein, A. J.; Reiff, W. M. *Chem. Rev.* **1988**, *88*, 201-220.
2. Bryce, M. R. *Chem. Soc. Rev.* **1991**, *20*, 355-390.
3. Dunbar, K. R. *Angew. Chem. Int. Ed.* **1996**, *35*, 1659-1661.
4. Janiak, C. *Dalton Trans.* **2003**, 2781-2804.
5. Shimomura, S.; Kitagawa, S. *J. Mater. Chem.* **2011**, *21*, 5537-5546.
6. Anderson, P. W.; Lee, P. A.; Saitoh, M. *Solid State Commun.* **1973**, *13*, 595-598.
7. Torrance, J. B. *Acc. Chem. Res.* **1979**, *12*, 79-86.
8. Kaim, W.; Moscherosch, M. *Coord. Chem. Rev.* **1994**, *129*, 157-193.
9. Ballester, L.; Gutiérrez, A.; Perpiñán, M. F.; Azcondo, M. T. *Coord. Chem. Rev.* **1999**, *190*, 447-470.
10. Inoue, M.; Inoue, M. B. *J. Chem. Soc., Chem. Commun.* **1984**, 790-791.
11. Grossel, M. C.; Evans, F. A.; Hriljac, J. A.; Morton, J. R.; LePage, Y.; Preston, K. F.; Sutcliffe, L. H.; Williams, A. J. *J. Chem. Soc., Chem. Commun.* **1990**, 439-441.
12. Ballester, L.; Barral, M. C.; Gutiérrez, A.; Jiménez-Aparicio, R.; Martínez-Muyo, J. M.; Perpiñán, M. F.; Monge, M. A.; Ruíz-Valero, C. *J. Chem. Soc., Chem. Commun.* **1991**, 1396-1397.
13. Ballester, L.; Barral, M. C.; Gutiérrez, A.; Monge, A.; Perpiñán, M. F.; Ruíz-Valero, C.; Sánchez-Pélaez, A. E. *Inorg. Chem.* **1994**, *33*, 2142-2146.
14. Azcondo, M. T.; Ballester, L.; Calderón, L.; Gutiérrez, A.; Perpiñán, M. F. *Polyhedron* **1995**, *14*, 2339-2347.
15. Ballester, L.; Gil, A. M.; Gutiérrez, A.; Perpiñán, M. F.; Azcondo, M. T.; Sánchez, A. E.; Coronado, E.; Gómez-García, J. *Inorg. Chem.* **2000**, *39*, 2837-2842.
16. Dong, V.; Endres, H.; Keller, H. J.; Moroni, W.; Nöthe, D. *Acta Crystallogr.* **1977**, *B33*, 2428-2431.
17. Morosin, B.; Plastas, H. J.; Coleman, L. B.; Stewart, J. M. *Acta Crystallogr.* **1978**, *B34*, 540-543.

18. Harms, R. H.; Keller, H. J.; Nöthe, D.; Werner, M.; Gundel, D.; Sixl, H.; Soos, Z. G.; Metzger, R. M. *Mol. Cryst. Liq. Cryst.* **1981**, *65*, 179-196.
19. Hoffmann, S. K.; Corvan, P. J.; Singh, P.; Sethulekshmi, C. N.; Metzger, R. M.; Hatfield, W. E. *J. Am. Chem. Soc.* **1983**, *105*, 4608-4617.
20. Radhakrishnan, T. P.; Van Engen, D.; Soos, Z. G. *Mol. Cryst. Liq. Cryst.* **1987**, *150*, 473-492.
21. Alonso, C.; Ballester, L.; Gutiérrez, A.; Perpiñán, M. F.; Sánchez, A. E.; Azcondo, M. T. *Eur. J. Inorg. Chem.* **2005**, 486-495.
22. Melby, L. R.; Harder, R. J.; Hertler, W. R.; Mahler, W.; Benson, R. E.; Mochel, W. E. *J. Am. Chem. Soc.* **1962**, *84*, 3374-3387.
23. Ballesteros-Rivas, M.; Ota, A.; Reinheimer, E.; Prosvirin, A.; Valdés-Martinez, J.; Dunbar, K. R. *Angew. Chem.* **2011**, *123*, 9877-9881.
24. Kistenmacher, T. J.; Emge, T. J.; Bloch, A. N.; Cowan, D. O. *Acta Crystallogr., Sect. B* **1982**, *38*, 1193-1199.
25. Zhao, H.; Heintz, R. A.; Ouyang, X.; Dunbar, K. R. *Chem. Mater.* **1999**, *11*, 736-746.
26. Zhao, H.; Heintz, R. A.; Dunbar, K. R. *J. Am. Chem. Soc.* **1996**, *118*, 12844-12845.
27. Shimomura, S.; Horike, S.; Matsuda, R.; Kitagawa, S. *J. Am. Chem. Soc.* **2007**, *129*, 10990-10991.
28. Shimomura, S.; Matsuda, R.; Kitagawa, S. *Chem. Mater.* **2010**, *22*, 4129-4131.
29. Boyd, R. H.; Phillips, W. D. *J. Chem. Phys.* **1965**, *43*, 2927-2929.
30. Iida, Y. *Bull. Chem. Soc. Jpn.* **1969**, *42*, 71-75.
31. Kepler, R. G.; Bierstedt, P. E.; Merrifield, R. E. *Phys. Rev. Lett.* **1960**, *5*, 503-504.
32. Le, T. H.; Nafady, A.; Qu, X.; Bond, A. M.; Martin, L. L. *Anal. Chem.* **2012**, *84*, 2343-2350.
33. Khoo, S. B.; Foley, J. F.; Korzeniewski, C.; Pons, S. *J. Electroanal. Chem.* **1987**, *233*, 223-236.
34. Bellec, V.; De Backer, M. G.; Levillain, E.; Sauvage, F. X.; Sombret, B.; Wartelle, C. *Electrochem. Commun.* **2001**, *3*, 483-488.
35. Haller, I.; Kaufman, F. B. *J. Am. Chem. Soc.* **1976**, *98*, 1464-1468.
36. Khatkale, M. S.; Devlin, J. P. *J. Chem. Phys.* **1979**, *70*, 1851-1859.

Appendix for Chapter 3

Magnetic properties measured by SQUID

Magnetic characterization was conducted using a Quantum Design superconducting quantum interference device (SQUID). The temperature dependence was measured in the temperature range of 5-300 K in a measuring field of 50 Oe. Field dependent measurements were measured in a range of -5 T to 5 T at 5 K. The powder samples were mounted in a gel capsule packed with cotton to reduce the background signal. Diamagnetic correction was conducted by subtracting the linear background at saturation taken between the field range of 3 T and 5 T.

Within a single molecule of **Zn dimer** I expected that the two zinc metal centers and $[TCNQ\text{-}TCNQ]^{2-}$ would be diamagnetic. Temperature dependent DC magnetic susceptibility measurements were conducted on separate powder samples of **Zn dimer** and Li(TCNQ). Magnetic susceptibility (χ) and inverse susceptibility (χ^{-1}) with units of emu/mol TCNQ for powders of Li(TCNQ) and **Zn dimer** were plotted in Figure 3A-1.

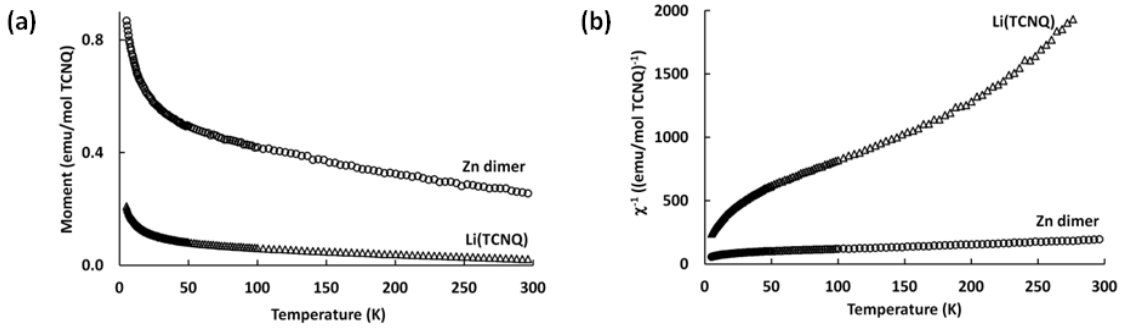

Figure 3A-1: Temperature dependence of magnetism for **Zn dimer** and Li(TCNQ) in (a) magnetic susceptibility (χ) and (b) inverse magnetic susceptibility (χ^{-1}).

Magnetic field sweeps were also conducted in the SQUID (Figure 3A-2). Diamagnetic background was subtracted from the raw signal by subtracting the linear signal of moment saturation near 5 T. The resulting curves show small separation around zero field; however, this is most likely attributed to possible metal impurities within the commercially purchased complexes.

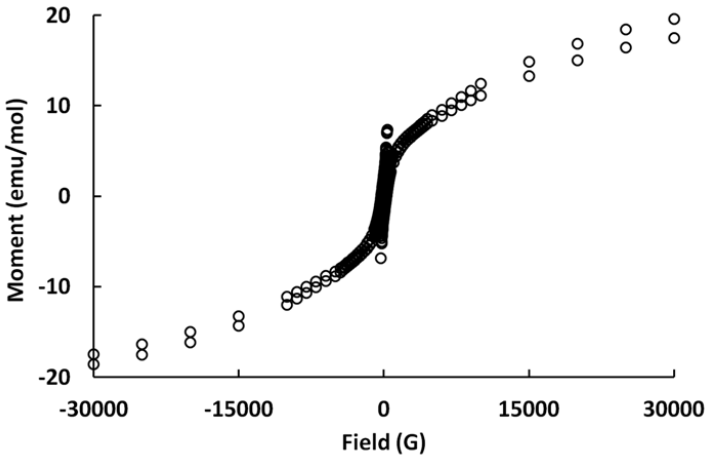

Figure 3A-2: Field dependence sweeps of **Zn dimer** at 5K.

Unfortunately, extracting the Curie constant and spin multiplicity from Figure 3A-1b does not produce reliable variables for **Zn dimer** and even the standard sample, Li(TCNQ). If one attempts to measure SQUID of powder samples which are randomly oriented and polycrystalline, I would recommend collaborating with a magnetochemist who has experience in proper sample preparation and analysis.

Chapter 4

Zinc oxide nanocrystals: Modification of electronic structure by ligand

Introduction

Semiconductor nanocrystals (NCs) are defined as crystallized nanoparticles (1-10 nm in diameter) with a bandgap. For such small systems, the bandgap varies with size, shape, and composition.[1-4] Because of this morphological dependence, the bandgap of NCs can easily be modified to absorb a wide range of light from UV to NIR, allowing a tunability that enhances the utility of the semiconductor systems.[5] When NCs are incorporated in electronic devices, they are usually combined with other nanomaterials that also play important roles in creation and transportation of charge carriers through the device.[6-9] Compared to bulk semiconductors, NCs have larger interfacial area between NCs themselves as well as the other components in the device as a result of the high surface area of NCs. The increase in the interfacial area rises the probability of electron-hole pairs generated from NCs to dissipate or recombine, consequently leading to decline the device efficiency. Thus, it becomes critical to improve interfacial contact between NCs and other components to enhance performance in NC-based optoelectronic devices such as photovoltaics.

In order to minimize energy loss at interfaces, it is important to study the surface electronic structure of NCs as well as how the electronic properties of the interface can be controlled. Because such NCs are often modified by chemical surfactants, a natural question to ask is if these surfactants can be used to control the electronics. Recently, a series of reports by the Weiss group have demonstrated surface ligand-assisted approaches for modifying the surface electronic structure of NCs.[10-13] In their reports, aromatic organic ligands such as

phenyldithiocarbamate were used for stabilizing the surface of CdSe NCs, and they found significant red-shifts in their bandgap absorption.[14] This shift was observed for particles of the same size, demonstrating that the bandgap difference is directly due to the ligands. Also, by using the aromatic organic ligands with different functional groups, they were able to vary the interfacial orbital mixing between the ligands and the NCs.[15,16] From these studies, they concluded that the electron density of NCs could be expanded onto the adsorbed aromatic ligands. This ligand-assisted modification of the electronic structure in NCs has opened a promising path to improve current optoelectronic device efficiency, which can be further utilized for other types of semiconductor NCs.

Beyond CdSe studied exhaustively by the Weiss group, herein I consider ZnO as a good candidate to apply the ligand-assisted modification of the electronic structure of the NCs. Although investigation of the reported system (CdSe-dithiocarbamate) has provided significant insight for electronic interactions between the ligand and the NCs, the studied species is known to be unstable. Thus, it is difficult to learn more information about ligand-involved interfacial interactions with electrons in the conduction band. ZnO NCs, however, are relatively stable for studying electrons in the conduction band. It was reported that upon photoreduction n-type ZnO NCs could retain electrons in the conduction band even for 2 weeks under anaerobic conditions.[17-21] Therefore, by applying the ligand-assisted method to ZnO NCs, one would be able to investigate the ligand effect on the wide bandgap and furthermore examine any influence on electrons in the conduction band directly.

I will discuss preliminary results regarding the synthesis of ZnO NCs and changes in the bandgap energy via ligand modification. Two types of organic ligands (aliphatic and aromatic carboxylic acids) were tested and their effects were investigated via UV-vis spectroscopy (Figure 4-1). It was assumed that the aromatic ligands would have better interaction with ZnO NCs due to

the π-conjugated orbitals. Thus, I expect some degree of change in the band structure and electronic properties of the NCs.

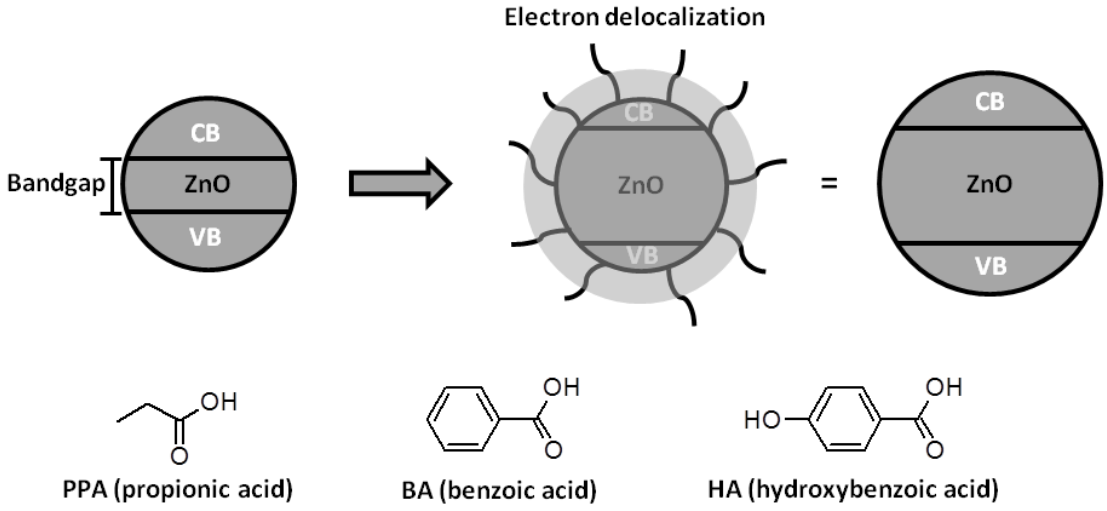

Figure 4-1: Schematic description of electron delocalization in ZnO NCs when modified with ligands and molecular structures that were used in this study.

Experimental

Chemicals and materials

Zinc acetate dihydrate ($Zn(OAc)_2$) [98+%, $Zn(CH_3COO)_2{\cdot}2H_2O$, Strem Chemicals], tetramethylammonium hydroxide pentahydrate (TMAH) [98%, $(CH_3)_4NOH{\cdot}5H_2O$, Alfa Aesar], propionic acid (PPA) [99%, $C_3H_6O_2$, Alfa Aesar], benzoic acid (BA) [99%, $C_7H_6O_2$, Alfa Aesar], and 4-hydroxybenzoic acid (HA) [98%, $C_7H_6O_3$, TCI] were purchased and used without further purification. Pure ethanol with 200 proof was used, and all other solvents were ACS grade.

Characterization

Powder X-ray diffraction (XRD) patterns were collected using a Bruker-AXS D8 Advance diffractometer with Cu K_α radiation and a LynxEye 1-D detector. UV-visible (UV-vis) absorption spectra were measured using an Agilent 8453 spectrometer with a 1 cm path length quartz cell. Infrared (IR) spectra were acquired using a Perkin-Elmer Spectrum 400 FT-IR/FT-NIR spectrometer with an attenuated total reflectance (ATR) crystal. Transmission electron microscopy (TEM) images were obtained from a JEOL 2010 operating at 200 kV.

Synthesis of ZnO NCs and ligand modification

ZnO NCs were prepared using a modified literature protocol.[18] $Zn(OAc)_2$ (0.6650 g, 1.52 mmol) was dissolved in 30 mL of dimethyl sulfoxide (DMSO) in a 100 mL round-bottom flask. TMAH (1.0 g, 5.52 mmol) was dissolved in 10 mL of ethanol in a 20 mL vial. While the $Zn(OAc)_2$ solution was vigorously stirred at 600 rpm, the TMAH solution was added slowly dropwise at 1 mL/min. Afterwards, as-prepared ZnO NCs were precipitated by adding 50 mL of ethyl acetate, which were then separated by centrifugation at 3300 rpm for 10 min. Any remaining liquid was decanted and the white powder (as-prepared ZnO NCs) was washed with ethanol to remove any remaining precursors.

For ligand modification of ZnO NCs, the desired ligand (1.1 mmol) was dissolved in 1 mL of ethanol (83 μL of PPA, 0.1319 g of BA, and 0.1519 g of HA). The as-prepared ZnO NCs from the above procedure could be split into two batches for two different ligand modifications. As-prepared ZnO NCs were redissolved in 24 mL of ethanol, and for each ligand modification half of the solution (12 mL) was transferred in a 50 mL round-bottom flask. The solution was stirred at 600 rpm, and the ligand solution was added dropwise to the ZnO solution until it

became cloudy (approximately 1 mL of PPA, 9 drops of BA, and 2 drops of HA). The ligand-modified ZnO NCs were separated by centrifugation at 3300 rpm for 10 min. After any remaining liquid was decanted, the product was washed with ethanol and dichloromethane. For UV-vis spectroscopy, the product was dissolved in dichloromethane and measured within 10 min immediately after the synthesis. For IR and XRD, the product was dried under vacuum overnight.

Results and Discussion

ZnO NCs were synthesized using the reported method with modification.[18] The synthesis consists of two steps: (*i*) formation of colloidal ZnO NCs and (*ii*) ligand modification process. As-prepared ZnO NCs could be formed by reacting zinc acetate with tetramethylammonium hydroxide through condensation and hydrolysis. They were then precipitated by ethyl acetate. After separated from the solution, as-prepared ZnO NCs were re-dissolved in ethanol and concentrated ligand solution was added to the solution of as-prepared ZnO NCs. Upon the addition of the ligand solution, ligand-modified ZnO NCs were immediately precipitated from ethanol.

In Figure 4-2, there are three peaks at 1575, 1427, and 1349 cm^{-1} shown in the IR spectrum of as-prepared ZnO NCs, which indicates that some amount of acetate ions are present on the surface. After each ligand (PPA, BA, and HA) is adsorbed onto as-prepared ZnO NCs, each ligand-modified ZnO NCs exhibits vibrational modes that correspond to each adsorbed ligand. PPA-ZnO NCs have C-H vibration at 2932 and 2855 cm^{-1}. BA-ZnO NCs show C=O vibration at 1602, 1556, and 1418 cm^{-1}, C=C vibration at 1447 cm^{-1}, and C-H vibration at 717 cm^{-1} that originated from BA.[22] Since all the steps in this synthesis were performed at room temperature, adsorption of carboxylic acids on ZnO NCs seems quite facile.

The XRD patterns of the ligand-modified ZnO NCs are shown in Figure 4-3. As-prepared ZnO NCs exhibit the hexagonal wurtzite structure.[23] Carboxylic acid (PPA, BA, and HA)-modified ZnO NCs retain the same structure with similar full width at half maximum (FWHM), which demonstrates that the ligand incorporation process did not alter the original crystal structure of ZnO NCs.

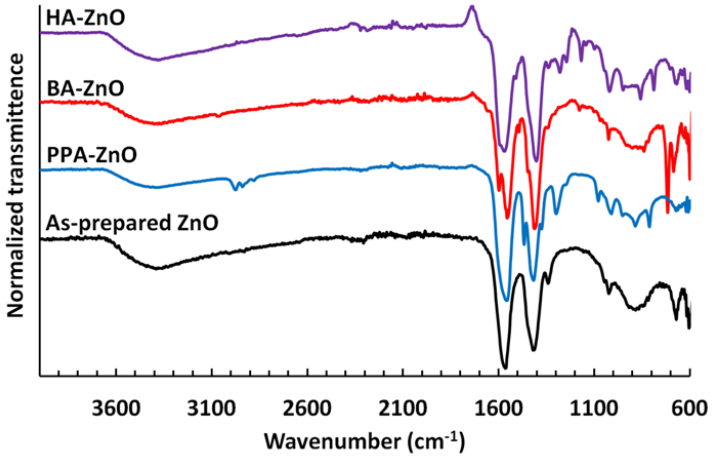

Figure 4-2: IR spectra of as-prepared ZnO (black), PPA-ZnO (blue), BA-ZnO (red), and HA-ZnO (purple) NCs.

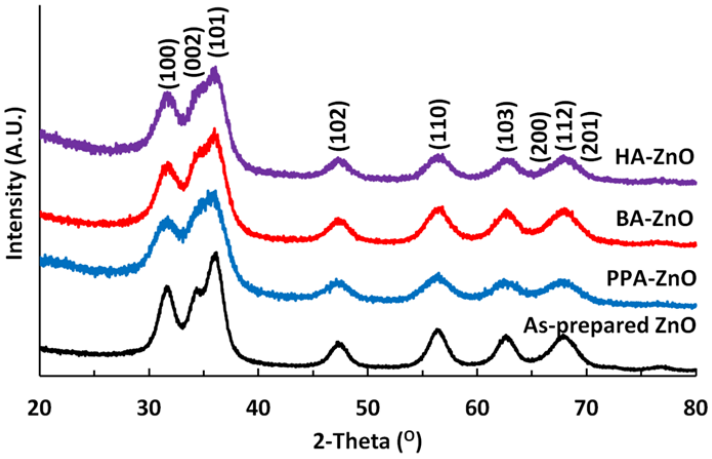

Figure 4-3: XRD patterns of as-prepared ZnO (black), PPA-ZnO (blue), BA-ZnO (red), and HA-ZnO (purple) NCs.

The UV-vis spectra of PPA-, BA-, and HA-ZnO NCs display difference in the bandgap absorption energy (Figure 4-4). Between the linear alkyl ligand (PPA) and the aromatic ligand (BA), BA-ZnO NCs show the absorption at lower energy by 5 nm. The absorption band in HA-ZnO NCs is more red-shifted by 6 nm than that of BA-ZnO NCs. I hypothesize that the π-conjugated HOMO in BA might have better electronic coupling with the surface electronic structure (valence band) of ZnO NCs than PPA, which gave rise to the decrease of the bandgap energy.[24-26] Likewise, further decrease in the bandgap energy could be predicted with the adsorption of HA on ZnO NCs because HA is more electron-donating than BA, which would enrich the electron density of the valence band in ZnO NCs.

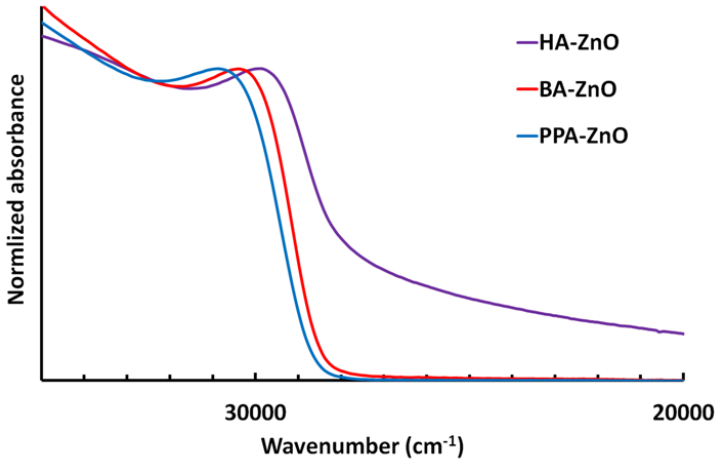

Figure 4-4: UV-vis spectra of PPA-ZnO (blue), BA-ZnO (red), and HA-ZnO (purple) in dichloromethane.

To solidify my hypothesis mentioned above, there are two properties to be evaluated: (*i*) physical size of ZnO NCs and (*ii*) potential optical interference by scattering of suspended particles in UV-vis absorption. It is noted that any change in the physical size affects their bandgap energy, due to quantum confinement.[27,28] Thus, it should be confirmed that there was no deviation of the physical size in PPA-, BA-, and HA-ZnO NCs. A couple of attempts were made to measure the size by TEM, but the poor contrast difference between ZnO NCs and carbon film

on the TEM grid did not help accurately identify the size of the ZnO NCs. By using an empirically-derived formula from literature,[29] one can extract the size of ZnO NCs based on the absorption band (324 nm → 3.08 nm for PPA-ZnO NCs, 329 nm → 3.77 nm for BA-ZnO NCs, and 335 nm → 4.10 nm for HA-ZnO NCs). Since slight increase in the size can give rise to change in the absorption band up to 10 nm, the poor resolution in the TEM images may not allow distinguishing the size difference within 1 nm. Another approach for the size identification was made by using the Scherrer's equation (Equation 4-1) with the XRD patterns.[30] The peak at $2\theta = 47.4^{o}$ was used for θ_B and B. The estimated sizes from XRD and UV-vis data are shown in Table 4-1. There are slight deviations between the estimated values from XRD and UV-vis, but the ascending size from PPA-ZnO NCs to HA-ZnO NCs concurs with XRD and UV-vis.

Table 4-1: Estimated sizes for PPA-ZnO, BA-ZnO, and HA-ZnO by XRD and UV-vis data.

Sample	XRD			UV-vis		
	FWHM	θ_B	Size (nm)	λ_{max} (nm)	$\lambda_{1/2}$ (nm)	Size (nm)
PPA-ZnO	2.40	23.615	3.62	324	340	3.08
BA-ZnO	2.09	23.700	4.15	329	343	3.24
HA-ZnO	2.01	23.695	4.32	335	354	4.10

$$t = \frac{0.9\lambda}{B\cos\theta_B} \qquad \text{(Equation 4-1)}$$

Conclusions

Different ligand-modified ZnO NCs could be synthesized at room temperature to investigate the interfacial interaction between the ligand and the ZnO NCs. Benzoic acid-modified ZnO NCs showed the red-shift in the bandgap absorption energy compared to propionic acid-modified ZnO NCs, which could be attributed to better electronic coupling between the

valence band of ZnO NCs and the π-conjugated HOMO of adsorbed benzoic acid. Further investigation with an electron-donating ligand, hydroxybenzoic acid, was performed to increase the electron density in the valence band. There was more red-shift in the bandgap absorption for hydroxybenzoic acid-modified ZnO NCs. However, this absorption band might also be affected by scattering of un-dissolved particles in solution. In order to verify the interfacial interaction between the ZnO and the aromatic carboxylic acid, it will be necessary to seek an electron-donating or -withdrawing aromatic carboxylic acid that would generate ZnO NCs soluble in non-polar solvents.

References

1. Alivisatos, A. P. *Science* **1996**, *271*, 933-937.
2. Peng, X.; Manna, L.; Yang, W.; Wickham, J.; Scher, E.; Kadavanich, A.; Alivisatos, A. P. *Nature* **2000**, *404*, 59-61.
3. Li, L.; Hu, J.; Yang, W.; Alivisatos, A. P. *Nano Lett.* **2001**, *1*, 349-351.
4. Allen, P. M.; Bawendi, M. G. *J. Am. Chem. Soc.* **2008**, *130*, 9240-9241.
5. Baskoutas, S.; Terzis, A. F. *J. Appl. Phys.* **2006**, *99*, 013708.
6. Leschkies, K. S.; Divakar, R.; Basu, J.; Enache-Pommer, E.; Boercker, J. E.; Carter, C. B.; Kortshagen, U. R.; Norris, D. J.; Aydil, E. S. *Nano Lett.* **2007**, *7*, 1793-1798.
7. Kamat, P. V. *J. Phys. Chem. C* **2008**, *112*, 18737-18753.
8. Pattantyus-Abraham, A. G.; Kramer, I. J.; Barkhouse, A. R.; Wang, X.; Konstantatos, G.; Debnath, R.; Levina, L.; Raabe, I.; Nazeeruddin, M. K.; Grätzel, M.; Sargent, E. H. *ACS Nano* **2010**, *4*, 3374-3380.
9. Thulasi-Varma, C. V.; Gopi, C. V. V. M.; Rao, S. S.; Punnoose, D.; Kim, S.; Kim, H. *J. Phys. Chem. C* **2015**, *119*, 11419-11429.
10. Weiss, E. A. *Acc. Chem. Res.* **2013**, *46*, 2607-2615.
11. Frederick, M. T.; Amin, V. A.; Weiss, E. A. *J. Phys. Chem. Lett.* **2013**, *4*, 634-640.
12. Knowles, K. E.; Peterson, M. D.; McPhail, M. R.; Weiss, E. A. *J. Phys. Chem. C* **2013**, *117*, 10229-10243.

13. Peterson, M. D.; Cass, L. C.; Harris, R. D.; Edme, K.; Sung, K.; Weiss, E. A. *Annu. Rev. Phys. Chem.* **2014**, *65*, 317-339.
14. Frederick, M. T.; Weiss, E. A. *ACS Nano* **2010**, *4*, 3195-3200.
15. Knowles, K. E.; Tice, D. B.; McArthur, E. A.; Solomon, G. C.; Weiss, E. A. *J. Am. Chem. Soc.* **2010**, *132*, 1041-1050.
16. Frederick, M. T.; Amin, V. A.; Swenson, N. K.; Ho, A. Y.; Weiss, E. A. *Nano Lett.* **2013**, *13*, 287-292.
17. Schwartz, D. A.; Gamelin, D. R. *Proc. SPIE-Int. Soc. Opt. Eng.* **2003**, *5224*, 1-7.
18. Schwartz, D. A.; Norberg, N. S.; Nguyen, Q. P.; Parker, J. M.; Gamelin, D. R. *J. Am. Chem. Soc.* **2003**, *125*, 13205-13218.
19. Liu, W. K.; Whitaker, K. M.; Smith, A. L.; Kittilstved, K. R.; Robinson, B. H.; Gamelin, D. R. *Phys. Rev. Lett.* **2007**, *98*, 186804.
20. Whitaker, K. M.; Ochsenbein, S. T.; Polinger, V. Z.; Gamelin, D. R. *J. Phys. Chem. C* **2008**, *112*, 14331-14335.
21. Schimpf, A. M.; Gunthardt, C. E.; Rinehart, J. D.; Mayer, J. M.; Gamelin, D. R. *J. Am. Chem. Soc.* **2013**, *135*, 16569-16577.
22. Lenz, A.; Selegård, L.; Söderlind, F.; Larsson, A.; Holtz, P. O.; Uvdal, K.; Ojamäe, L.; Käll, P. *J. Phys. Chem. C.* **2009**, *113*, 17332-17341.
23. Lin, K.; Cheng, H.; Hsu, H.; Lin, L.; Hsieh, W. *Chem. Phys. Lett.* **2005**, *409*, 208-211.
24. Teklemichael, S. T.; McCluskey, M. D. *J. Phys. Chem. C.* **2012**, *116*, 17248-17251.
25. Saha, S.; Sarkar, S.; Pal, S.; Sarkar, P. *RSC Adv.* **2013**, *3*, 532-539.
26. Saha, S.; Sarkar, P. *RSC Adv.* **2014**, *4*, 1640-1645.
27. Wood, A.; Giersig, M.; Hilgendorff, M.; Vilas-Campos, A.; Liz-Marzán, L. M.; Mulvaney, P. *Aust. J. Chem.* **2003**, *56*, 1051-1057.
28. Reid, P. J.; Fujimoto, B.; Gamelin, D. R. *J. Chem. Educ.* **2014**, *91*, 280-282.
29. Meulenkamp, E. A. *J. Phys. Chem. B* **1998**, *102*, 5566-5572.
30. Cullity, B. D.; Stock, S. R. *Elements of X-Ray Diffraction, 3rd Ed., Prentice-Hall Inc.* **2001**, 167-171.

Appendix A for Chapter 4

Stability of ZnO NCs in solution

During the synthesis (when re-dissolved in solution (ethanol or dichloromethane) after centrifugation of as-prepared ZnO NCs or ligand-modified ZnO NCs) and measurement for UV-vis spectra, I occasionally noticed that the solution of ZnO NCs became a little bit cloudy, which indicated a decrease in the solubility. Thus, I investigated the stability of ZnO NCs in different conditions by comparing their absorption bands (Figure 4A-1).

Immediately after the synthesis was terminated, ligand-modified ZnO NCs were soluble in non-polar solvents such as dichloromethane. After they were fully dried under vacuum, however, I found that the dried ZnO NCs became scarcely soluble in dichloromethane and other non-polar solvents. To measure the UV-vis spectrum of the dried ZnO NCs, I tried to dissolve them in dichloromethane, but the majority of the particles were still suspended in solution. The absorption band of the cloudy solution was red-shifted from 330 nm to 340 nm (Figure 4A-1a), and a broad absorption band grew in low-energy region, which could be caused by scattering of un-dissolved ZnO NCs in solution. Hence, I presume that the ZnO NCs could be aggregated when dried under vacuum and the drying process could cause the dissociation of surface ligands.

Time-dependent stability of OA-, BA-, and PPA-ZnO NCs in dichloromethane (OA = octanoic acid, BA = benzoic acid, and PPA = propionic acid) was also measured via UV-vis spectroscopy (Figure 4A-1b, c, and d). All of the ZnO NCs showed the red-shift in the absorption band by approximately 10 nm after being left in solution for more than 1 day. I presume that those ligand-modified ZnO NCs did not have sufficient stability in dichloromethane over time, which might originate from fragmentation and aggregation of the NCs due to either weak binding between the ligand and the surface or deficient coverage of the ligand on the surface.

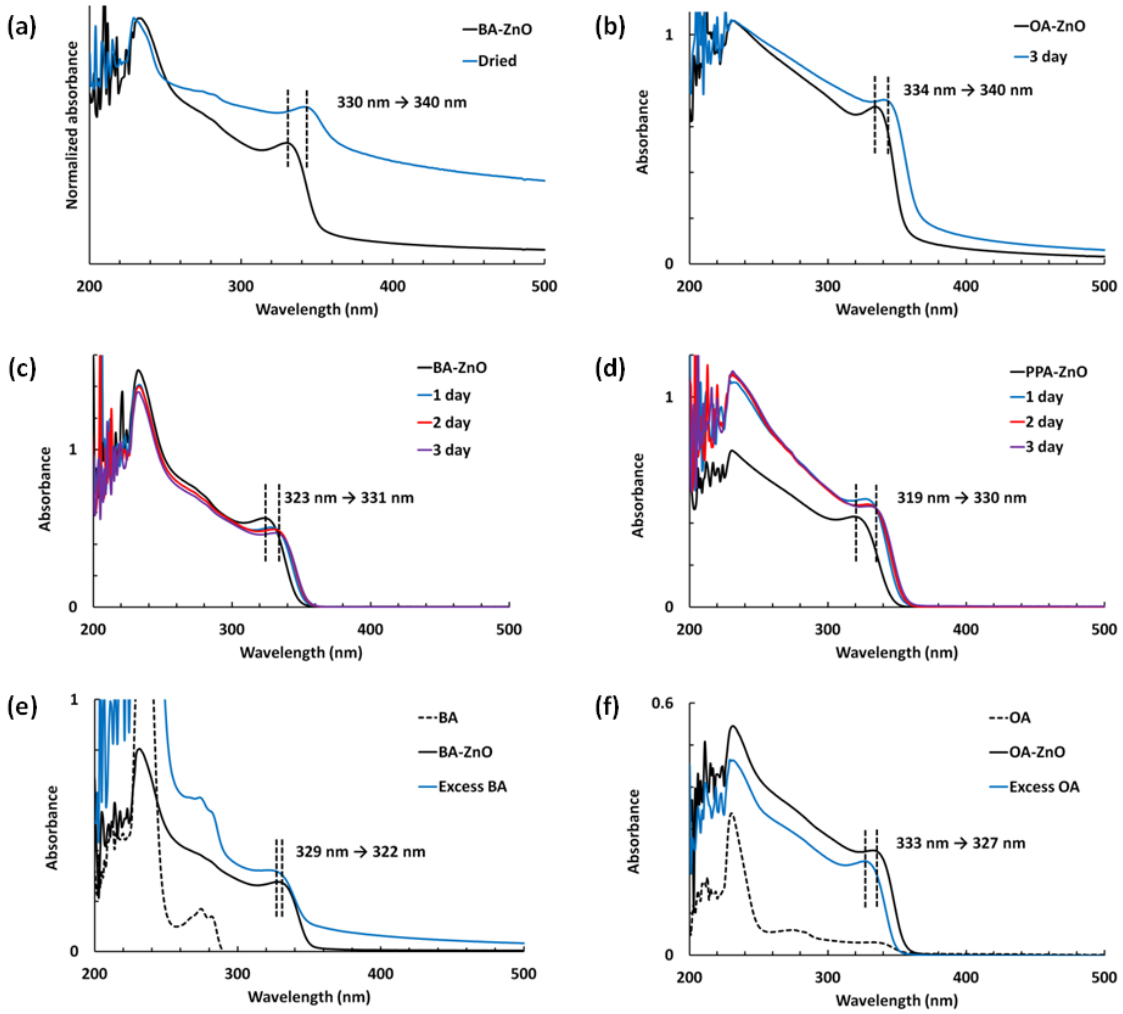

Figure 4A-1: UV-vis spectra of (a) as-prepared BA-ZnO NCs (black) and dried BA-ZnO NCs (blue), (b) as-prepared OA-ZnO NCs (black) and after 3 day in solution (blue), (c) as-prepared BA-ZnO NCs (black) and after 1 (blue), 2 (red), and 3 (purple) day in solution, (d) as-prepared PPA-ZnO NCs (black) and after 1 (blue), 2 (red), and 3 (purple) day in solution, (e) pure BA (dotted), as-prepared BA-ZnO NCs (black), and with excess BA (blue), and (f) pure OA (dotted), as-prepared OA-ZnO NCs (black), and with excess OA (blue). All samples were prepared in dichloromethane.

In order to improve stability of the ligand-modified ZnO NCs in dichloromethane, an excess amount of ligand was added to the solution of the ZnO NCs (Figure 4A-1e and f). However, the addition of each ligand resulted in rather faster precipitation of the ZnO NCs. The

absorption energy in BA-ZnO NCs decreased with the addition of BA, but OA-ZnO NCs showed the red-shifted absorption band with an excess amount of OA. Since pure OA absorbs light from 200 nm to 350 nm, the red-shift in the absorption band may grow in due to the absorption of pure OA, not any interaction between OA and OA-ZnO NCs. On the other hand, the blue-shifted absorption in BA-ZnO NCs likely represents some influence of the excess amount of BA.

Appendix B for Chapter 4

Scattering effect with HA-ZnO NCs

I cannot rule out any optical interference caused by suspended particles for the red-shift in the bandgap absorption energy of HA-ZnO NCs. In the UV-vis spectrum of HA-ZnO NCs, the broad absorption band exists after 32000 cm^{-1}. Contrary to the spectra in PPA- and BA-ZnO NCs, there is a tailing toward low energy present in the spectrum of HA-ZnO NCs. In practice, I observed that the solubility of HA-ZnO NCs was poor in dichloromethane and the solution was turbid when its UV-vis absorption was measured. Some un-dissolved NCs might give rise to light scattering, which could obscure the bandgap absorption energy detected in HA-ZnO NCs. Subsequently, two supplementary experiments were followed to minimize the scattering effect with HA-ZnO NCs.

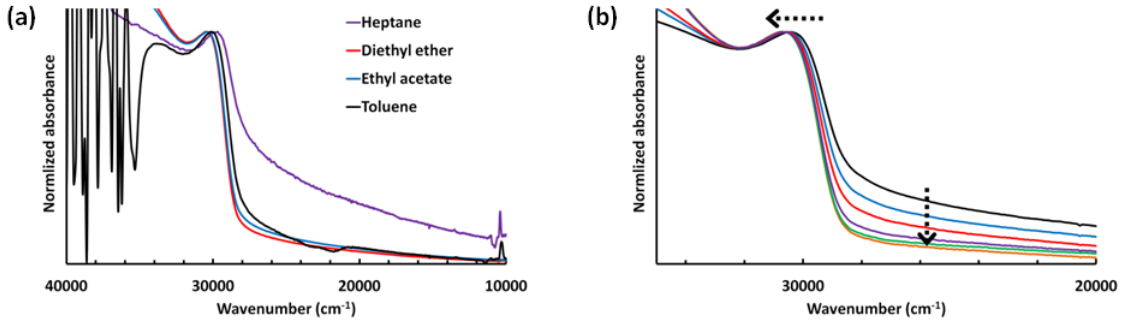

Figure 4A-2: (a) UV-vis spectra of HA-ZnO NCs in toluene (black), ethyl acetate (blue), diethyl ether (red), and heptane (purple) and (b) UV-vis spectra of HA-ZnO NCs in dichloromethane after a series of filtration from initial (black) to final (orange).

First, they were dissolved in different solvents to find a solvent that would dissolve them the most (Figure 4A-2a). By visible inspection, HA-ZnO NCs looked more soluble in diethyl ether and ethyl acetate than toluene and heptane, which clearly reduced the broad absorption band after 32000 cm^{-1}. However, the blue-shift in the bandgap absorption band was observed in diethyl ether and ethyl acetate. Second, repetitive filtrations were performed to eliminate un-dissolved

NCs in solution. Figure 4A-2b shows change in the absorption band of HA-ZnO NCs with repetitive filtrations. As un-dissolved HA-ZnO NCs were removed gradually, the broad absorption band decreased but again the bandgap absorption maxima were blue-shifted. From these two demonstrations, I should admit that the scattering effect could influence the red-shift of the bandgap absorption energy in HA-ZnO NCs, which may not be ascribed to any electronic interaction between ZnO NCs and HA.

Appendix C for Chapter 4

Transformation of ZnO NCs to crystalline sheets

I would like to now discuss interesting findings during the synthesis of ZnO NCs and it will still need further investigation to identify the product and understand the transformation mechanism. During the ligand incorporation step in the synthesis, it was found that OA-ZnO NCs became insoluble in any other solvents after the addition of an excess amount of OA.

As-prepared ZnO NCs were first prepared by the above synthesis at half-scale. In the ligand incorporation, once precipitation occurred with the addition of OA solution, dichloromethane was added to the cloudy solution in order to re-dissolve the precipitates. This step was repeated six times until precipitation did not occur in dichloromethane even with the addition of an excess amount of the OA solution. Then, pure OA was added to the solution until any precipitation of ZnO species was observed, but the final precipitates could not be re-dissolved in dichloromethane anymore (Table 4A-1). The product was separated by centrifugation at 3300 rpm for 10 min and washed with ethanol. No common solvent was found that would dissolve the produce. Likewise, the production of insoluble solid from ZnO NCs could be obtained with the addition of HA, but not PPA nor BA. The insoluble solid with HA, however, was not as crystalline as that with OA based on the XRD patterns.

Table 4A-1: Volume of OA solution and dichloromethane added during the synthesis.

Iteration	OA solution (drop)	Dichloromethane (mL)
1	18	6
2	6	4
3	5	4
4	6	3
5	8	3
6	63 and pure OA 29 drops	not dissolved

The XRD pattern of the insoluble product (OA-ZnO-P) looks completely different from that of OA-ZnO NCs, but showing sharp peaks at 2θ = 8.5, 12.8, and 17.0° with high-intensity (Figure 4A-3a). The IR spectrum of OA-ZnO-P clearly contain C-H vibration at 2923 and 2854 cm^{-1} and C=O vibration at 1526 and 1456 cm^{-1}, which proves that OA is still present in the product (Figure 4A-3b).

The SEM images show that the product is plate-like and the size of individual plates ranges in ~50 μm, and also the SEM EDS mapping identifies the presence of Zn (Figure 4A-4). Thus, I presume that the product is composed of both of OA and Zn. OA-ZnO-P is not thermally stable beyond 200 °C and loses all organic species before 360 °C (Figure 4A-5a). In addition, the N_2 isotherm shows that OA-ZnO-P is a non-porous crystalline solid (Figure 4A-5b).

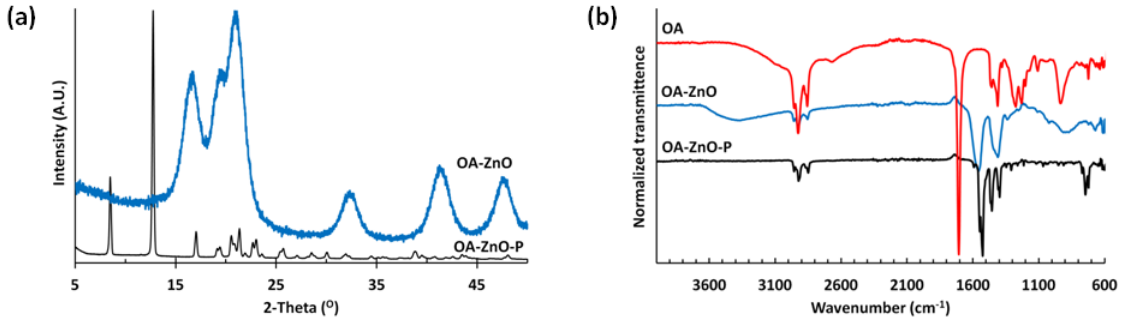

Figure 4A-3: (a) XRD pattern of OA-ZnO-P (black) and OA-ZnO NCs (blue) and (b) IR spectra of OA-ZnO-P (black), OA-ZnO NCs (blue), and pure OA (red).

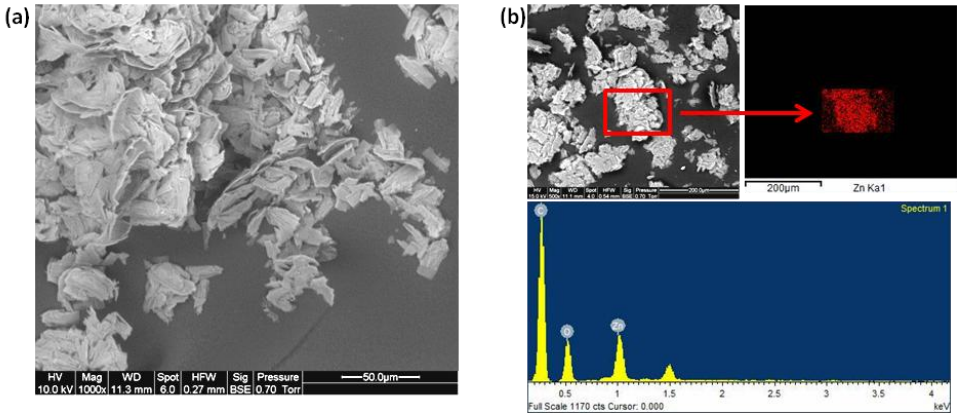

Figure 4A-4: (a) SEM image and (b) SEM EDS mapping of OA-ZnO-P.

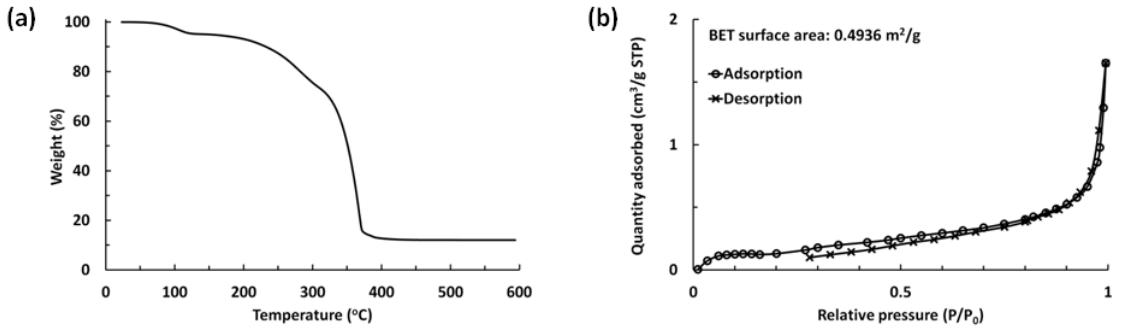

Figure 4A-5: (a) TGA and (b) BET analysis of OA-ZnO-P.

Chapter 5

Coumarin 153 in MOF-5: Photophysical properties in confined environment

Introduction

The physical confinement of molecules can change their behavior.[1-9] For instance, confinement creates new interactions between the confined molecule and the confining medium, as well as a reduction of the interaction between neighboring molecules. Both of these effects give rise to behavior of molecules that is different than when they are freely present. Such confined molecular interactions play a role in both homogeneous and heterogeneous interactions, and contribute to catalysis. One set of compounds for which confinement is important are metal-organic frameworks (MOFs), organic-inorganic hybrid materials with order micropores.[10] Various molecules can be confined inside the pore in MOFs, and the confined molecular interactions result in an enhanced capacity for gas absorption and high efficiency for liquid separation and purification in MOFs.[11-13] In addition, certain classes of MOFs catalyze chemical reactions with high yields.[14,15] Thus, an understanding of confined molecular behavior in MOFs would be helpful for elucidating mechanisms on physical adsorption of molecules and chemical reactions occurring inside MOFs, and further guiding how to select types of MOFs and guest molecules for enhanced performance as well as how to design MOFs for specific applications.

MOFs provide a diverse molecule-scale environment for investigating confined molecular interactions. Since they are formed through periodic linkages of organic ligands and metal clusters, one can design and synthesize a number of MOF structures.[16-20] There are also many techniques developed for modifying functional groups and morphology of already synthesized MOFs, which extends the range possible MOFs.[21-23] Therefore, these facile structural

and chemical modification methods for MOFs allow one to fine-control a particular parameter of confined environment such as polarity and internal space. In order to fully understand how to design such environments, it becomes necessary to understand the effect of confinement on molecular behavior.

The behavior of molecules confined in MOFs has been studied mostly via molecular dynamics simulations, which gives an understanding of their diffusivity and preferred positions inside the pore.[24-26] Amirjalayer et al. reported the liquid diffusivity of benzene molecules in MOF-5,[24] which is a prototypical MOF. It is composed of terephthalate as an organic linker and Zn_4O unit as a metal node, which yields an overall cubic structure.[27] His simulation shows that benzene molecules diffuse slower inside MOF-5 than in bulk solvent due to lattice dynamics of the flexible framework and the molecules preferentially reside at the pocket sites near Zn_4O units. Ford et al. further studied self-diffusion of various *n*-alkanes in MOF-5 and demonstrated that molecular dynamics simulations are in accord with experimental results: the diffusion rates of hydrocarbons are similar to those in bulk solvent but an order of magnitude quicker than those in zeolites.[26] These studies contribute to understanding binary interactions between guest molecules themselves or a guest molecule and the framework.

The above focused on interaction of pure behavior with MOF-5. In most applications, there are more than one type of guest molecule involved in chemical reaction or physical adsorption events inside MOFs, producing more complex molecular interactions than are present in systems with a single type of guest molecule. It is necessary to develop a model system in order to comprehend the multiple molecular interactions within the pore. One can create such system by confining a solvatochromic dye molecule in MOFs, and investigation of its spectral response to different solvent molecules will help understand confined molecular interactions. Inclusion of solvent molecules in the pore would create secondary local environment to be

considered apart from a primary host-guest interaction between the framework and the solvatochromic molecule.

Below, I discuss solvent-dependent photophysical properties of coumarin 153 (C153) confined in MOF-5 (Figure 5-1) in comparison with the properties of C153 with different solvents in bulk condition. C153 and MOF-5 are well-suited to this study of confined molecular behavior under control of solvent polarity in that MOF-5 is known to be compatible with various solvent molecules,[28-30] and C153 is also soluble in a wide range of solvents from nonpolar to polar and shows strong solvatochromism in both the absorption and emission spectra.[31-32]

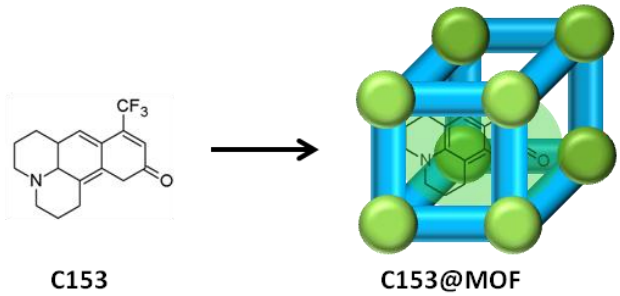

Figure 5-1: C153 confined in MOF-5 (C153@MOF).

I will focus on UV-visible absorption and fluorescence emission spectra of C153 and C153@MOF with different solvents and specifically examine change in the absorption and emission band energy and shape with respect to solvent polarity (Figure 5-2). The absorption and emission band position of C153 is known to decrease in energy as the polarity of the environment increases, which is attributed to stabilization of the excited state of C153. In addition, the vibronic features of C153 spectra become more resolved in nonpolar solvents. Thus, analyzing the energy and shape of the spectra will help understand how confined space affects the ground and excited state energy levels of C153, and from the emission process of C153 one can infer how much confined molecular interactions such as a host-guest interaction are associated with the energetics of C153. Furthermore, Stokes shift will provide information for solvent reorganization energy in the confined space.

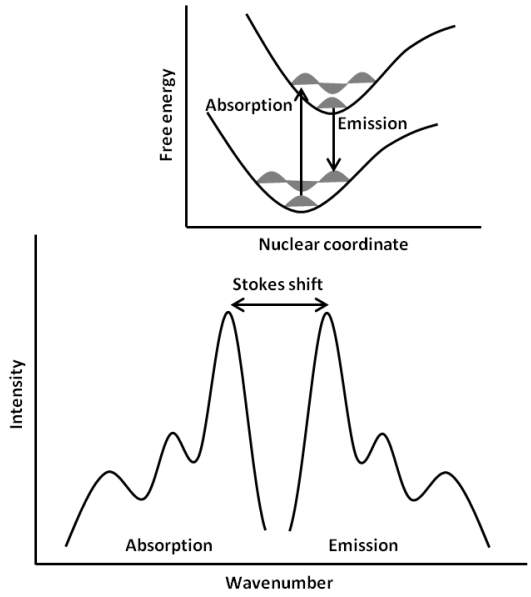

Figure 5-2: Spectral illustrations of absorption, emission, and Stokes shift with corresponding potential energy surfaces of the ground and excited states.

I hypothesize that the confined environment in MOF-5 would diminish solvent reorganization energy due to a reduced amount of solvent molecules present in the pore, and it also creates an additional interaction with the framework. Specifically, I suppose that lattice dynamics of MOF-5 would contribute to change in the energetics of C153.

Experimental

Materials and methods

Zinc nitrate hexahydrate [98%, $Zn(NO_3)_2 \cdot 6H_2O$, Strem Chemicals], terephthalic acid [98+%, $C_8H_6O_4$, Alfa Aesar], and C153 [99%, $C_{16}H_{14}F_3NO_2$, Aldrich] were purchased and used without further purification. All solvents were ACS grade. Beside *N*,*N*-dimethylformamide and chloroform used for synthesis, all solvents were dried and used for spectroscopic measurements.

Also, because MOF-5 is susceptible to water, sample preparation for spectroscopic measurements was performed cautiously to minimize sample exposure to water.

Powder X-ray diffraction (XRD) patterns were collected using a Bruker-AXS D8 Advance diffractometer with Cu K_α radiation and a LynxEye 1-D detector. Absorption spectra were measured for 0.2 g of each solid sample mixed with 0.1 g KBr using a Perkin-Elmer Lambda 950 UV-Vis-NIR spectrophotometer, and regular liquid-phase absorption spectra were measured using an Agilent 8453 spectrometer with a 1 cm path length quartz cell. Emission spectra were measured using a Spex 212 Fluorolog fluorometer with a NMR tube. ^{1}H NMR spectra were recorded with C_2D_6OS by a Bruker CDPX-300 spectrometer. Confocal fluorescence images were obtained using a LSM-5 Pascal Laser confocal microscope (Carl Zeiss, Inc.).

Synthesis of MOF-5

$Zn(NO_3)_2 \cdot 6H_2O$ (2.52 g, 8.45 mmol) and terephthalic acid (0.477 g, 2.87 mmol) were added to an 100 mL flask with 50 mL of argon-purged *N*,*N*-dimethylformamide.[33] The solution was stirred at 600 rpm and refluxed at 120 ^oC for 16 h under argon without light. It was cooled to room temperature, and the solution was decanted carefully. The white precipitates were soaked in 20 mL of *N*,*N*-dimethylformamide, followed by decanting the solvent carefully, which was repeated 9 times to remove unreacted precursors. Then, the white precipitates were soaked in 20 mL of chloroform and the above decanting process was repeated 6 times. The product was stored in 20 mL of chloroform for 1 day, and after the solvent removal it was dried under vacuum for 1 day.

Synthesis of C153@MOF and preparation for spectroscopic measurements

C153 (0.0062 g, 0.0200 mmol) was dissolved in 20 mL of dry methanol. MOF-5 (0.05 g) was added to a 20 mL vial, followed by adding 2 mL of the C153 solution. The vial was stored in the dark for 1 day. Afterwards, the green solution was decanted and 2 mL of chloroform was added to the vial for rinsing any remaining C153 solution. This washing and decanting process was repeated 5 times. To remove methanol molecules remaining inside the MOF, the vial was filled with 5 mL of chloroform and stored in the dark for 1 day. Chloroform was decanted and rinsed with the solvent that would be tested for spectroscopic measurements. It was decanted and 5 mL of fresh solvent was added to the vial. Then, it was stored in the dark for 1 day before measurements. For diffuse reflectance UV-vis absorption spectra, all materials used in the procedure were doubled in amount.

Results

Encapsulation of C153 with MOF-5

C153 could be encapsulated inside MOF-5 by simply soaking the MOF in concentrated C153 solution. The size of C153 (4 Å) can allow the molecule to be diffused into preformed MOF-5 (15 Å pore size and 7.5 Å pore opening).[27] Based on the size difference, I also presume that solvent molecules can reside inside the pore.

Encapsulation of C153 in MOF-5 was confirmed by the absorption band observed with C153@MOF that corresponds to the electronic transition of C153 (λ_{max}: 419 nm for C153 in acetonitrile),[32] and the fluorescence emission image demonstrated the presence of C153 and the homogeneous distribution of the molecules over the MOF particles (Figure 5-3). If the molecule

was trapped at surface or only diffused a small way into the MOF, the edges would be much brighter than the middle in the fluorescence image. The XRD pattern of C153@MOF is similar to that of pure MOF-5 (Figure 5-4), indicating that the crystal structure of MOF-5 was not altered by encapsulation of C153.

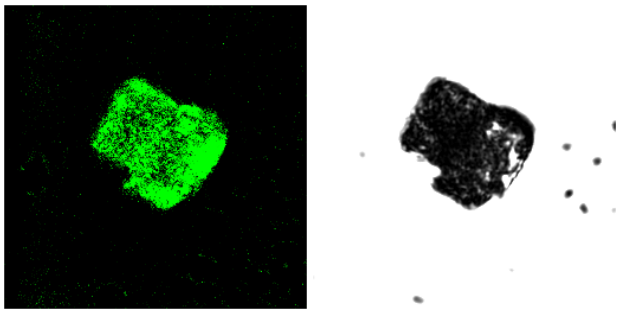

Figure 5-3: Fluorescence emission (left) and transmitted (right) images of C153@MOF with excitation at 400 nm.

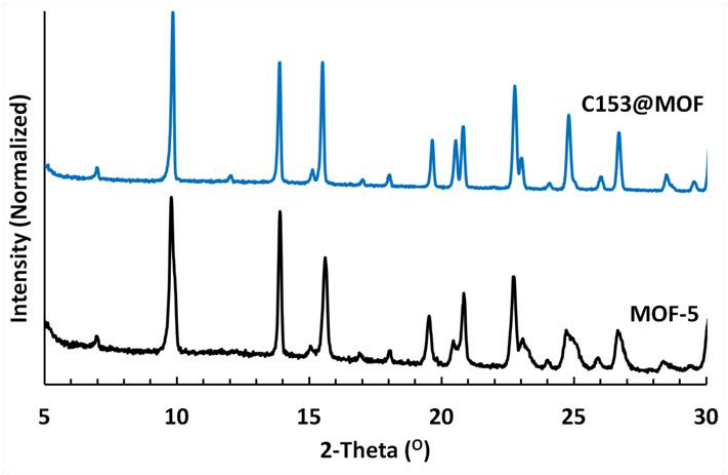

Figure 5-4: X-ray diffraction patterns of MOF-5 (black) and C153@MOF (blue).

Absorption spectra of C153 and C153@MOF in different solvents

The absorption spectra of C153@MOF in five different solvents (hexane, chloroform, acetonitrile = MeCN, dichloromethane = DCM, and *N*,*N*-dimethylformamide = DMF) were measured by diffuse reflectance UV-vis spectroscopy and compared with those of C153 that were

collected by regular UV-vis spectroscopy in the solution phase (Figure 5-5 and 5-6). Polarity of these five solvents ranges from -0.08 (hexane) to 0.88 (DMF).[34]

Due to two different spectroscopic techniques used for solution (C153) and solid (C153@MOF) samples, it is difficult to directly compare the absorption band widths in the spectra measured via diffuse reflectance spectroscopy when compared with those obtained by regular UV-vis spectroscopy. Also, it should be noted that the background reflectance signals fluctuate from sample to sample in diffuse reflectance spectroscopy, although the absorption band positions and shapes of the spectra did not deviate much as a result. However, the different background reflectance signals can change in the absorption band widths. Thus, the widths may not accurately reflect the photophysical properties of C153@MOF.

As reported in literature,[31] the absorption spectra of C153 show the red-shift in the absorption band position with increased polarity (Figure 5-5a). The absorption band positions with hexane (25532 cm^{-1}), chloroform (23866 cm^{-1}), MeCN (23885 cm^{-1}), DCM (23753 cm^{-1}), and DMF (23613 cm^{-1}) are dependent upon solvent polarity. The spectrum of C153 in hexane displays distinct vibronic features located in higher energy compared to the spectra with the other four polar solvents whose absorption band shapes are broadly asymmetric and featureless. Solid C153 has the absorption band at the lowest energy (23462 cm^{-1}) with the asymmetric gaussian shape.

Figure 5-5b presents the absorption spectra of C153@MOF in different solvents. There are two absorption events displayed within the plotted wavenumber range (28000-20000 cm^{-1}). The rise from approximately 25500 cm^{-1} to higher wavenumbers accounts for the absorption by terephthalate in MOF-5 and the lower-energy absorption band corresponds to the electronic transition of C153 confined in MOF-5.[35] The absorption band positions of C153@MOF (22989 cm^{-1} for hexane, 22884 cm^{-1} for chloroform, 23166 cm^{-1} for MeCN, 23274 cm^{-1} for DCM, and 22762 cm^{-1} for DMF) are more red-shifted than C153 measured in the same solvents. Specially,

the absorption band of solid C153@MOF is located at 23772 cm^{-1}, which is lower in energy by 310 cm^{-1} than solid C153. The absorption band position of solid C153@MOF, however, is at higher energy than C153@MOF with solvent molecules, whereas that of solid C153 is positioned at lower energy than C153 with solvent molecules. After confined in MOF-5, the absorption band of C153 lacks well-resolved vibronic features in all solvents, though a discernible shoulder is present in most solvents.

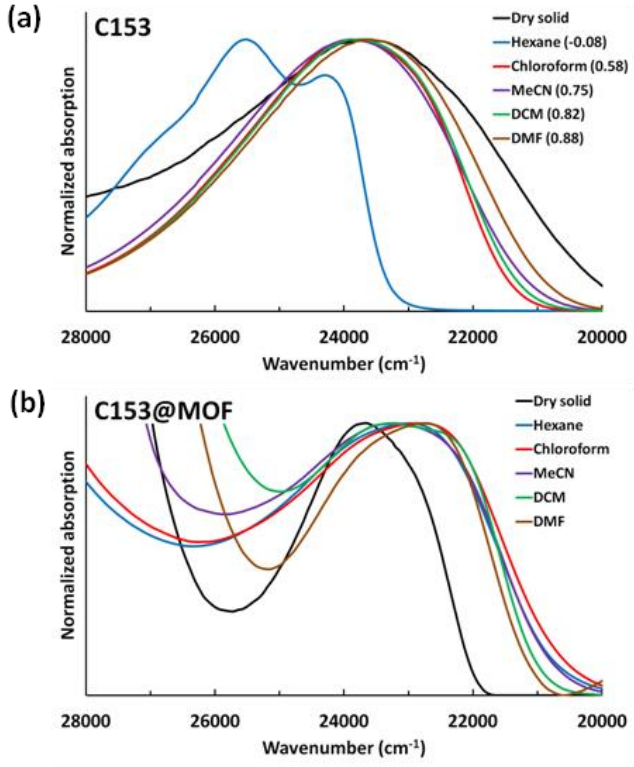

Figure 5-5: Normalized UV-vis absorption spectra of (a) C153 and (b) C153@MOF in different solvents. The spectra of C153 in solution were measured via a regular UV-vis absorption spectrometer. The spectra of solid C153 and C153@MOF in solution were measured via a UV-vis-NIR diffuse reflectance spectrometer and the original reflectance signal was converted by the Kubelka-Munk theory and normalized. Polarity index is shown in parenthesis.

Overlaid absorption spectra of C153 and C153@MOF are plotted in Figure 5-5. Without solvent molecules (Figure 5-6a), the absorption band position of C153 does not show any large difference (blue-shifted only by 310 cm^{-1}) after confined in MOF-5, whereas the absorption band

positions of C153@MOF with solvent molecules are all red-shifted by larger energy difference (2543 cm^{-1} for hexane, 982 cm^{-1} for chloroform, 719 cm^{-1} for MeCN, 479 cm^{-1} for DCM, and 851 cm^{-1} for DMF) from those of C153.

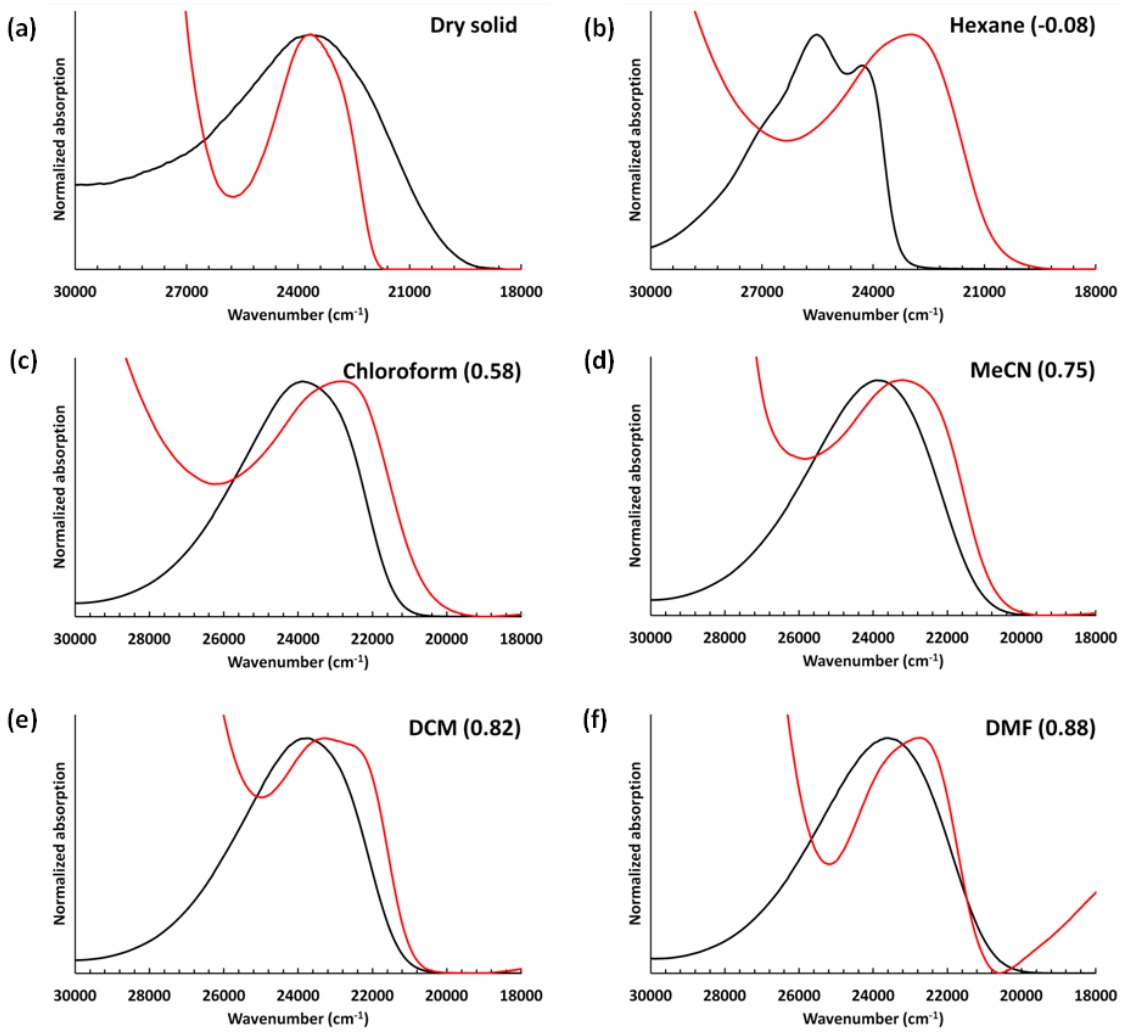

Figure 5-6: Individual absorption spectra of C153 (black) and C153@MOF (red) in each solvent. Polarity index is shown in parenthesis.

The absorption band shapes of C153 in some of the solvents are changed after encapsulated in MOF-5, which can be recognized by the vibronic features. In hexane (Figure 5-6b), the vibronic features of C153 at 27027 cm^{-1}, 25510 cm^{-1}, and 24272 cm^{-1} become less distinct for C153@MOF. In the other four solvents, however, the vibronic features of C153

emerge slightly when confined in MOF-5. Except MeCN, a should peak can be identified next to the absorption band maximum.

Emission spectra of C153 and C153@MOF in different solvents

Fluorescence emission spectra of C153 and C153@MOF are displayed in Figure 5-7 and 5-8. Both solution and solid samples could be measured using the same fluorometer. The quantum yield of C153@MOF will not be discussed because heterogeneous distribution of the particles resulted in variation of the emission intensity even with the same batch of C153@MOF. The emission band position and shape of C153@MOF in different solvents was reproducible. There is a shoulder peak observed at higher energy in the emission spectra of C153@MOF, which might originate from the emission by terephthalate in MOF-5 as a result of vibronic features.[36,37]

Analogous to the solvent-dependent shift in the absorption band position of C153 without MOF-5, the emission band position of C153 (22222 cm^{-1} for hexane, 20325 cm^{-1} for chloroform, 19268 cm^{-1} for MeCN, 19987 cm^{-1} for DCM, and 19121 cm^{-1} for DMF) decreases as solvent polarity increases (Figure 5-7a). The emission band positions of C153 in the four polar solvents are rather closely located to each other at lower wavenumbers than that for hexane. In those four solvents, solvent dependency in the emission spectra stands out compared to that in the absorption spectra in that energy difference in the emission (~1204 cm^{-1}) is five-fold larger than that in the absorption (253 cm^{-1}).

In hexane, C153 shows the vibronic features at 23256 cm^{-1}, 22124 cm^{-1}, and 20790 cm^{-1} which are of similar symmetry and spacing to those detected in the corresponding absorption spectrum. Also, the emission spectra with the other solvents are symmetric to the corresponding absorption spectra: they do not retain the vibronic features, and their band shapes are asymmetric-

gaussian. The emission band of solid C153 appears Lorentzian and much narrower (1467 cm^{-1} in FWHM) than C153 with solvent molecules (2973-3196 cm^{-1} in FWHM).

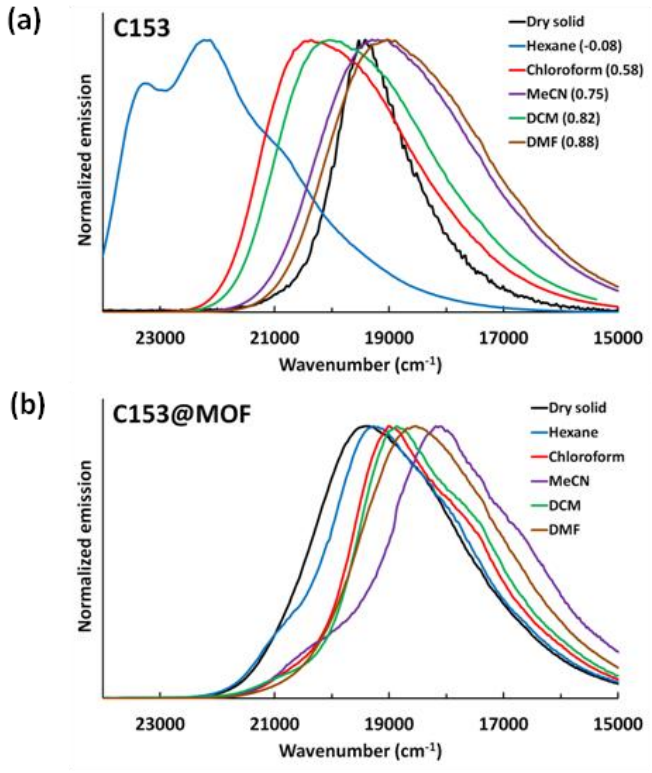

Figure 5-7: Normalized fluorescence emission spectra of (a) C153 and (b) C153@MOF in different solvents. Polarity index is shown in parenthesis.

The emission spectra of C153@MOF in different solvents are shown in Figure 5-7b. In the presence of solvent molecules, the emission band energy of C153@MOF are red-shifted with respect to that of C153. Increase in the solvent polarity leads to decrease in the emission band position of C153 confined in MOF-5 (19343 cm^{-1} for hexane, 18999 cm^{-1} for chloroform, 18094 cm^{-1} for MeCN, 18832 cm^{-1} for DCM, and 18507 cm^{-1} for DMF), but this trend is not absolute for the three most polar solvents (MeCN, DCM, and DMF). C153@MOF in MeCN ($\pi^* = 0.75$) has the lowest energy emission band than in DCM ($\pi^* = 0.82$) and DMF ($\pi^* = 0.88$).

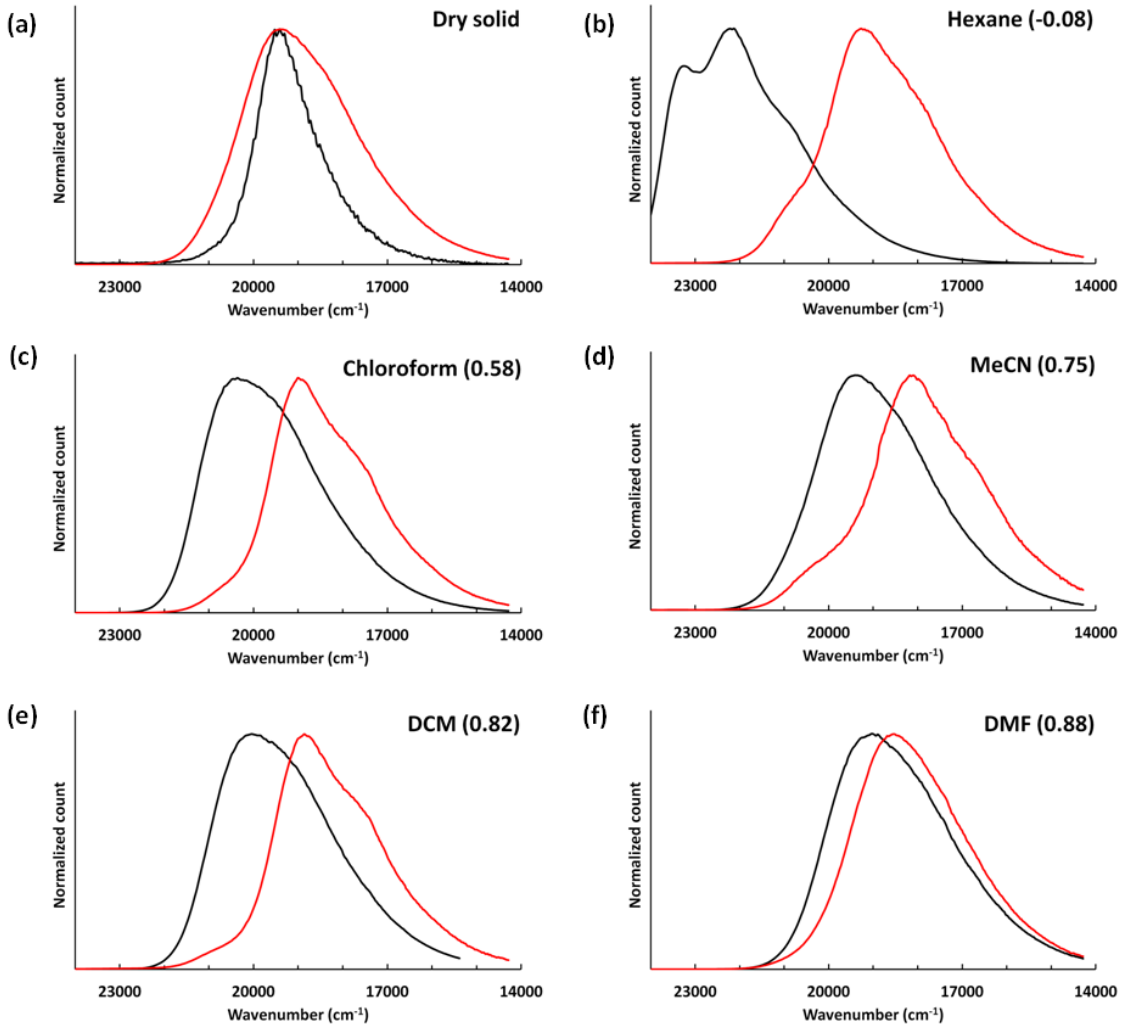

Figure 5-8: Individual fluorescence emission spectra of C153 (black) and C153@MOF (red) in each solvent. Polarity index is shown in parenthesis.

Overlaid emission spectra of C153 and C153@MOF in the same solvent are presented in Figure 5-8. The distinct vibronic features observed with C153 in hexane become obscured for C153@MOF in hexane, while the emission spectra of C153@MOF in the other solvents show re-occurrence of the vibronic features with the asymmetric gaussian shape. In addition, after confined in MOF-5, the emission band widths of C153 become narrower by approximately 400 cm^{-1} in FWHM than those without MOF-5. Solid C153@MOF, however, shows broadening of the emission band width.

Discussion

Solvatochromism

In order to help quantify their relative solvatochromism, the absorption band maxima of C153 and C153@MOF in different solvents are plotted with respect to solvent polarity in Figure 5-9a. There is a good linear correlation between the absorption band energy and the solvent polarity. It is known that the dipole moment of C153 changes from 5.6 D in the ground state (S_0) to 10 D in the excited state (S_1).[31] With the increased dipole moment, the S_1 state of C153 can be more stabilized with polar solvent molecules than the S_0 state, which is demonstrated by the lowest absorption band energy observed for C153 in DMF ($\pi^* = 0.88$). There is no linear dependence of the absorption band energy of C153@MOF and the solvent polarity. That is the absorption of C153@MOF appears to be solvent-independent. Together, these two trends yield interesting to find that a linear dependence of the energy difference between C153 and C153@MOF for the absorption band (Figure 5-9b).

In addition, the emission spectra of C153 and C153@MOF show a similar relationship observed for the absorption spectra. Figure 5-10a shows relationships between the emission band energy and the solvent polarity for C153 and C153@MOF. It is clear to observe that the emission band energy of C153 decreases as solvent polarity increases, and again C153@MOF shows a much weaker solvatochromic response than does C153. Once more, the difference in energy between C153 and C153@MOF is linear (Figure 5-10b).

There are two possible explanation for the weaker solvatochromism of C153 in MOF-5 (Figure 5-9a and 5-10a). First, the framework may affect and interact so strongly with C153 that it dominates the change in the S_0 or S_1 states and even in the presence of solvent molecules. Second, the framework may exclude solvent molecules, reducing the degree of solvation and by

way of this, the solvatochromism. Considering the fact that the smallest energy difference between absorption and emission spectra for C153 and C153@MOF occurs in the absence of solvent molecules (Figure 5-6a and 5-8a). This suggests that it may be the exclusion of solvent molecules that dominates the effect of the framework.

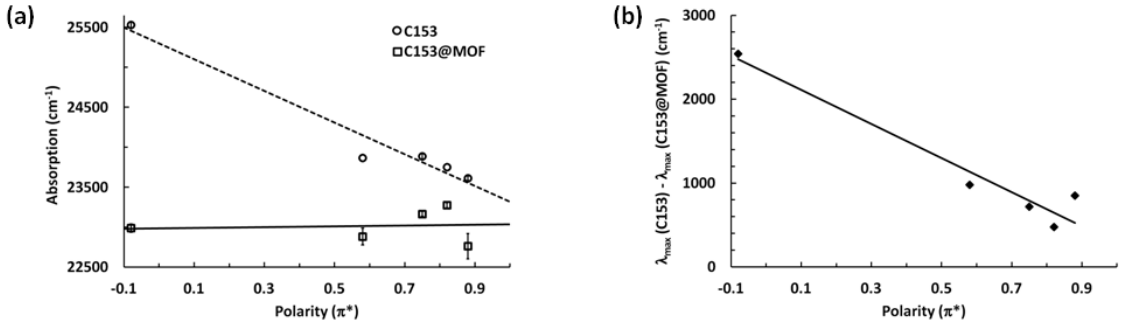

Figure 5-9: (a) Absorption maxima of C153 (circle) and C153@MOF (square) as a function of solvent polarity (π*) and (b) energy difference between C153 and C153@MOF as a function of solvent polarity (π*). Equations for the best-fit lines are y = -1982x + 25299, R^2 = 0.9597 for C153 (dotted) in (a), y = 48.092x + 22987, R^2 = 0.0082 for C153@MOF (solid) in (b), and y = -2030.1x + 2312.6, R^2 = 0.9378 for the energy difference in (b).

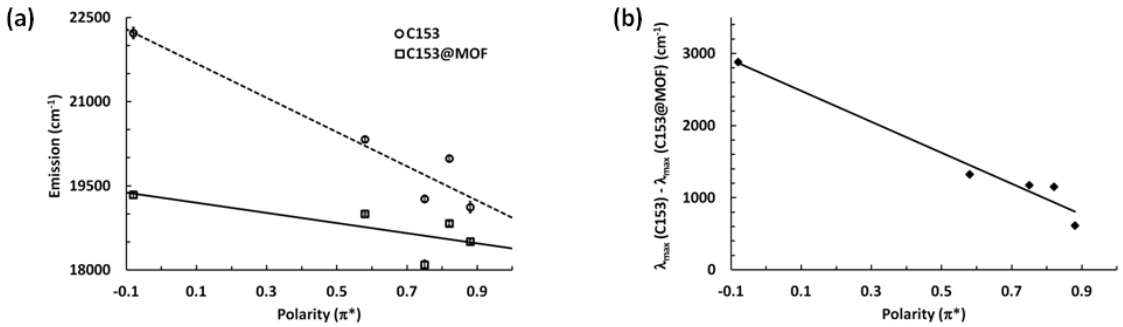

Figure 5-10: (a) Emission maxima of C153 (circle) and C153@MOF (square) as a function of solvent polarity (π*) and (b) energy difference between C153 and C153@MOF as a function of solvent polarity (π*). Equations for the best-fit lines are y = -3053.2x + 21986, R^2 = 0.9221 for C153 (dotted) in (a), y = -909.01x + 19291, R^2 = 0.5561 for C153@MOF (solid) in (b), and y = -2144.2x + 2694.6, R^2 = 0.9628 for the energy difference in (b).

Stokes shift

Stokes shifts of C153 and C153@MOF are shown in Figure 5-11a. Plotted as a function of the reaction field function ($f(\varepsilon_o) - f(n^2)$), Stokes shift is derived by subtracting the emission band energy from the absorption band energy. As reported in literature,[31] the Stokes shift of C153 displays a good linear relationship with the reaction field function. As the reaction field function of solvent molecules increases (0.000 for hexane, 0.145 for chloroform, 0.217 for DCM, 0.274 for DMF, and 0.305 for MeCN), the Stokes shift of C153 increases. Surprisingly, the linear relationship between the Stokes shift and the reaction field function can also be found for C153@MOF, which is not the case for the respective absorption and emission. Except DMF, the Stokes shifts of C153@MOF are overall larger than those of C153 (Figure 5-11b).

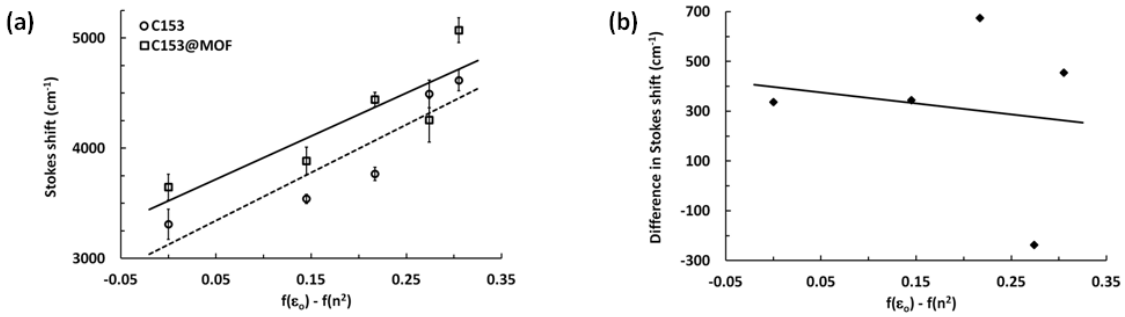

Figure 5-11: (a) Stokes shifts of C153 (circle) and C153@MOF (square) as a function of reaction field function ($f(\varepsilon_o) - f(n^2)$) and (b) energy difference between C153 and C153@MOF as a function of reaction field function ($f(\varepsilon_o) - f(n^2)$). Equations for the best-fit lines are $y = 4354.3x + 3125$, $R^2 = 0.8297$ for C153 (dotted) in (a), $y = 3913.9x + 3523$, $R^2 = 0.7487$ for C153@MOF (solid), and $y = -440.33x + 397.54$, $R^2 = 0.0251$ for the energy difference in (b).

It seems difficult to rationalize the solvent-dependent Stokes shift of C153@MOF when considering the observation of weak solvatochromism observed in the absorption and emission spectra. The consistent energy difference between C153 and C153@MOF might imply that the framework is responsible for such energy in the Stokes shift. The major sources for Stokes shift are generally listed as solvent reorganization and vibrational relaxation.[38] I cannot designate

which one gives rise to this energy difference in the Stokes shift for C153 and C153@MOF, but it seems plausible to address that the framework can increase the amount of energy loss related to either solvent reorganization, vibrational relaxation, or any other events during the electronic transition of C153.

Hypotheses

I hypothesize that there are two confined molecular interactions that influence the photophysical properties of C153 in MOF-5: (*i*) a framework-C153 interaction and (*ii*) a solvent-C153 interaction (typical solvatochromism).

The framework-C153 interaction is demonstrated by the large decrease in the absorption and emission energy for C153@MOF as well as the weak solvent-dependency in the spectra, indicating that C153 is influenced dominantly by the framework. The energy decrease for both absorption and emission of C153@MOF leads me to assume that the framework either stabilizes the S_1 state or destabilizes the S_0 state of C153. The former effect is highly possible because from a thermodynamic standpoint destabilization of the S_0 state of C153 in MOF-5 would not explain the spontaneous diffusion of C153 into MOF-5 that I observed during the synthesis of C153@MOF. Thus, on the assumption that the framework stabilizes the S_1 state of C153, a schematic energy diagram can be introduced in Figure 5-12. The stabilized S_1 state can account for the energy decrease in both absorption and emission band of C153 after encapsulated in MOF-5.

Although the framework effect mainly affects the observed spectra of C153@MOF, I cannot rule out the solvent effect for the electronic transition of C153. The solvent effect is normally more noticeable for the emission process than for the absorption process because solvent reorganization should occur and affect change of the energy levels, specially the S_1 state,

while the absorption does not reflect solvent reorganization.[38] For C153@MOF, the solvent effect can be found clearly in the plot of the Stokes shift with the reaction field function, and also from an improved R^2 value in the equation of the emission band energy as a function of solvent polarity. Thus, I conclude that the solvent-C153 interaction can still exist in this system.

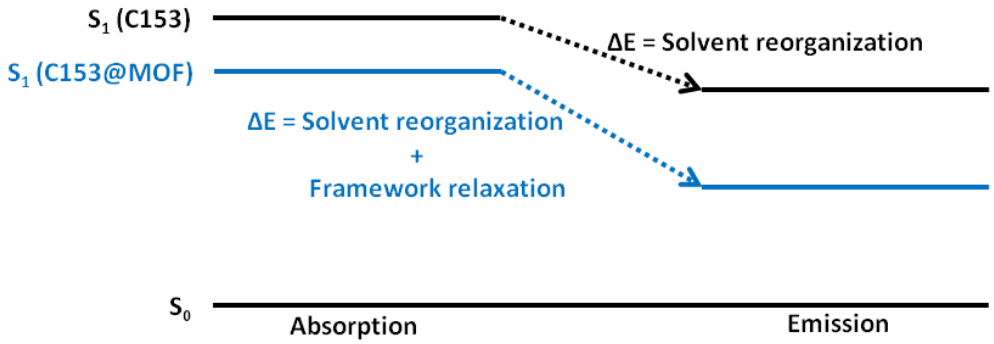

Figure 5-12: Energy levels for electronic transitions of C153 and C153@MOF.

I ascribe the existence of both two effects (framework and solvent) on C153 to the location of C153 in the pore, where C153 can be easily affected by both the framework and solvent molecules. According to literature,[24] benzene molecules are likely to reside near Zn_4O clusters inside the pore of MOF-5 rather than center of the pore. Because C153 is composed of aromatic rings, it is likely to be located near the Zn_4O clusters, which allows one plane of C153 to close contact the framework and its other plane to be exposed to solvent molecules. Then, it is probable that the electronic transition of C153 can be influenced by both the framework and solvent molecules in the pore.

The dominant framework effect might originate from a potential lattice flexibility of MOF-5. A few recent reports demonstrate that some degree of lattice flexibility exists in MOF-5.[24-26,39-42] This flexibility might be more strongly associated to the emission process of C153 than the absorption process. When solvent reorganization occurs around C153, some energy from the excited state of C153 might also be consumed by lattice relaxation in MOF-5, which appears larger than energy for solvent reorganization. Noting that less amount of solvent molecules exist

in the pore than bulk condition, C153@MOF requires less energy for solvent reorganization than C153. However, one should know that the framework effect seems to be only influential in perturbing the energy levels of C153 when solvent molecules are involved. Otherwise, there is no large energy change for the absorption and emission observed with solid C153@MOF.

Conclusions

C153 was confined in MOF-5, and its absorption and emission properties were measured with different solvents via UV-vis absorption spectroscopy and fluorescent emission spectroscopy. After confinement, C153 shows weak solvatochromic properties in the absorption and emission spectra, and the absorption and emission energy of C153@MOF become lower than those of C153 in the presence of solvent molecules. The Stokes shift of C153@MOF, however, is higher than that of C153, showing a good relationship with the reaction field function.

The framework seems to have a significant effect on the photophysical properties of C153 when solvent molecules are associated. I presume that the framework stabilizes the S_1 state of C153, resulting in the decrease for both absorption and emission energy. During the electronic transition of C153, extra energy can be consumed due to lattice flexibility of MOF-5. I conclude that the framework-guest interaction is more dominant than the solvent-guest interaction in this model system. However, the solvent effect cannot be excluded during the photophysical process of C153 because C153@MOF does not show such energy deviation without solvent molecules.

There will be more works to follow in order to elucidate the ternary guest-solvent-framework interaction. Molecular simulations will confirm the location of C153 in the pore and predict how lattice flexibility of MOF-5 can affect the properties of C153 in association with solvent molecules. It will be necessary to quantify the number of guest and solvent molecules in the pore. To verify the influence for the emission process by lattice flexibility of MOF-5, it might

be helpful to perform time-resolved vibrational spectroscopy and investigate any change of the carboxylate vibration of MOF-5. Studying the solvent-framework interaction would be informative and foundational to understand complex molecular interactions in confined environment. It can be performed by testing a series of solvent molecules, and I will learn how a specific solvent parameter affects the solvent-framework interaction.

References

1. Incavo, J. A.; Dutta, P. K. *J. Phys. Chem.* **1990**, *94*, 3075-3081.
2. Borja, M.; Dutta, P. K. *Nature* **1993,** *362*, 43-45.
3. Baumann, R.; Ferrante, C.; Kneuper, E.; Deeg, F.; Bräuchle, C. *J. Phys. Chem. A* **2003**, *107*, 2422-2430.
4. Sen, P.; Roy, D.; Mondal, S. K.; Sahu, K.; Ghosh, S.; Bhattacharyya, K. *J. Phys. Chem. A* **2005**, *109*, 9716-9722.
5. Kamijo, T.; Yamaguchi, A.; Suzuki, S.; Teramae, N.; Itoh, T.; Ikeda, T. *J. Phys. Chem. A* **2008**, *112*, 11535-11542.
6. Inagaki, S.; Ohtani, O.; Goto, Y.; Okamoto, K.; Ikai, M.; Yamanaka, K.; Tani, T.; Okada, T. *Angew. Chem. Int. Ed.* **2009**, *48*, 4042-4046.
7. Brühwiler, D.; Calzaferri, G.; Torres, T.; Ramm, J. H.; Gartmann, N.; Dieu, L.; López-Duarte, I.; Martínez-Díaz, M. V. *J. Mater. Chem.* **2009**, *19*, 8040-8067.
8. Sen, R.; Koner, S.; Bhattacharjee, A.; Kusz, J.; Miyashita, Y.; Okamoto, K. *Dalton Trans.* **2011**, *40*, 6952-6960.
9. Larsen, R. W.; Wojtas, L. *J. Phys. Chem. A* **2012**, *116*, 7830-7835.
10. Eddaoudi, M.; Moler, D. B.; Li, H.; Chen, B.; Reineke, T. M.; O'Keeffe, M.; Yaghi, O. M. *Acc. Chem. Res.* **2001**, *34*, 319-330.
11. Sumida, K.; Rogow, D. L.; Mason, J. A.; McDonald, T. M.; Bloch, E. D.; Herm, Z. R.; Bae, T.; Long, J. R. *Chem. Rev.* **2012**, *112*, 724-781.
12. Suh, M. P.; Park, H. J.; Prasad, T. K.; Lim, D. *Chem. Rev.* **2012**, *112*, 782-835.
13. Li, J.; Sculley, J.; Zhou, H. *Chem. Rev.* **2012**, *112*, 869-932.
14. Czaja, A. U.; Trukhan, N.; Müller, U. *Chem. Soc. Rev.* **2009**, *38*, 1284-1293.

15. Lee, J.; Farha, O. K.; Roberts, J.; Scheidt, K. A.; Nguyen, S. T.; Hupp, J. T. *Chem. Soc. Rev.* **2009**, *38*, 1450-1459.
16. Eddaoudi, M.; Kim, J.; Rosi, N.; Vodak, D.; Wachter, J.; O'Keeffe, M.; Yaghi, O. M. *Science* **2002**, *295*, 469-472.
17. Yaghi, O. M.; O'Keeffe, M.; Ockwig, N. W.; Chae, H. K.; Eddaoudi, M.; Kim, J. *Nature* **2003**, *423*, 705-714.
18. Rowsell, J. L. C.; Yaghi, O. M. *Microporous Mesoporous Mater.* **2004**, *73*, 3-14.
19. Rosi, N. L.; Kim, J.; Eddaoudi, M.; Chen, B.; O'Keeffe, M.; Yaghi, O. M. *J. Am. Chem. Soc.* **2005**, *127*, 1504-1518.
20. Deng, H.; Grunder, S.; Cordova, K. E.; Valente, C.; Furukawa, H.; Hmadeh, M.; Gándara, F.; Whalley, A. C.; Liu, Z.; Asahina, S.; Kazumori, H.; O'Keeffe, M.; Terasaki, O.; Stoddart, J. F.; Yaghi, O. M. *Science* **2012**, *336*, 1018-1023.
21. Wang, Z.; Cohen, S. M. *Chem. Soc. Rev.* **2009**, *38*, 1315-1329.
22. Deria, P.; Mondloch, J. E.; Karagiaridi, O.; Bury, W.; Hupp, J. T.; Farha, O. K. *Chem. Soc. Rev.* **2014**, *43*, 5896-5912.
23. Brozek, C. K.; Dincă, M. *Chem. Soc. Rev.* **2014**, *43*, 5456-5467.
24. Amirjalayer, S.; Tofipolsky, M.; Schmid, R. *Angew. Chem. Int. Ed.* **2007**, *46*, 463-466.
25. Amirjalayer, S.; Schmid, R. *Microporous Mesoporous Mater.* **2009**, *125*, 90-96.
26. Ford, D. C.; Dubbeldam, D.; Snurr, R. Q.; Künzel, V.; Wehring, M.; Stallmach, F.; Kärger, J.; Müller, U. *J. Phys. Chem. Lett.* **2012**, *3*, 930-933.
27. Li, H.; Eddaoudi, M.; O'Keeffe, M.; Yaghi, O. M. *Nature* **1999**, *402*, 276-279.
28. Stallmach, F.; Gröger, Künzel, V.; Kärger, J.; Yaghi, O. M.; Hesse, M.; Müller, U. *Angew. Chem. Int. Ed.* **2006**, *45*, 2123-2126.
29. Han, S.; Wei, Y.; Valente, C.; Lagzi, I.; Gassensmith, J. J.; Coskun, A.; Stoddart, J. F.; Grzybowski, B. A. **2010**, *132*, 16358-16361.
30. Münch, A. S.; Seidel, J.; Obst, A.; Weber, E.; Mertens, F. O. R. L. *Chem. Eur. J.* **2011**, *17*, 10958-10964.
31. Maroncelli, M.; Fleming, G. R. *J. Chem. Phys.* **1987**, *86*, 6221-6239.
32. Horng, M. L.; Gardecki, J. A.; Papazyan, A.; Maroncelli, M. *J. Phys. Chem.* **1995**, *99*, 17311-17337.
33. Huang, L.; Wang, H.; Chen, J.; Wang, Z.; Sun, J.; Zhao, D.; Yan, Y. *Microporous Mesoporous Mater.* **2003**, *58*, 105-114.

34. Laurence, C.; Nicolet, P.; Dalati, M. T.; Abboud, J. M.; Notario, R. *J. Phys. Chem* **1994**, *98*, 5807-5816.
35. Bordiga, S.; Lamberti, C.; Ricchiardi, G.; Regli, L.; Bonino, F.; Damin, A.; Lillerud, K. P.; Bjorgen, M.; Zecchina, A. *Chem. Commun.* **2004**, 2300-2301.
36. Silva, C. G.; Corma, A.; García, H. *J. Mater. Chem.* **2010**, *20*, 3141-3156.
37. Feng, P. L.; Perry IV, J. J.; Nikodemski, S.; Jacobs, B. W.; Meek, S. T.; Allendorf, M. D. *J. Am. Chem. Soc.* **2010**, *132*, 15487-15489.
38. Bayliss, N. S.; McRae, E. G. *J. Phys. Chem.* **1954**, *58*, 1002-1006.
39. Gould, S. L.; Tranchemontagne, D.; Yaghi, O. M.; Garcia-Garibay, M. A. *J. Am. Chem. Soc.* **2008**, *130*, 3246-3247.
40. Greathouse, J. A.; Allendorf, M. D. *J. Phys. Chem. C* **2008**, *112*, 5795-5802.
41. Takakura, K.; Ueda, T.; Miyakubo, K.; Eguchi, T. *Phys. Chem. Chem. Phys.* **2013**, *15*, 279-290.
42. Joo, J.; Kim, H.; Han, S. S. *Phys. Chem. Chem. Phys.* **2013**, *15*, 18822-18826.

Chapter 6

Conclusions and future directions

In this dissertation, I demonstrated the ligand-controlled method for understanding how the electronic properties of inorganic materials can be tuned by intramolecular or intermolecular interactions between the inorganic substrates and ligands. This research theme was motivated from current needs in the scientific community to seek for a facile methodology in controlling the electronic properties of inorganic materials, which can range from molecular complexes to nano-scale materials. Exploring the electronic interactions between inorganic materials and ligands can provide foundational knowledge that will help devise an inorganic material whose electronic properties can be well-fitted to targeted applications. My dissertation represented how a specific ligand property (electron density, molecular structure, π-conjugated orbital, and confined space) could influence the electronic properties of inorganic materials (ruthenium polypyridyl complexes, a TCNQ-coordinated zinc complex, zinc oxide semiconductor nanocrystals, and solvatochromic molecules). Below, I will summarize the previous chapters and propose future directions.

Ligand-controlled electron transfer in transition metal complexes

In Chapter 2 and 3, I exhibited the ligand effects to the electronic structure of transition metal complexes through two different types of electron transfer process (intramolecular and intermolecular). In both chapters, novel inorganic complexes were first synthesized, following spectroscopic, electrochemical, and magnetic characterization: ruthenium polypyridyl complexes with a hydroxypyridine ligand (Chapter 2) and a dinuclear zinc complex with a TCNQ σ-dimer

(Chapter 3). The intramolecular electron transfer was investigated with the former complexes, and the intermolecular electron transfer was studied with the latter one.

Study of the ruthenium polypyridyl complexes was performed by modifying the substituents in the hydroxypyridine ligand, which led me to understand how change in the electron density of an ancillary ligand affects the electronic structure of an entire molecule. Deprotonation of the hydroxypyridine ligand could enrich the electron density of the ruthenium metal center, and also this effect influenced the electronic properties of the bipyridine ligands, which was observed by chemical shifts of the protons in the bipyridine ligands. Ethylation of the hydroxypyridine ligand, however, did not perturb the electronic properties of neither the metal center nor the bipyridine ligands, but only increased the electron density of the hydroxypyridine ligand itself. Furthermore, the one-electron reduction of the ethylated complex could generate a stable species and allowed me to investigate the intramolecular electron transfer from a reduced bipyridine to a neutral bipyridine. I found no absorption signal for such electron transfer and concluded that the complex did not have good electronic coupling between the bipyridine ligands through the metal center.

In Chapter 3, the intermolecular electron transfer between redox-active TCNQ ligands could be explored with crystals of **Zn dimer**. Different from a TCNQ mono-radical and formed linear π-stacking, the TCNQ σ-dimer allowed **Zn dimer** to be stacked in a zigzag pattern. Two single TCNQ ligands were stacked closely to each other and the π-stacked single TCNQ ligands were covered by two TCNQ σ-dimer ligands. The intermolecular electron transfer was observed at higher energy than that of linear π-stacked TCNQ salts, also resulting in poor electrical conductivity. It was concluded that the zigzag stacking pattern and large spacing distance between the single TCNQ ligand and the TCNQ σ-dimer ligand gave rise to the poor electronic coupling throughout the π-stacking. The EPR spectroscopy demonstrated that there was

antiferromagnetic coupling between the single TCNQ ligands. Investigation of **Zn dimer** provided me an understanding that a different molecular structure, in this study the TCNQ σ-dimer, can bring about change in the stacking pattern. This change consequently affects energy for the intermolecular electron transfer and further magnetic coupling between the TCNQ ligands in the π-stacks.

I believe that these two demonstrations suggest a useful way to tune the electronic properties of transition metal complexes by modifying substituents in a ligand or coordinating a structurally different redox-active ligand derivative. As a continuing study of Chapter 2, I would like to change the metal center from ruthenium to iron or osmium in order to find any relationship between the degree of the intramolecular electron transfer and the electron density of the metal center. Furthermore, having electron-withdrawing functional groups to the bipyridine ligands will decrease their reduction potentials and separate them from the redox event of the hydroxypyridine ligand. Then, it would be possible to generate a reduced species of **1** and examine the intramolecular electron transfer mediated by pH change.

I think that the properties of **Zn dimer** have not been fully understood, and I would be interested in examining the magnetic properties at high temperatures and also elucidating the solution-phase behavior of an individual molecule. Due to technical limits in the EPR instrument, a temperature-dependent study could not be implemented. I expect that **Zn dimer** might give rise to further magnetic coupling between the single TCNQ and TCNQ σ-dimer ligand at elevated temperatures, which might lead to change in the electronic conductivity. Moreover, if it is possible to maintain the same π-stacking pattern, change of the metal center to a paramagnetic metal such as Mn(II) and Fe(III) might generate addition interactions between electron spins in the TCNQ ligands and the paramagnetic metals. This magnetic interactions can provide another possibility for controlling the electron conduction through the π-stacks.

Ligand-controlled interfacial electronic interactions with zinc oxide nanocrystals

I discussed the ligand effect to the bandgap energy of zinc oxide semiconductor nanocrystals in Chapter 4. The nanocrystals were synthesized through hydrolysis and condensation of zinc acetate at room temperature, following ligand modification. The resulted zinc oxide nanocrystals had the Wurtzite structure and they were 3-4 nm in diameter. Their bandgap energy was determined using UV-vis absorption spectroscopy. The bandgap absorption band occurred around 330 nm, which corresponded to the diameter of the nanocrystals determined via TEM. Three different carboxylic acids (propionic acid, benzoic acid, and hydroxybenzoic acid) were utilized as surfactants to the nanocrystals. The absorption band energy for propionic acid-modified nanocrystals was higher than those for the nanocrystals with benzoic acid and hydroxybenzoic acid, respectively. The observation in which benzoic acid-modified nanocrystals showed a smaller bandgap energy than propionic acid-modified ones led me to speculate that the aromatic ligand might create better interfacial electronic coupling with the nanocrystals than those with the aliphatic ligand. I assume that the electron density of the nanocrystals could be more delocalized toward the aromatic ligands adsorbed on the nanocrystals.

I will be required to perform additional experiments in order to verify my hypothesis of the ligand effect to the bandgap perturbation of zinc oxide nanocrystals. It might be true that the red-shift in the UV-vis absorption band was observed because the size of the nanocrystals indeed increased. Thus, it is necessary to precisely measure the size of the nanocrystals using TEM or other techniques so that the ligand effect can be a reasonable conclusion. After this examination, I would like to explore the ligand effect to the conduction band of the nanocrystals directly. An advantage for using zinc oxide nanocrystals is that electrons in the conduction band can be easily generated and more stable than other types of semiconductor nanocrystals. Thus, direct

investigation of electrons in the conduction band with the ligand will provide detailed information about the ligand effect to the band structure.

Perturbation of the electronic properties of coumarin 153 confined in MOF-5

Chapter 5 showed a systematic approach for understanding the photophysical properties of a solvatochromic molecule in a confined environment. Herein I chose to encapsulate coumarin 153 in MOF-5. It was observed that this confined environment could perturb the absorption and emission events of coumarin 153 in the presence of solvent molecules. The spectra of the confined molecule did not show any good relationship to solvent polarity, and there was a large energy decrease in both absorption and emission bands. The Stokes shift, however, displayed a good solvent-dependency with increased energy.

The confined space in MOF-5 did not allow as many solvent molecules around coumarin 153 as bulk condition does. It was expected to observe weak solvent-dependent response in the absorption and emission of the molecule. Thus, the framework effect became more dominant than the solvent effect. I tentatively concluded that the framework could stabilize the excited state of coumarin 153 when solvent molecules were present. In addition, lattice flexibility of the framework, specifically ligand rotation, might dissipate energy during the emission process of coumarin 153, which may be responsible for the increased energy in the Stokes shift. Further studies would be to investigate the photophysical response of the molecule by modulating specific parameters such as pore size, ligand type, and framework structure.

Conclusions

In my dissertation, I studied control of the electronic properties of four different inorganic materials by the ligand-assisted method. My studies demonstrated that ligands can have significant effects to the electronic properties of inorganic materials. In general, inorganic materials inevitably contain covalent bonding with ligands, but the ligand effect has not been focused significantly when one needs to find an inorganic material suitable for a specific application. Beyond regarding ligands as stabilizing agents for metals, one can turn to explore ligand-mediated electronic interactions with inorganic materials. Incorporation of a proper ligand or modification of a coordinated ligand can provide a new controllability in tuning inorganic materials.

VITA

Juyeong Kim

2006 Bachelor of Engineering, Ajou University, Suwon, South Korea

2009 Master of Science, Sungkyunkwan University, Suwon, South Korea

2015 Doctor of Philosophy, The Pennsylvania State University, Pennsylvania, United States

PUBLICATIONS

Kim, J.; Dolgos, M.; Lear, B. J. *Crystal Growth & Design*, **2015**, *In revision*.

Kim, J.; Silakov, A.; Yennawar, H. P.; Lear, B. J. *Inorganic Chemistry*, **2015**, *54*, 6072-6074.

Kim, J.; Yennawar, H. P.; Lear, B. J. *Dalton Transactions*, **2013**, *42*, 15656-15662.

Jang, J.; Kim, J.; Lee, Y.; Kim, I. Y.; Park, M.; Yang, C.; Hwang, S.; Kwon, Y. *Energy & Environmental Science*, **2011**, *4*, 4947-4953.

Lee, Y.; Kim, G.; Joe, M.; Jang, J.; Kim, J.; Lee, K.; Kwon, Y. *Chemical Communications*, **2010**, *46*, 5656-5658.

Jang, J.; Kim, J.; Lee, Y.; Park, C.; Kwon, Y. *Electrochimica Acta*, **2009**, *55*, 485-490.

Kim, J.; Jang, J.; Lee, Y.; Kwon, Y. *Journal of Power Sources*, **2009**, *193*, 441-446.